Thermo-mechanical behaviour of thick copper metallizations for power electronics

Doctoral Thesis

April 2017

Stephan (Paul) Bigl

Department Materials Physics, Montanuniversität Leoben

Die vorliegende Arbeit wurde innerhalb des EPPL (Enhanced Power Pilot Line) Projekts durchgeführt, mit der finanziellen Unterstützung von Fördergeldern aus Österreich, Deutschland, Niederlanden, Frankreich, Italien, Portugal und dem ENIAC Joint Undertaking (ENIAC JU Förderabkommen Nr. 325608). Zusätzlich wurde das Projekt durch Gelder aus dem Programm, "Forschung, Innovation und Technologie für Informationstechnologie" vom Bundesministerium für Transport, Innovation und Technologie gefördert.

Ich erkläre an Eides statt, dass ich diese Arbeit selbständig verfasst, andere als die angegebenen Quellen und Hilfsmittel nicht benutzt mich auch sonst keiner unerlaubten Hilfsmittel bedient habe.

Leoben, April 2017 Stephan P. Bigl

Danksagung

Ich habe sehr lange darüber nachgedacht wem und was ich eigentlich zu Dank verpflichtet bin, bzw. was vielleicht der tiefere Sinn folgender Zeilen sein könnte. Eine konkrete Antwort darauf habe ich freilich nicht gefunden, geschweige denn parat. Aber dafür ist mir viel mehr der eigentliche Zweck einer Dissertation bewusst geworden. Nicht die Qualität, oder gar die Quantität der fertigen Arbeit sind das eigentliche Ziel, sondern das eigenständige arbeiten und lösen von komplexen Problemstellungen.

Dabei sollte auch im gleichen Maße die eigene Person zu einem selbstständig denkenden Individuum in unserer Gesellschaft heranreifen, welches sich mit der Umwelt und mit sich selbst, kritisch auseinander setzt. Aus diesem Grund möchte ich anstatt der üblichen „hierarchische Dankesliste“ folgende Worte für meine Leser festhalten:

Ich danke allen Menschen die mich im Laufe meiner Arbeit und Lebenszeit in Leoben unterstützt haben. Egal ob diese Unterstützung durch wissenschaftliche Betreuung erfolgte, oder durch private Vergnügen, wie das gesellige Beisammensein. Auch ob es sich bei den jeweiligen Personen um direkte Kollegen, Betreuer, Freunde, Pfadfinderkameraden, oder Familienmitglieder handelt spielt letztlich keine übergeordnete Rolle. Genauso möchte ich auch die negativen Aspekte, egal ob arbeitstechnischer als auch zwischenmenschlicher Natur, als lehrreiche und vor allem wichtige Erfahrungen für das weitere Leben hervorheben.

Denn führt nicht letztendlich die Gesamtheit aller positiven sowie negativen Aspekte im Leben zu den Resultaten die wir als Menschen wahrnehmen, bzw. ernten?

Bevor ich aber anfange um den heißen Brei zu reden, möchte ich noch folgendes berühmte Schlusszitat des Kabarettisten Karl Farkas meiner angeführten Dissertation vorausschicken:

“*Schau´n Sie sich das an!*“

Table of Contents

I Introduction I-1

1 Application background and motivation I-1
2 Literature review of thermo-mechanical film fatigue I-4
3 Aim of this work I-6
4 Thermal cycling and microstructural characterization I-7
5 References I-16

II Summary of work II-2

III Short summary of publications III-1

1. Publication A III-1
2. Publication B III-1
3. Publication C III-2
4. Publication D III-3
5. Publication E III-3
6. Publication F III-4

IV Publication A IV-1

1 Introduction IV-2
2 Experimental IV-2
3 Results and Discussion IV-4
4 Summary and Outlook IV-7
5 Acknowledgements IV-7
6 References IV-7

V Publication B V-1

1 Introduction V-2
2 Materials V-4
3 Experimental V-4
4 Results V-6
5 Discussion V-21
6 Conclusions and Summary V-26
7 Acknowledgement V-27
8 References V-27

VI Publication C VI-1

1 Introduction VI-2
2 Experimental VI-4
3 Results VI-5
4 Discussion VI-15
5 Conclusions and Summary VI-21
6 Acknowledgement VI-22
7 References VI-22

VII Publication D VII-1

1 Introduction VII-2
2 Materials and Experimental Methods VII-3
3 Results VII-8
4 Discussion VII-17
5 Conclusion VII-20
6 Acknowledgements VII-21
7 References VII-21

VIII Publication E VIII-1

1 Introduction VIII-2
2 Materials and Experimental VIII-3
3 Results and Discussion VIII-5
4 Acknowledgement VIII-22
5 References VIII-22

IX Publication F IX-1

1 Introduction IX-2
2 Materials and Experimental IX-3
3 Results IX-4
4 Discussion IX-6
5 Conclusions IX-9
6 Acknowledgement IX-10
7 References IX-10

X List of Publications X-1

I Introduction

1 Application background and motivation

Since the origins of large scale integrated circuits production in the early 1960s, thin films play an important role in the semiconductor manufacturing process [1]. The ambiguously used adjective “thin” can be understood as a film thickness, ranging from a few nanometers (e.g. high-k dielectrics) up to several micrometers (e.g. metal films).

In modern power electronics, the increasing performance requirements such as high current capability and high switching frequencies demand metallization schemes which are able to not only serve as an electrical connection, but also laterally dissipate the thermal heat generated by a power pulse [2]. Depending on the specific product specifications the metallization thickness can reach up to 20 µm [3]. This requires not only a cost efficient deposition process with respect to the increasing thickness, but more importantly raises the need for improved electrical and thermal material properties.

Copper (Cu), with its superior electrical and thermal properties, is replacing Aluminium (Al) as the standard material for thick metallization layers [4]. In a switching event the extreme electric power densities create large temperature rises in the device. The Cu metallization acts as a heat sink and actively removes the thermal energy and prevents any device damage such as a thermal runaway [2].

Since the Cu metallization is deposited on to a thin film stack on a monolithic substrate such as silicon, the mismatch in the coefficient of thermal expansion (CTE) creates large rapid thermal stresses [5]. Experimental results and numerical simulations have shown that such repetitive power pulses can locally lead to a maximum temperature up to about 400°C [6]. Inevitably the generated thermal stresses exceed the yield point of Cu and cause plastic deformation events, which change the microstructure of the Cu film and lead to thermo-mechanical fatigue events such as diffusional mass transport and motion of dislocations [7].

Figure 1 [2] presents a focused ion beam (FIB) cross-section of a power semiconductor device which was actively cycled. In the Cu metallization cracks along the grain boundaries and small voids formed (indicated by arrows). Further stressing of the device

would eventually lead to a mechanical failure of the metallization and induce local hot spots, where the generated heat cannot be efficiently removed from the transistor region. As a consequence of the local accumulation of thermal energy, the device would lose its functionality.

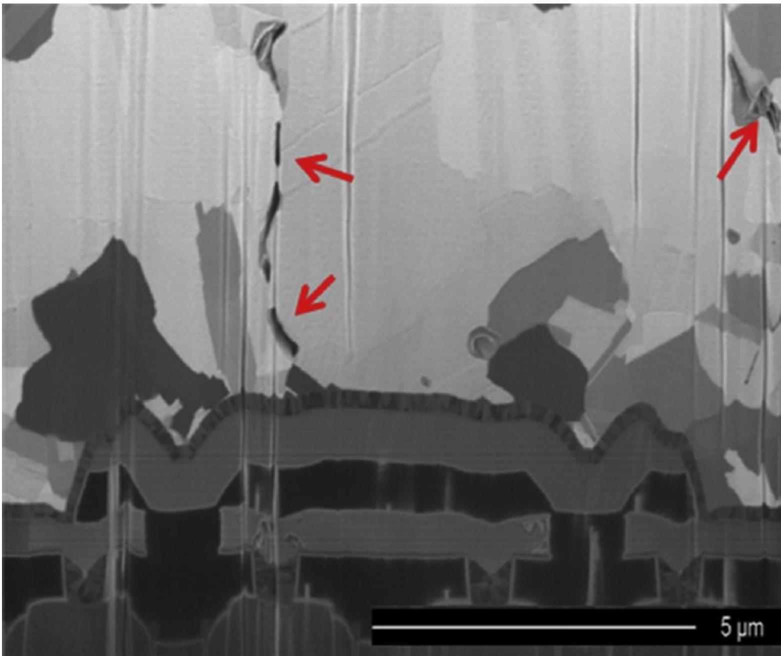

Figure 1: FIB cross-section of a semiconductor device after active power cycling reveals cracks and voids formed (indicated by arrows) in the Cu metallization [2].

To improve the operational lifetime and reliability of such power semiconductor devices, state of the art Cu metallization schemes increase their heat capacity by the increase of the film thickness. Since conventional sputter deposition is not economically feasible for thick metallizations (~5-20 µm), electrochemical deposition has become the standard copper deposition process due to its performance and cost efficiency [8, 9]. A high degree of freedom with regard to process parameters and the usage of additives lead to customized film microstructures and high deposition rates. This can often result in high residual inorganic impurity concentrations, which can have an effect on the microstructural stability [10]. Based on energy minimising models, thicker films (> 5 µm) will result in a different film texture and grain size [11] and therefore require experimental investigation with regards to their influence on the thermo-mechanical behaviour. The reduction of the substrate thickness for improved electrical device performance leads to increased substrate bending when subjected to thermal cycles due

to the reduced bending stiffness [12]. The effect of such thickness reduction is not considered in simplified film stress theories and therefore experimental data is needed for basic understanding. Additionally, the sub-millisecond thermal cycles in power electronics require cycling methods which offer high heating/cooling rates to experimentally simulate the dynamic conditions in actively cycled microelectronic devices.

2 Literature review of thermo-mechanical film fatigue

The term fatigue can be generally understood as a phenomenon where cyclic loading causes a progressive (micro)structural damage which eventually can lead to failure [13]. Cyclic loading events also occur in thin film structures used in the microelectronic industry. In microelectronic devices, integrated film structures experience temperature cycling during fabrication and operation where the mismatch of CTE between the substrate (i.e. wafer) and the film results in large strains and stresses [14].

The cyclic damage formation and evolution in Cu bulk materials has been studied since the second half of the 19th century and an extensive amount of literature is available [15-20]. With the beginning of the semiconductor area the field of thin film fatigue initiated a new field of research. In contrast to their bulk counter parts, the thin film fatigue phenomena exhibit distinctively different characteristics due to their significant reduction of one physical dimension (thickness of the film) and the film-substrate constraint. This has the consequence that the resulting grainsize, d, is frequently proportional to the deposited metal film thickness h_f (d ~ h_f) [11, 21]. Studies have shown that the yield strength of thin films has an inverse relationship with regards to h_f [22-24]. Similar as reported for fine grained bulk materials a Hall-Petch relation is observed, where the increase in strength of thin films is explained by the fact that dislocation motion is restricted by grain boundaries and the substrate-film interface leading to dislocation pile ups [25, 26].

Since complex interactions of dislocations with grain boundaries and interfaces in metal films dictate the mechanical characteristics, the fatigue behaviour of Cu films was found to be different compared to their bulk material counterparts. Most studies on films and foils reported that with decreasing h_f an increase in fatigue life and resistance was observed [27-31]. The fatigue mechanism as well as the damage morphology was strongly dependent on the film thickness, which is directly connected to the grain size. One fundamental conclusion with respect to films with $h_f \geq 1$ µm was that dislocations structures throughout the thermo-mechanical fatigue experiment differently develop due to the limited volume of thinner films. Instead of characteristic fatigue dislocation structures, such as persistent slip bands (PSB) with a periodic spacing found in grains with $d > 3$ µm [32], thin films (< 1 µm) did not show these characteristics [28, 29, 33,

34]. In fact, many studies with film thicknesses > 1 μm reported that cyclic loading of the Cu films led to a similar fatigue damage which is present in bulk Cu [35, 36]. Intergranular cracks, extrusions at the surface and voids at the film-substrate interface have been reported [37, 38]. The authors emphasized that voids, initiators for cracks that formed by an agglomeration of vacancies, are the main factor of failure in thermal fatigue for Cu films.

The high elastic anisotropy in Cu also leads to a film thickness dependent texture with respect to the out-of-plane orientation [39]. The minimisation of strain energy and surface energy of the individual crystal orientations compete with each other, resulting in a preferable {111} texture for Cu films less than 4 μm, whereas a {100} texture was observed for thicker films [40]. Thermal fatigue experiments have shown an orientation dependent damage evolution [35, 41, 42] although full understanding regarding the mechanism and its consequences for fatigue lifetime would need further experimental verification with state-of-the-art methods.

3 Aim of this work

As explained above, thermo-mechanical fatigue in Cu films plays a key role with regards to the reliability of microelectronic devices. Previous studies focused on the thermo-mechanical behaviour of pure thin (≤ 5 µm) Cu films on rigid and compliant substrates. Therefore, the aim of this thesis is to extend the current literature knowledge regarding thermo-mechanical Cu film fatigue.

To mimic the cyclic thermally induced stresses in the Cu film material, we use an infrared furnace with inert/reductive atmosphere where cycle time is about a factor of 30 faster than cycling during conventional wafer curvature experiments with the same respective temperature range. Moreover, a new fast cycling set-up is implemented which uses a high power diode laser for heating and a pyrometer for in-situ sample temperature measurement. Using these experimental cycling methods in combination with in-situ film stress measurements (wafer curvature) the thermo-mechanical fatigue behaviour of Cu films will be investigated.

The utilization of a site specific characterization method combining electron back scatter diffraction (EBSD) and atomic force microscopy during the thermal cycling will enable novel insights on the local microstructural evolution of Cu films. Additionally, focussed ion beam (FIB), scanning electron microscopy (SEM), nanoindentation and four point probe sheet resistivity will provide valuable information on a global as well as local scale with respect to the mechanisms governing fatigue in Cu metallizations.

The experimental work investigates the influence of residual inorganic impurities on the thermo-mechanical fatigue behaviour as well as the effect on grain boundaries within the corresponding microstructures. Inorganic species in the ppm region have become an important concern because fast and cost efficient plating schemes use a complex electrolyte chemistry to fulfil certain semiconductor process specifications such as film thickness and surface roughness. In the current literature numerous studies investigated the microstructural properties with respect to thermo-mechanical fatigue behaviour for thin Cu films (< 5 µm). Hence, specific focus in this work will lie in the understanding of the microstructural evolution. The influence of the decrease in substrate thickness is taken into account to investigate the validity of the widely used Stoney's film stress

model [43] Moreover, the fatigue mechanisms will be evaluated with respect to the influence of the high strain rates (heating/cooling rates) caused by the thermal cycling methods.

4 Thermal cycling and microstructural characterization

In order to obtain experimental data with respect to the microstructural evolution of Cu films upon cyclic thermo-mechanical loading, specific focus was placed in the development of a new cycling method enabling rapid temperature changes with respect to the studied film-substrate structures. This is one of the key requirements in fatigue testing for modern (power) electronic applications, since respective heating and cooling rates generated by power pulses during device switching are distinctively larger than common wafer curvature methods can assess. The fast heating/cooling rates will not only allow application-related testing conditions, but moreover lead to new insights regarding the influence of high thermally induced strain rates on the microstructural evolution of Cu films.

Secondly, characterization methods have to be developed and applied which support fast and reliable experimental data generation with regards to microstructural changes during thermo-mechanical cycling. Current state of the art microstructure characterization methods for fatigue of metallic films focus on high resolution techniques such as FIB and transmission electron microscopy (TEM). These methods exhibit great insights with respect to the microstructural response of thermally strained films, but require extensive preparation time and are limited with respect to the amount of information generated by testing (e.g. small high resolution images of certain microstructural features using TEM). Changes in microstructural properties during cycling such as grain size, grain boundary strength, or film texture have to be evaluated on a global as well as local scale. This would allow the development of microstructural fatigue mechanisms and permit statistically significant results.

Thermal cycling and experimental verification

To experimentally simulate the cyclic switching conditions in semiconductor power devices, three customized thermal cycling devices have been used/developed.

Wafer Curvature:

A high temperature wafer curvature system was used to evaluate the corresponding biaxial stresses of the copper films as a function of temperature. The stress-temperature curves represent the global elasto-plastic film behaviour within the desired temperature range. In Figure 1 the customized wafer curvature set up for temperatures up to 1000°C is shown. Detailed information regarding the used experimental set up can be found in [44].

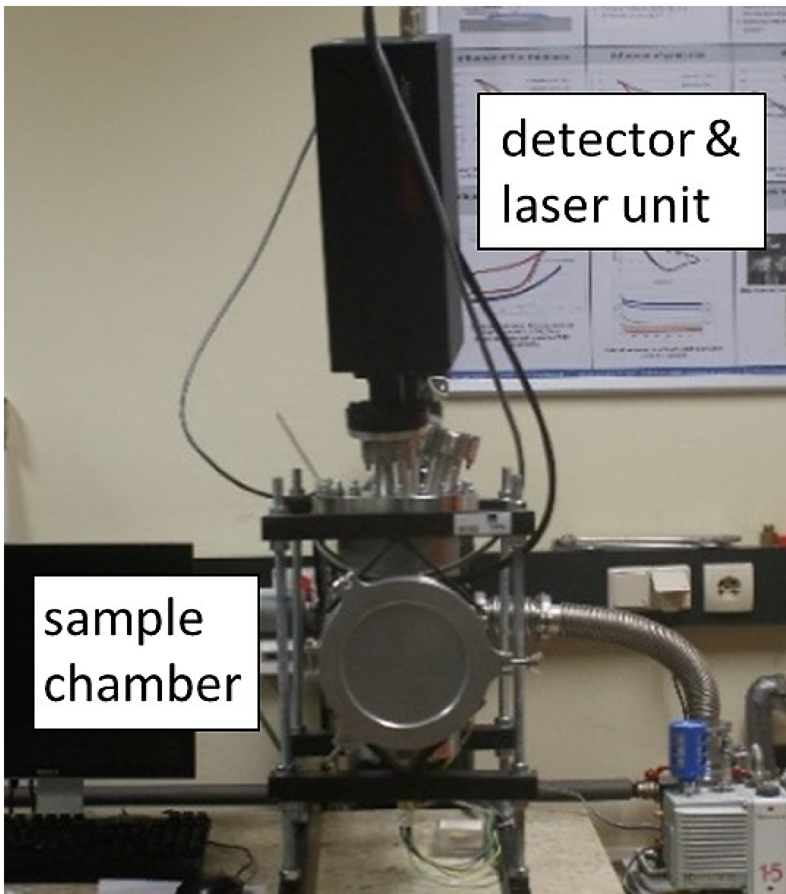

Figure 1: Wafer curvature set up using a multi optical beam sensor detection system from kSpace and a customized heating set up enabling in situ biaxial film stress measurements up to 1000°C.

The film stresses were measured under vacuum conditions ($5*10^{-4}$ mbar) via using a multi-beam optical sensor (MOS) which creates a two dimensional laser beam array on the film-substrate specimens. The change of the film-substrate curvature with respect to

temperature was assessed via a strong ceramic heating plate, where the temperature program was monitored using the temperature controller and the detection software.

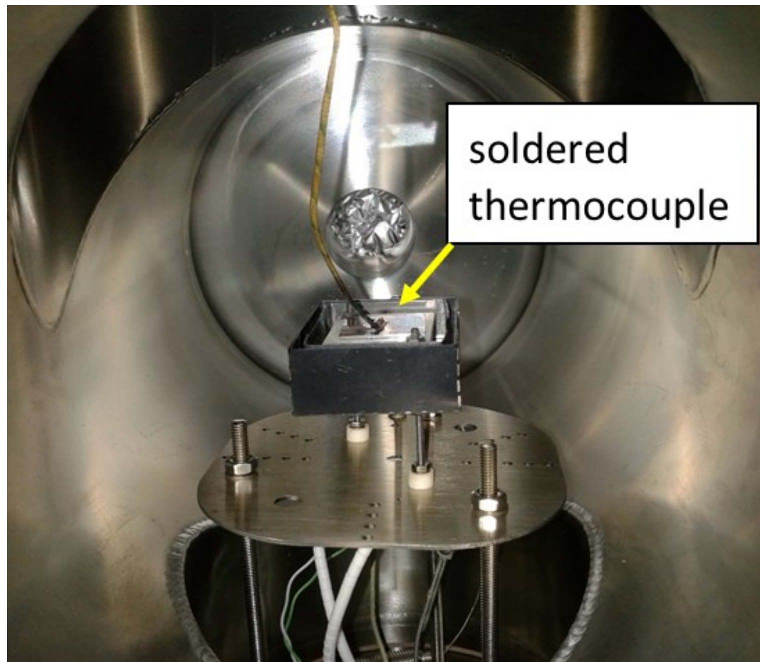

Figure 2: Heating plate inside the vacuum chamber of the wafer curvature set up. The type K thermocouple is brazed on a Cu film specimen.

Since the investigation of the thermo-mechanical fatigue behaviour of Cu films is strongly dependent on the validity and precision of the used experimental temperature ranges, great effort was made to evaluate the actual temperatures of the samples during thermal cycling for each measurement device. The experimental approach is presented in Figure 2. Thereby, the actual surface temperature of the Cu film with respect to the heating plate temperature was determined using type K thermocouples brazed on a Cu film specimen. A small amount of solder material was used to achieve an ideal contact of the thermocouple with the Cu film surface. Via a vacuum flange with an electrical feed through it was possible to detect the sample temperature during the thermal cycling of the samples in the wafer curvature system. This enabled the correct temperature evaluation with respect to the chosen heating and cooling rate and allowed for precise temperature correction of the experimental data.

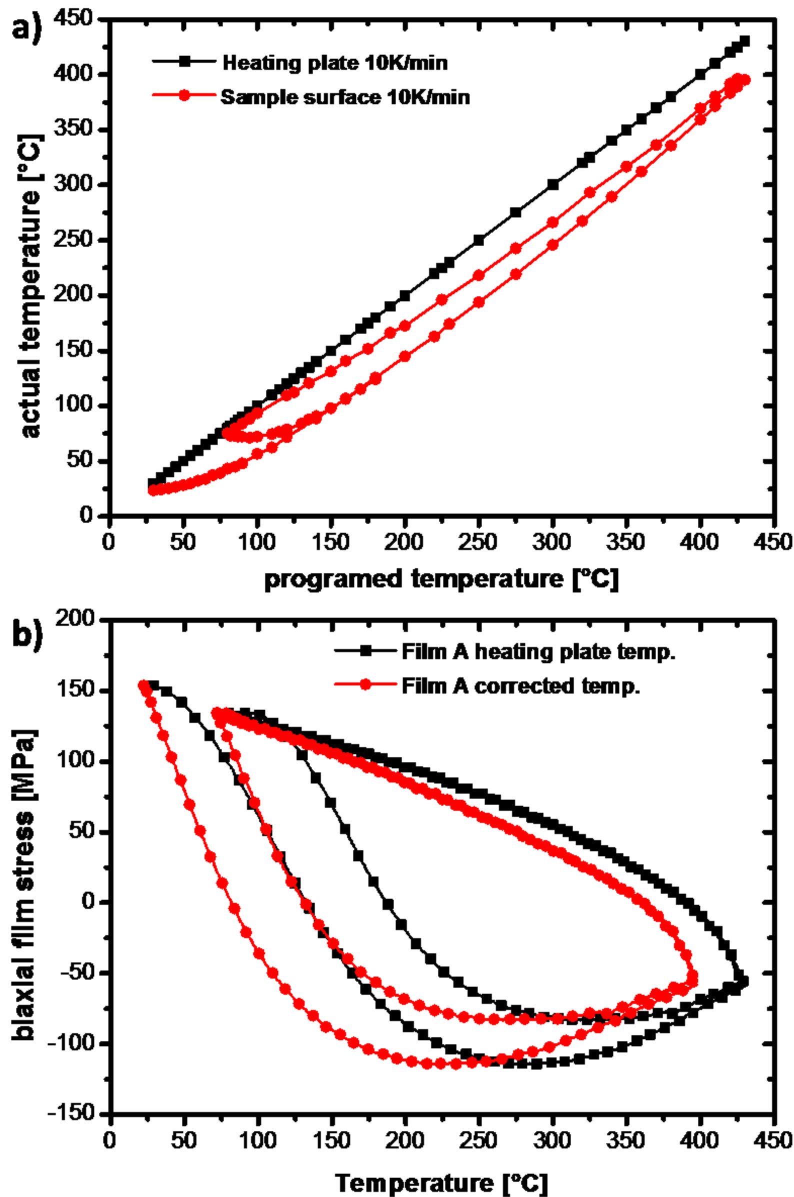

Figure 3: Relationship between the measured heating plate temperature and the sample temperature as a function of the programmed temperature (a). Stress-temperature cycles of a Cu film, denoted Film A, (5 µm thickness) using the heating plate temperature data and the corresponding corrected stress-temperature plot based on a polynomial correction function (b).

Figure 3a illustrates the relationship between the heating plate temperature and the actual sample temperature at a heating and cooling rate of 10 K/min. The temperature of the thermocouple in the heating plate shows a linear increase of the temperature with respect to the programmed temperature of the defined thermal cycle (black line with squares). In contrast, the measured sample temperature shows a non-linear temperature increase at the initial temperature ramp up of the experiment (red line with circles). This indicates that due to the lack of heat transfer in the lower temperature region (non-

radiative heat transfer regime) and the lack of convective heat transfer mechanisms (vacuum conditions) a slow temperature increase is observed. This results in a specific sample temperature hysteresis compared to the measured heating plate temperature.

Figure 3b shows how the sample temperature evaluation can be used to correct the results from the wafer curvature experiments. The original stress hysteresis (black curve) of a 5 µm thick Cu film, denoted Film A, emphasizes that temperatures would reach up to ~430°C during the experiment. Moreover, the film stress evolution at the beginning of the experiment would emphasize that no thermo-elastic behaviour is present until ~100°C (gradual change of the stress slope).

Using the experimental data of the actual sample temperature (Figure 3a) we computed a polynomial correction function which corrects the stress data in terms of the actual temperature of the Cu films. As one can see from the corrected stress hysteresis, the actual maximum temperature of the Cu film sample during the thermal cycle in the wafer curvature is ~ 400°C instead of 430°C for the measured heating plate temperature. The resulting corrected stress-temperature curvature now reveals a initial thermo-elastic stress response, indicating that the polynomial successfully corrects the measurement artefacts due to imperfect heat transfer between the heating plate and the sample during the thermal cycling.

Infrared Furnace:

Using appropriate heating and cooling rates (10 K/min used in literature), in the wafer curvature on thermal cycle takes about 45 minutes using an appropriate temperature range between 170°C and 400°C. Hence, the wafer curvature set up shows limited applicability for studying the microstructural evolution of Cu films with respect to cyclic thermo-mechanical loading.

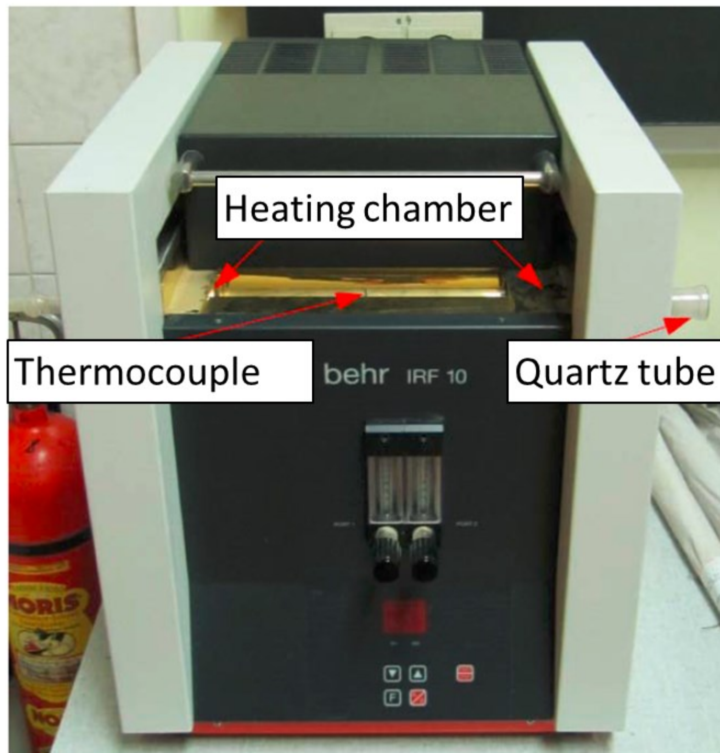

Figure 4: Infrared furnace with strong quartz lamps and a quartz tube containing the sample carriers enables fast thermal cycling in an inert/reductive atmosphere between 170°C and 400°C.

To span the gap between slow thermo-mechanical cycling in the wafer curvature and a rapid pulsed thermal laser cycling set-up an intermediate stage for thermal cycling was developed within the work (see Figure 4). The infrared (IR) furnace is capable of carrying up to nine samples during the fatigue experiment. The heating is performed with quartz lamps heating up the samples indirectly inside sample carriers. To avoid oxidation of the copper surface, a constant gas flow of N_2/H_2 (95vol% N_2) gas mixture of ~1 l/min is used during cycling. The actual time-temperature data during thermal cycling was determined using dummy samples with type K thermocouples brazed to the film surface. This leads to high heating and cooling rates (17K/s and 3K/s) and an

average cycling time of ~ 95 sec (170°C - 400°C) during repetitive thermal cycling. Compared to the wafer curvature set up the IR furnace results in an experimental time saving factor of about 28.

Fast thermal laser cycling device:

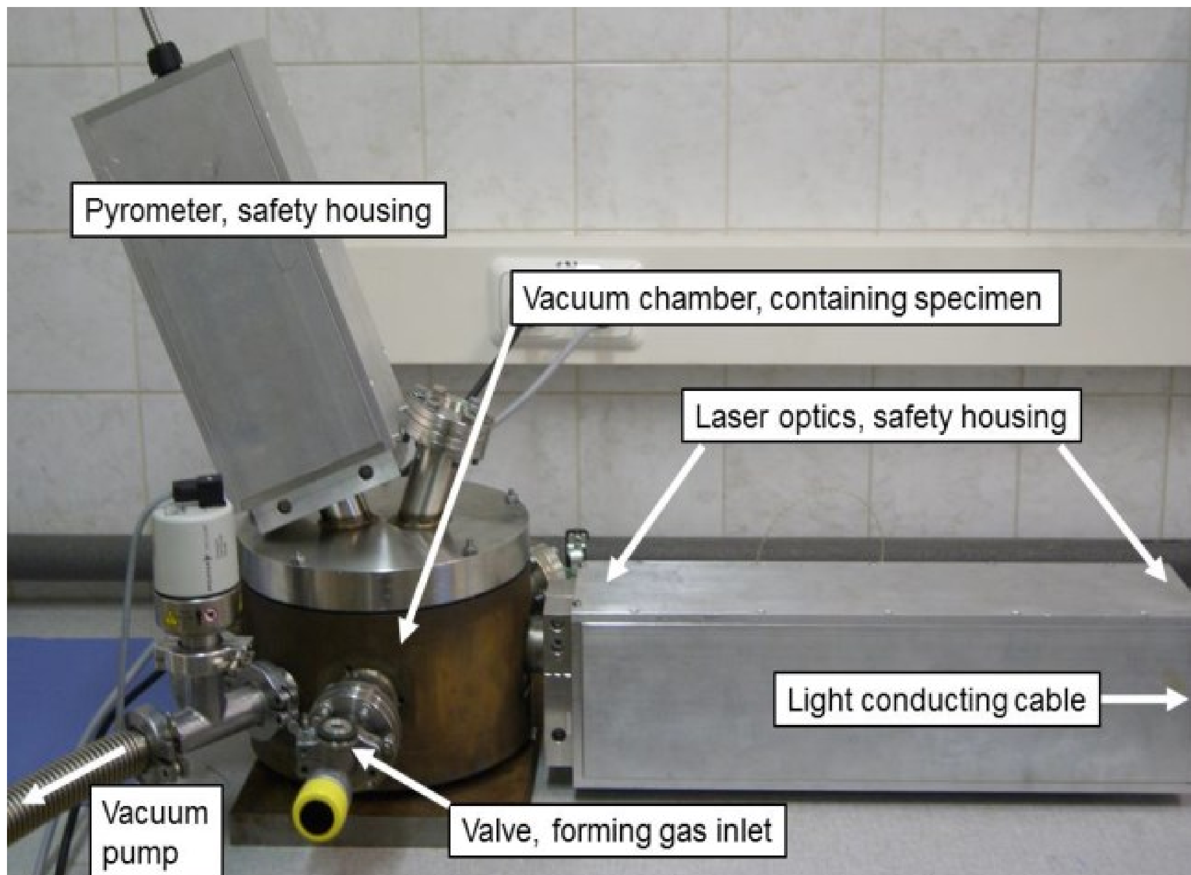

Figure 5: Fast thermal laser cycling device using a 300 Watt near infrared (940 nm) diode laser. Set up consists of a vacuum chamber with a gas inlet, laser optics inside the safety housings and the external temperature control using a pyrometer.

To experimentally simulate fast power pulses and achieve even more realistic cycling conditions, a dedicated thermal laser cycling set up was developed within the experimental frame work. The accelerated thermal cycling method uses a 300 Watt infrared laser, which operates in the near infrared regime at a wavelength of 940 nm. A custom-built safety housing protects the operator from the laser light which is collimated after a glass fibre and then expanded and focused via several optical lenses to enable a defined "top head" laser energy profile (laser energy does not significantly differ with

respect to beam position; no Gaussian laser energy distribution). The laser beam hitting the bottom sample surface (=substrate) using a 45° dielectric mirror and subsequently heats the whole specimen via heat conduction.

The sample temperature is measured in a contact-free way via a pyrometer pointed at the Cu film surface. To adjust the optical properties with respect to the Cu film material and the temperature range sophisticated temperature calibration was performed. Similar as shown for the wafer curvature sample temperature characterization, type K thermocouples mounted in a Cu dummy sample have been used to quantify the corresponding pyrometer detector currents with respect to the thermal cycling temperatures.

The specimen is positioned into a custom-made sample holder with different sample carrier sizes that enable various sample geometries and sizes. During thermal cycling forming gas is used as an inert media where the vacuum chamber pressure is adjusted to about 150 mbar using a membrane pump. A small nozzle next to the sample carrier is used as a gas inlet, enabling effective and fast cooling of the sample via convective heat transfer mechanisms. This allows average heating and cooling rates of ~ 1050 K/sec and ~110 K/sec, respectively. For Cu film samples on thick Si wafers (725 µm) a cycle time of about two seconds (between 170°C and 400°C) is a achieved which results in an experimental time saving factor of about 1350 compared to the wafer curvature set up.

Site specific microstructural characterization

In order to evaluate the on-going microstructural changes of the different Cu films with respect to different thermo-mechanical loading conditions, a new characterization method was implemented. Studying the same surface area with atomic force microscopy (AFM) and electron backscatter diffraction (EBSD) enables a determination of global microstructural parameters, such as surface roughness, grain size, and grain boundary characteristics with cycling, and hence exhibits a great potential for universal microstructural analysis regardless of the loading process.

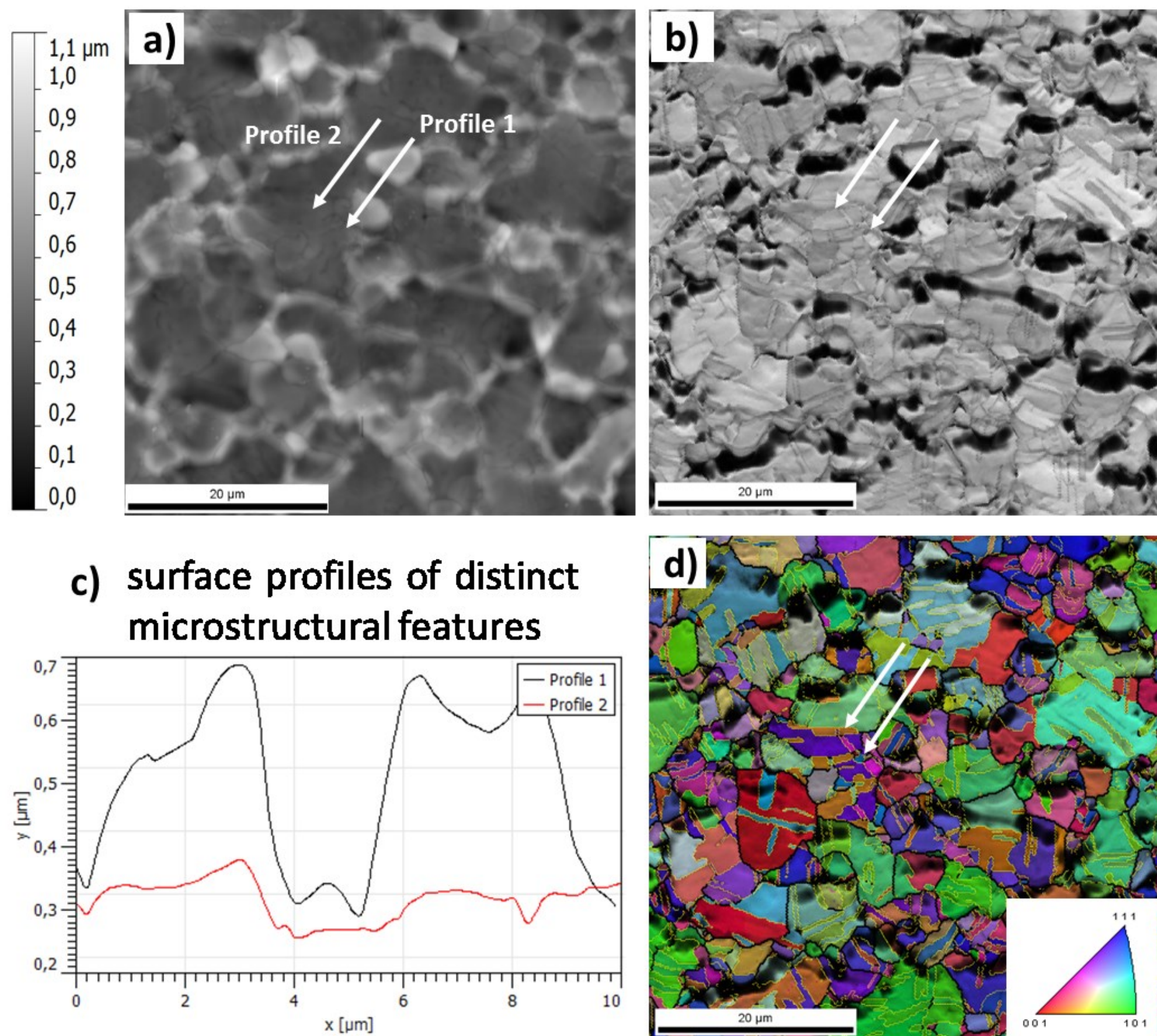

Figure 6: The identical surface sections of a 5 µm thick Cu film on 220 µm Si after 100 thermal cycles are shown by AFM (a) and EBSD (b). Two surface profiles indicate distinctively different microstructural features with regards to the surface topography (c). By applying an inverse pole figure colour code, the crystallographic orientation of the individual grains can be examined (d).

The potential of this characterization approach is illustrated in Figure 6. As one can see from the AFM (Fig 6a) and EBSD (Fig 6b) images it possible to study the microstructural changes of a specific area in terms of the individual fatigue test conditions. Figure 6 presents a 5 µm thick Cu film on 220 µm thick silicon substrate after 100 thermal cycles in the IR furnace.

From the film surface topography it can be observed that certain smaller grains exhibit a distinct sharp uprise. This is also quantitatively confirmed by the surface profile 1 displayed in Fig. 6c. There it can be seen that the grains reveal an uprise in the range of about 400 nm, whereas other microstructural areas do no so shows distinct height

changes (e.g. profile 2). The corresponding EBSD inverse pole figure (IPF) image reveals that the grain orientations of the two neighbouring grains in the profile 2 is very similar (twinned grains with ~ {110} grain orientation). This might explain why there is no roughening at the grain boundary, since the two grains exhibit similar elastic properties during thermo-mechanical loading.

Such example of combining the crystallographic and topographical information emphasizes the great potential for improved understanding of microstructural changes at a local scale. It enables the tracking of specific microstructural features during the entire fatigue experiment and simultaneously tracking the change of quantitative parameters such as grain size, texture and surface roughness. The critical evaluation of such observations could serve as the base for new hypothesis regarding the mechanisms driving fatigue in Cu films used for microelectronic applications.

5 References

[1] G.E. Moore, Electronics 56 (1965) 114-117.

[2] M. Nelhiebel, R. Illing, C. Schreiber, S. Wöhlert, S. Lanzerstorfer, M. Ladurner, C. Kadow, S. Decker, D. Dibra, H. Unterwalcher, M. Rogalli, W. Robl, T. Herzig, M. Poschgan, M. Inselsbacher, M. Glavanovics, S. Fraissé, Microelectronics Reliability 51(9–11) (2011) 1927-1932.

[3] A. Wimmer, M. Smolka, W. Heinz, T. Detzel, W. Robl, C. Motz, V. Eyert, E. Wimmer, F. Jahnel, R. Treichler, Materials Science and Engineering: A 618 (2014) 398-405.

[4] W. Robl, M. Melzl, B. Weidgans, R. Hofmann, M. Stecher, IEEE Transactions on Semiconductor Manufacturing 21(3) (2008) 358-362.

[5] R.P. Vinci, E.M. Zielinski, J.C. Bravman, Thin Solid Films 262(1) (1995) 142-153.

[6] M. Nelhiebel, R. Illing, T. Detzel, S. Wöhlert, B. Auer, S. Lanzerstorfer, M. Rogalli, W. Robl, S. Decker, J. Fugger, M. Ladurner, Microelectronics Reliability 53(9–11) (2013) 1745-1749.

[7] P.A. Flinn, Journal of Materials Research 6(07) (1991) 1498-1501.

[8] M. Stangl, M. Liptak, A. Fletcher, J. Acker, J. Thomas, H. Wendrock, S. Oswald, K. Wetzig, Microelectronic Engineering 85(3) (2008) 534-541.

[9] R. Huang, W. Robl, H. Ceric, T. Detzel, G. Dehm, IEEE transactions on device and materials reliability 10(1) (2010) 47-54.

[10] M. Stangl, V. Dittel, J. Acker, V. Hoffmann, W. Gruner, S. Strehle, K. Wetzig, Applied surface science 252(1) (2005) 158-161.

[11] C.V. Thompson, R. Carel, Materials Science and Engineering: B 32(3) (1995) 211-219.

[12] L.B. Freund, J.A. Floro, E. Chason, Applied Physics Letters 74(14) (1999) 1987-1989.

[13] Y.-L. Lee, Fatigue testing and analysis: theory and practice, Butterworth-Heinemann2005.

[14] P.A. Flinn, D.S. Gardner, W.D. Nix, IEEE Transactions on electron devices 34(3) (1987) 689-699.

[15] N. Thompson, N. Wadsworth, N. Louat, Philosophical Magazine 1(2) (1956) 113-126.

[16] A. Winter, Philosophical Magazine 30(4) (1974) 719-738.

[17] S. Basinski, Z. Basinski, A. Howie, Philosophical magazine 19(161) (1969) 899-924.

[18] F. Ackermann, L.P. Kubin, J. Lepinoux, H. Mughrabi, Acta Metallurgica 32(5) (1984) 715-725.

[19] K. Rasmussen, O.B. Pedersen, Acta Metallurgica 28(11) (1980) 1467-1478.

[20] L. Kunz, P. Lukáš, M. Svoboda, Materials Science and Engineering: A 424(1) (2006) 97-104.

[21] C.V. Thompson, R. Carel, Journal of the Mechanics and Physics of Solids 44(5) (1996) 657-673.

[22] W.D. Nix, Metallurgical transactions A 20(11) (1989) 2217-2245.

[23] T. Kuan, M. Murakami, Metallurgical Transactions A 13(3) (1982) 383-391.

[24] R. Venkatraman, J.C. Bravman, Journal of materials research 7(08) (1992) 2040-2048.

[25] E. Hall, Proceedings of the Physical Society. Section B 64(9) (1951) 747.

[26] N.J. Petch, The Journal of the Iron and Steel Institute 174 (1953) 25-28.

[27] S. Hong, R. Weil, Thin Solid Films 283(1) (1996) 175-181.

[28] D.T. Read, International Journal of Fatigue 20(3) (1998) 203-209.

[29] R. Schwaiger, G. Dehm, O. Kraft, Philosophical Magazine 83(6) (2003) 693-710.

[30] R. Schwaiger, O. Kraft, Fatigue of Thin Silver Films Investigated by Dynamic Microbeam Deflection, MRS Proceedings, Cambridge Univ Press, 1999, p. 201.

[31] H. Merchant, M. Minor, Y. Liu, Journal of Electronic Materials 28(9) (1999) 998-1007.

[32] G. Zhang, C. Volkert, R. Schwaiger, P. Wellner, E. Arzt, O. Kraft, Acta Materialia 54(11) (2006) 3127-3139.

[33] G. Zhang, R. Schwaiger, C. Volkert, O. Kraft, Philosophical Magazine Letters 83(8) (2003) 477-483.

[34] G.P. Zhang, C.A. Volkert, R. Schwaiger, E. Arzt, O. Kraft, Journal of Materials Research 20(01) (2005) 201-207.

[35] W. Heinz, W. Robl, G. Dehm, Microelectronic Engineering 137 (2015) 5-10.

[36] G.P. Zhang, C.A. Volkert, R. Schwaiger, P. Wellner, E. Arzt, O. Kraft, Acta Materialia 54(11) (2006) 3127-3139.

[37] M. Hommel, O. Kraft, E. Arzt, Journal of Materials Research 14(06) (1999) 2373-2376.

[38] O. Kraft, P. Wellner, M. Hommel, R. Schwaiger, E. Arzt, Zeitschrift für Metallkunde 93(5) (2002) 392-400.

[39] S.P. Baker, A. Kretschmann, E. Arzt, Acta Materialia 49(12) (2001) 2145-2160.

[40] P. Sonnweber-Ribic, P. Gruber, G. Dehm, E. Arzt, Acta Materialia 54(15) (2006) 3863-3870.

[41] R. Mönig, R.R. Keller, C.A. Volkert, Review of Scientific Instruments 75(11) (2004) 4997-5004.

[42] R. Mönig, Dissertation, Max Plank Institute (2005).

[43] G.G. Stoney, Proceedings of the Royal Society of London. Series A 82(553) (1909) 172-175.

[44] S. Bigl, W. Heinz, M. Kahn, H. Schoenherr, M.J. Cordill, JOM 67(12) (2015) 2902-2907.

II Summary of work

The response of thin Cu films in the micron and submicron thickness dimensions with respect to cyclic thermo-mechanical loadings has been of great importance for the last several decades to improve the reliability of modern microelectronic devices. The fatigue behaviour of thin films on different substrates has been extensively studied, where the overall greater strength of these films has been explained by the effects of constraint dislocation motion in small grains and geometries. In contrast, only little is known about the fatigue behaviour of Cu films increasing up to several microns in thickness (e.g. 5-20 µm) and its implications for the microstructural properties (incorporated impurities due to new deposition methods).

This work presents results of investigations with respect to the microstructural evolution and the characterization of the corresponding driving forces for material degradation of thick Cu films (≥ 5 µm) on silicon substrates. The implementation of a newly developed thermal laser cycling device enabled experimental investigations of high cyclic thermo-mechanical strain rates (heating/cooling rates) for Cu films with different thicknesses and initial microstructures. The newly implemented site specific microstructural characterization approach by combining topographical (AFM) and crystallographic (EBSD) information allowed novel insights with respect to fatigue mechanisms in Cu films exhibited to repetitive thermo-mechanical loading.

With the newly developed thermal cycling set up(s) and the versatile site specific tracking approach in combination with other characterization approach the following new insights in the field of material science could be obtained:

The microstructure and the subsequent microstructural evolution due to thermal straining is strongly influenced by inorganic residuals in the ppm region. The commonly incorporated Sulphur (S) and Chlorine (Cl) atoms are inevitably bound to modern metallization technologies in power microelectronics. Film A, a Cu film type with dedicated S and Cl incorporation in the ppm region showed that during thermo-mechanical cycling insignificant grain growth with a stable network of twins was present. Furthermore, a constrained roughness evolution with respect to the grain interior (smooth) and the grain boundaries (severe roughening) was observed, indicating

that diffusional processes at the film surface occurred in a restricted manner. It was also found out that Film A exhibited distinct void formation within the film material. In contrast, fatigue testing with the identical thermo-mechanical loading parameters on a pure Cu film, denoted as Film B does result in pronounced twin boundary migration along with grain growth. Moreover, an increase of the (100) texture throughout the thermo-mechanical loading process and no voiding with respect to the film cross-sectional properties was observed. The preferable growth of {100} oriented grains can be mainly attributed to the elastic strain energy minimisation compared to all other crystallographic orientations. The results of fatigue testing led to the conclusion that even small concentration of inorganic impurities distinctively influence the fatigue behaviour. The experimental findings indicate that the pure Cu film system B follows the criteria of energy minimisation whereas Film A, displaying possible challenges in metallization manufacturing, shows a higher risk of fatigue failure due to the higher driving force of void formation.

The problem regarding the incorporation of inorganic impurities was also investigated on a quantitative level using site specific nanoindentation. It has been shown that the incorporation of residual inorganic impurities leads to a distinctively higher hardness at interfaces such as high angle grain boundaries (HAGB) and twins in Film A. Pure Cu films do not show such effects since no segregation of S or Cl can happen in the annealing treatments after film deposition. The obtained results also enabled the explanation of the constrained surface roughness evolution and the marginal grain growth in impure Cu films. Inorganic impurity elements tend to segregate at interfaces such as HAGB and twin boundaries to reduce the surface energy. This leads to a brittle interface and subsequently inhibits other energy minimising processes which occur in pure Cu films.

Moreover, the local nanoindentation experiments led to a phenomenological model with respect to the local topography and the identer tip geometry. Large errors in the obtained hardness can occur when the local topography matches the dimension (tip angle, contact depth) of the indenter tip or when microstructural features lead to imperfect indenter contact situations. The presented experimental results showed that the determination of accurate mechanical properties is coupled with the local contact situation, which

depends on a geometric relationship between the indenter shape (indenter geometry, final contact depth), the surface geometry (curvature, grooves) and the local microstructure (grain boundaries).

The influence of the applied thermal strain rate (heating and cooling rates) during fatigue testing showed that Cu films exhibit a high strain sensitivity with respect to certain microstructural parameters. Greater increase in grain size and surface roughness during thermo-mechanical cycling in both film microstructures was found with respect to higher strain rates. A stronger increase of the {100} out of plane texture component in the pure Cu films (Film B) at higher strain rates indicates that greater elastic stresses must be present to accelerate the mechanisms of elastic strain energy minimisation. Electrical characterisation showed that the increase in sheet resistance in Cu films is mainly dictated by the increase in surface roughness and does not greatly depend on the amount of pores found in the film interior.

Experimental observations on thick Cu films (≥5 µm) showed that thermo-mechanical fatigue is mainly dictated by the texture transition towards the {100} out-of-plane orientation along with a gradual formation of dislocation sub-structures. The results revealed a transition of an orientation independent surface damage (5 µm) to an orientation dependent damage (roughening) for thicker films (10 µm and 20 µm). This was seen in combination with a higher damage tolerance for the {100} oriented grains where such grains exhibited a distinctively lower surface roughness than other orientations. Quantitative surface roughness evaluation revealed a $\sim 1/h_f$ dependency for thicker films (≥ 5 µm) and hence a very different behaviour compared to thin Cu film counterparts (≤ 5 µm).

The investigation of new technological trends such as the reduction of the wafer thickness revealed a strong influence with respect to thermo-mechanical fatigue of Cu films. Experimental findings showed that distinct grain growth coupled with twin migration and accelerated surface roughening was present for Cu films cycled on thin substrates with h_s= 323 and 220 µm. Furthermore, the experimental investigations point out the limits of Stoney´s thin film assumption for the stress characterisation of films on thin substrate materials. Thereby, measurements showed a significantly larger sample

curvature in combination with expected plastic strain gradients in the film material which would explain why an accelerated material degradation is present for Cu films on thinner substrates, although the thermal strain was the same.

To cut a long story short:

With the development of a novel fast thermal laser cycling set up and the usage of newly developed site specific characterisation method the experimental results within this work extended the current understanding of Cu film fatigue with respect to thermo-mechanical loading. Effects of inorganic impurities were investigated on local as well as global scale and the effect was quantified with critical experimental considerations. Experimental effects such as applied strain rates have been studied as well as geometric effects such as film and substrate thickness.

The obtained results and conclusions should serve as a base for material improvements in the microelectronic industry. Furthermore, the high strain rates achieved by the fast laser cycling method revealed new microstructural effects in Cu films and the site-specific characterization enabled the precise investigation of microstructural changes on a global and local scale.

III Short summary of publications

1. Publication A

Site specific microstructural evolution of thermo-mechanically fatigued copper films

To obtain reliable, fast and easy accessible data regarding the microstructural evolution of copper films during thermo-mechanical cycling, a new tracking technique was developed. In order to examine the topographical and crystallographic evolution of the Cu film microstructure, we combined AFM and EBSD analysis of the same surface area during cycling. To guarantee the examination of the identic film surface area, Vickers indents are used as markings, and selective copper oxide etching was applied between thermal cycling. Examples illustrate that the determination of global microstructural parameters, such as grain size, twin boundary length, surface roughness and other characteristics can be shown as a function of cycle number or accumulated thermal strain. The method shows the great potential of studying complex microstructural mechanisms at a local scale. Observations indicate twin boundary migration, topographical evolution of individual grains as well as diffusional mass transport at grain boundaries. The developed method successfully presents a great potential as fast, reliable and universal characterization method regardless of the loading conditions.

2. Publication B

Advanced characterization of thermo-mechanical fatigue mechanisms of different copper film systems for wafer metallizations

The study presents the influence of inorganic residual species in the ppm region on the thermo-mechanical fatigue of Cu films. Two 5 µm thick Cu films with similar initial microstructural parameters are thermally cycled in an infrared furnace. Film A was designed to contain inorganic impurities in the ppm region and Film B resulted in an almost pure Cu film. Distinct differences in the global thermo-mechanical behaviour, using film stress measurements, as well as during microstructural evolution are observed. The impurity-enriched Film A exhibited marginal grain growth, constrained roughness evolution and almost no twin plasticity during thermal cycling. In contrast,

the pure Cu film (Film B) showed distinct grain growth combined with pronounced twin boundary migration and severe roughening of the film surface. Furthermore, preferable texture gain of the {100} out-of-plane orientation is observed, indicating that in pure Cu films strain energy minimizing processes take place. Film A showed a greater elastic regime, quantified by wafer curvature measurements, but exhibited void formation in the film interior. This could lead to crack initiation as well as material failure. The observations underline the influence of film processing related impurities on the thermo-mechanical behaviour of Cu thin films.

3. Publication C

Correlative microstructure and topography informed nanoindentation of copper films

In order to understand and quantify the effect that the residual inorganic species have on grain boundaries, the local mechanical behaviour of 5 µm thick Cu films were investigated with nanoindentation, EBSD and AFM. Film A, designed to incorporate inorganic impurities (mostly S, Cl) in the ppm range and Film B, an almost pure Cu film, were used to investigate the local hardness behaviour with regard to grain boundaries. The influence of surface topography at low indentation loads was taken into account to avoid errors in the hardness measurements. The experiments using low loads revealed that the elastic-plastic behaviour in the grain interior (no boundary involved) is similar for both film systems. At grain boundaries and twins a distinct difference was observed in the mechanical response. Film A showed a significantly higher hardness at twins and grain boundaries, whereas Film B exhibited almost no changes in hardness with respect to grain boundaries. The differences in hardness (factor of ~1.5) can be attributed to the segregated S and Cl atoms forming a strong, partially covalent ionic interface in Film A. The quantitative comparison of the elastic properties of the loading and unloading segments using the Oliver-Pharr method and Hertzian contact mechanics demonstrated that significant errors in hardness determination occur when the indenter tip geometry matches the dimension of the local surface topography.

4. Publication D

Accelerated thermo-mechanical fatigue of copper metallizations studied by pulsed laser heating

In this work a newly developed infrared heating set up is demonstrated for thermal cycling of 5 μm thick films on substrates for microelectronics. In an inert/reductive atmosphere, specimens are heated with a strong infrared laser beam (λ~940 nm) from the substrate, while the in-situ temperature control is performed on the film surface at the same time. The effect of significantly increased heating and cooling rates and, therefore, material strain rates was demonstrated for two copper metallizations, differing in the content of additives. Experimental results showed that an overall accelerated microstructural evolution was found for both films. The higher the heating/cooling rate, the faster the increase of surface roughness and grain size with respect to cycle number was found. The strong increase of the strain minimizing {100} texture component emphasizes that with higher strain rates, greater elastic stresses are reached, which would support the minimization of the elastic strain energy. Furthermore, sheet resistance measurements for both film types emphasized that the increase in resistance is directly proportional to the increase in roughness and is not affected by localized formation of voids in the film interior.

5. Publication E

Film thickness dependent microstructural changes of thick copper metallizations upon thermal fatigue

To satisfy the product requirements of modern power electronics, thick copper metallizations (≥ 5 μm) for lateral heat dissipation are needed. The state of the art literature dedicated most of their research interest to the size effect in thin films. Therefore, pure Cu films in the range of 5 -20 μm on silicon substrates were investigated with respect to thermo-mechanical cycling using a fast laser cycling device. The initial state showed a clear transition towards a dominating {100} texture with increasing film thickness. During thermal cycling all film thicknesses exhibited pronounced grain growth as well as a constant increase of the {100} out of plane orientation. Site specific EBSD during cycling revealed that in {100}-oriented grains dislocation substructures

gradually developed. SEM and surface roughness analysis showed that surfaces damage changes from an orientation independent surface damage (5 µm) to an orientation specific damage (roughening) for thicker films (10 µm and 20 µm). It seems that the {100} oriented grains have a higher thermo-mechanical fatigue damage resistance than differently oriented grains.

6. Publication F

Limits of Stoney's equation: substrate influenced thermo-mechanical fatigue of copper metallizations

The film stress which arises during thermo-mechanical fatigue experiments is almost invariably related to the simple Stoney's curvature-strain relationship. The substrate thickness variation regarding stress determination is neglected due to the comparably small thickness of the deposited metal films. Since current metallization schemes result in thicker films (up to 20 µm) and trends towards thinner substrates in microelectronics are known, we examined the substrate thickness influence with regards to the thermo-mechanical behaviour. The experimental results on 5 µm thick Cu films, cycled in an IR furnace between 170-400°C, presented a substrate thickness dependent microstructure evolution. Accelerated grain growth and surface roughening was found for the thinner substrates. Compared to a substrate thickness of h_s = 541 µm the surface roughness for h_s = 323 and 220 µm was a factor of ~ 3 and ~ 5 greater after 750 thermal cycles. The evaluation of the curvature-strain relations using the wafer curvature method revealed distinct deviations between the expected (calculated) and measured curvature, emphasizing that more sophisticated bending plate theories have to be applied. Laser detector images of the bended thin substrate samples (e.g. 210 µm) showed non-uniform sample curvature and bifurcation confirming the emerging need of more detailed investigations regarding the limits of Stoney´s curvature-strain relation.

IV Publication A

Site specific microstructural evolution of thermo-mechanically fatigued copper Films

Stephan Bigl, Stefan Wurster, Megan J. Cordill, Daniel Kiener

Berg und Hüttenmännische Monatshefte (2015) Vol. 160; Issue 5; 235‑239

Copper metallizations used in modern power semiconductors have to withstand cyclic thermo-mechanical loading over the full operational life-time. Hence, detailed knowledge about the microstructural changes is required to better understand ongoing fatigue mechanisms and specifically to enable improvement of the fabrication process. Therefore, a microstructural characterization method was applied which combines a site-specific analysis using atomic force microscopy (AFM) and electron backscatter diffraction (EBSD) throughout thermal cycling. Studying the same surface area with AFM and EBSD enables a determination of global microstructural parameters, such as surface roughness, grain size, and grain boundary characteristics with cycling, and hence exhibits a great potential for universal microstructural analysis regardless of the loading process. We report about combining topographical and crystallographic information by tracking the identical surface area. Our observations indicate diffusional mass transport at grain boundaries, quantified by height profile evolution, grain growth, and twin boundary migration.

1 Introduction

For modern power semiconductor switches, the key requirements of high current capabilities, high breakthrough voltages, high heat conductivity, and high switching frequencies, are constantly increasing [1]. In current and future power semiconductors, short power pulses during switching operations lead to temporal temperature rise in the device. These short thermal spikes induce thermal stresses due to different thermal expansion coefficients of the various material layers [2-4]. High temperatures and stresses can cause materials to deform plastically, which generates changes in the microstructure and the interface integrity, which leads to degradation in the performance or even failure of the device [5, 6].

With its excellent thermal and electrical properties, copper is the material of choice for metallization layers in semiconductor industry [7, 8]. Previous studies already used electron backscatter diffraction (EBSD) or atomic force microscopy (AFM) for microstructural characterisation of microelectronic thin films [9, 10]. In this contribution a novel tracking technique is presented whereby the same area on the sample was monitored using AFM and EBSD throughout thermal cycling. This enables the correlation between microstructural and topographical evolution of the copper films as a function of cycle number.

2 Experimental

For thermal cycling and subsequent microstructural investigations, electrodeposited copper films with 5µm thickness on (100) Silicon substrate were used.

To experimentally simulate the thermal load caused by a power pulse, the specimens were thermally cycled using an IRF 10 (Behr GmbH, Düsseldorf, Germany) infrared furnace. The heating was performed by a set of strong quartz lamps heating up the samples indirectly inside sample carriers. To avoid oxidation of the copper surface, a constant gas flow of N2/H2 (95vol% N2) gas mixture of about 1l/min was used during cycling. To adjust the parameters in terms of heating and cooling, an external type K thermocouple was brazed onto an extra sample to determine the actual time-temperature data during thermal cycling. Equilibrium conditions for a thermal cycle were reached after about 10 heating cycles (see Figure 1a).

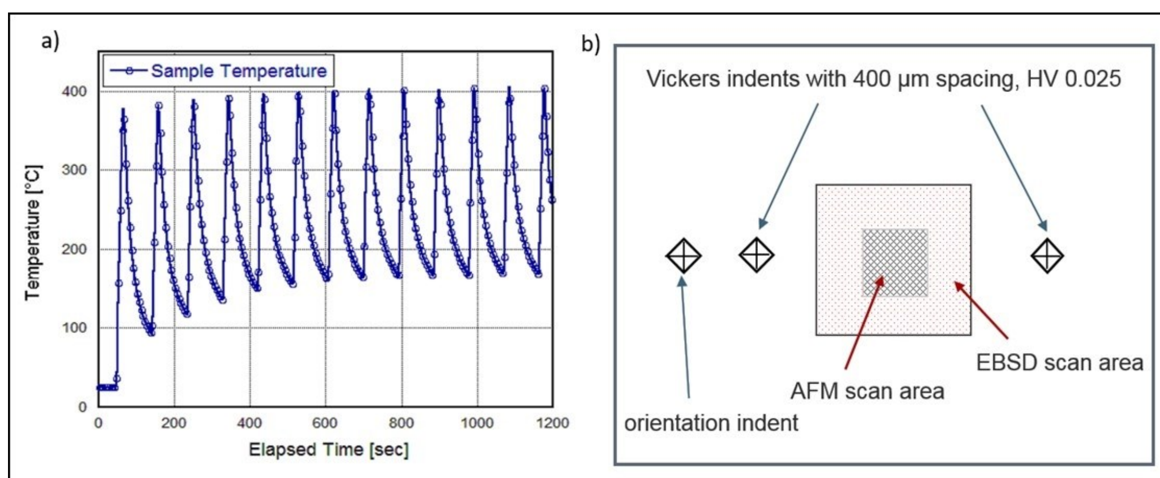

Figure 1: a) Sample temperature during thermal cycling using an infrared furnace. After about ten cycles, an equilibrium state is reached, b) Schematic drawing of the marking technique, showing Vickers indents and scanning areas.

To examine the microstructural evolution of the copper film, a site-specific tracking technique was used (Figure 1b). Using a Vickers hardness indenter, three indents were made to define the area of investigation. The central scanning area was marked with two indents (distance: 400µm) and the third was used as an orientation indent to define the particular scanning direction for the EBSD scan. For the EBSD scans, the settings of 20 kV acceleration voltage and 120µm aperture size were used.

Throughout the thermal cycling process, the marked area was investigated with a Dimension 3100 AFM (Bruker Inc., Billerica, USA) and EBSD using a LEO 1525 (Zeiss Inc., Oberkochen, Germany) scanning electron microscope (SEM). The scanned areas of the AFM images were between 30x30µm² and 50x50µm² with a scan resolution of 512 lines. A further analysis of the AFM scans was performed using Gwyddion 2.36 software [11]. The scan size for the EBSD was between 100x100µm² and 150x150µm², with a step size of 0.2-0.3µm. The EBSD data analysis was performed using TSL OIM Analysis 5 software. For all scans, a confidence index clean-up with a threshold value of 0.07 was performed. To allow microstructural characterisation after several thousand thermal cycles, the specimens were treated with acetic acid after thermal cycling. Hereby, the samples were put into a 100vol% acetic acid at 35-40°C for about 3min. This selectively etches copper oxide to ensure a high quality surface for EBSD analysis.

The actual copper surface is not affected by this etching process [12]. Furthermore, focused ion beam (FIB)-cross-sectioning with a LEO 1540 (Zeiss Inc., Oberkochen, Germany) was used to examine through-thickness diffusion mechanisms. After cutting a large trench with a high ion current of 20nA, fine subsequent polishing steps with 1nA and 100pA resulted in a good quality cross-section of the highly cycled copper film.

3 Results and Discussion

The initial copper film microstructure revealed a root mean square (RMS) roughness of about 14nm and 2.76 ±0.88µm grain diameter, including twin boundaries.

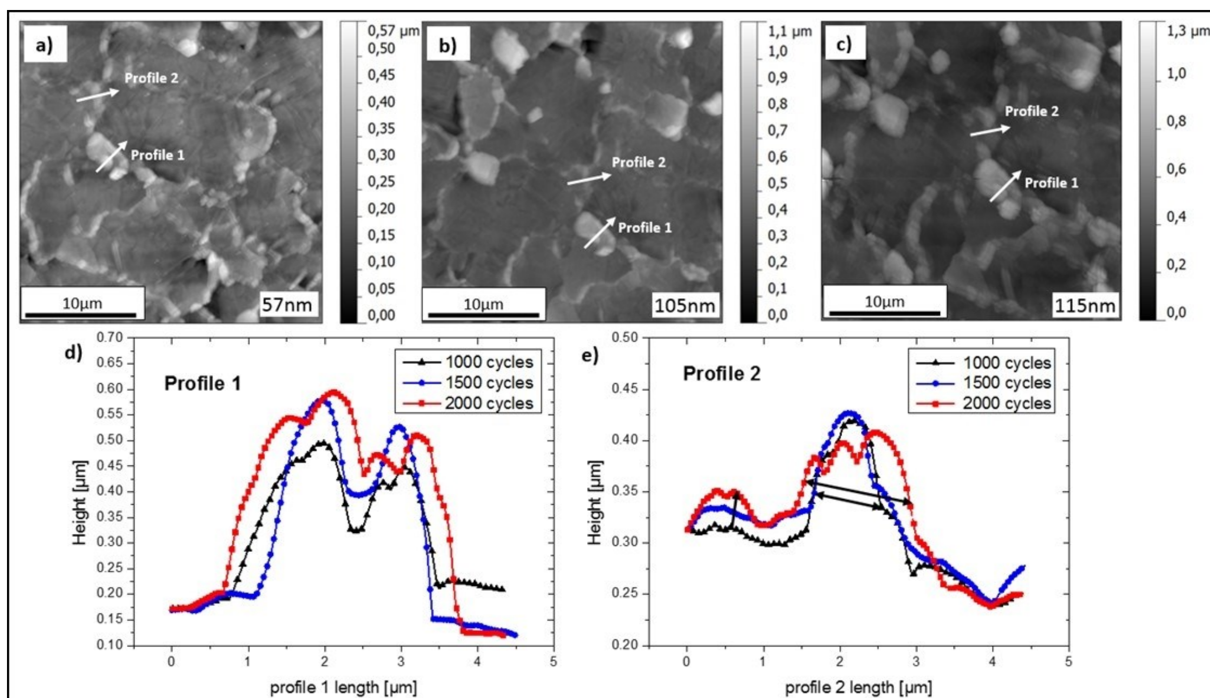

Figure 2: Site specific topographical evolution of thermally cycled copper samples. (a-c) AFM height images after 1000, 1500, and 2000 cycles. (d-e) Topographical evolution of the two selected structural features indicated as Profile 1 and Profile 2

In Figure 2 the capabilities of specific topographical tracking using AFM as an analytical tool for the ongoing cycling process is shown. Figures 2a-c illustrate the topographical evolution of a 30µm by 30µm area of the copper film after 1000, 1500, and 2000 cycles, respectively. Two specific microstructural features were closely examined. Profile 1 indicates a cross-section of a small grain which is increasing in height and broadening in the lateral direction with on-going cycling (2d). As indicated by the arrows, Profile 2 displays the broadening of a formed hill at a grain boundary and the formation of a

smaller hill with increasing cycle number indicating diffusional mass transport (2e). The RMS roughness increases from 57nm at 1000 cycles up to 115nm at 2000 cycles.

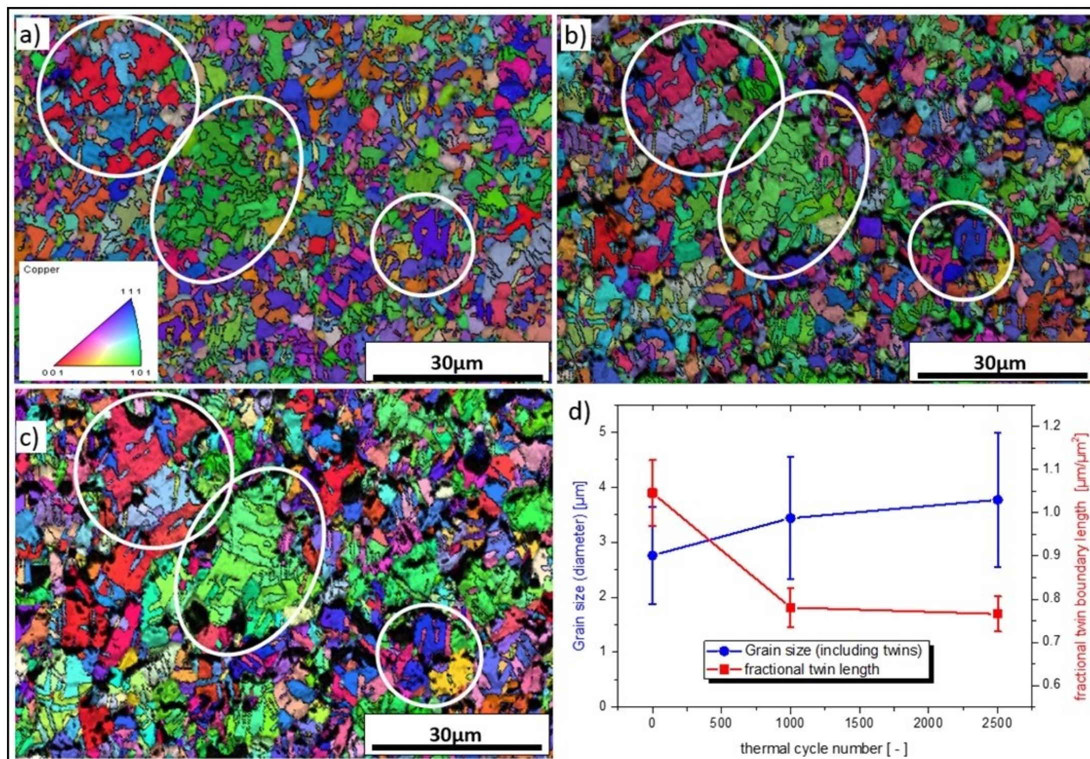

Figure 3: Site specific microstructural evolution using EBSD. (a-c) Inverse pol figure images of the same sample area after 0, 1000, and 2500 cycles. (d) Increase of grain size and decrease of twin boundary length of the tracked area with proceeding cycle number

Figure 3 shows the site-specific tracking of the evolving microstructure using EBSD. Figures 3a-c illustrate the microstructural evolution after 0, 1000, and 2500 cycles using inverse pole figures., The image quality presenting the quality of the diffraction patterns is shown as a grey-scale overlay, and ∑3 grain boundaries are indicated by black lines. As a result of the increasing roughness formed at grain boundaries and by grains growing in the out of plane direction, fewer points can be identified in the EBSD scanning due to diffuse scattering. This results in black spots in the overlaid image quality (Fig 3b, c). There is a notable difference in grain size when 0 cycles are compared to 2500 cycles. The circles highlight three distinctive features of the site-specific EBSD method. Twin boundary migration can be observed in the centre feature (middle circle). After 2500 cycles, the total twin boundary length within the grain is distinctively reduced compared to the as-received state [13]. Figure 3d corroborates this statement, since the grain diameter (including twins as grain boundary) increases from 2.8±0.88 to

3.8±1.22µm, and the fractional twin boundary length decreases from 1.05±0.08 to 0.76±0.04µm/µm^2.

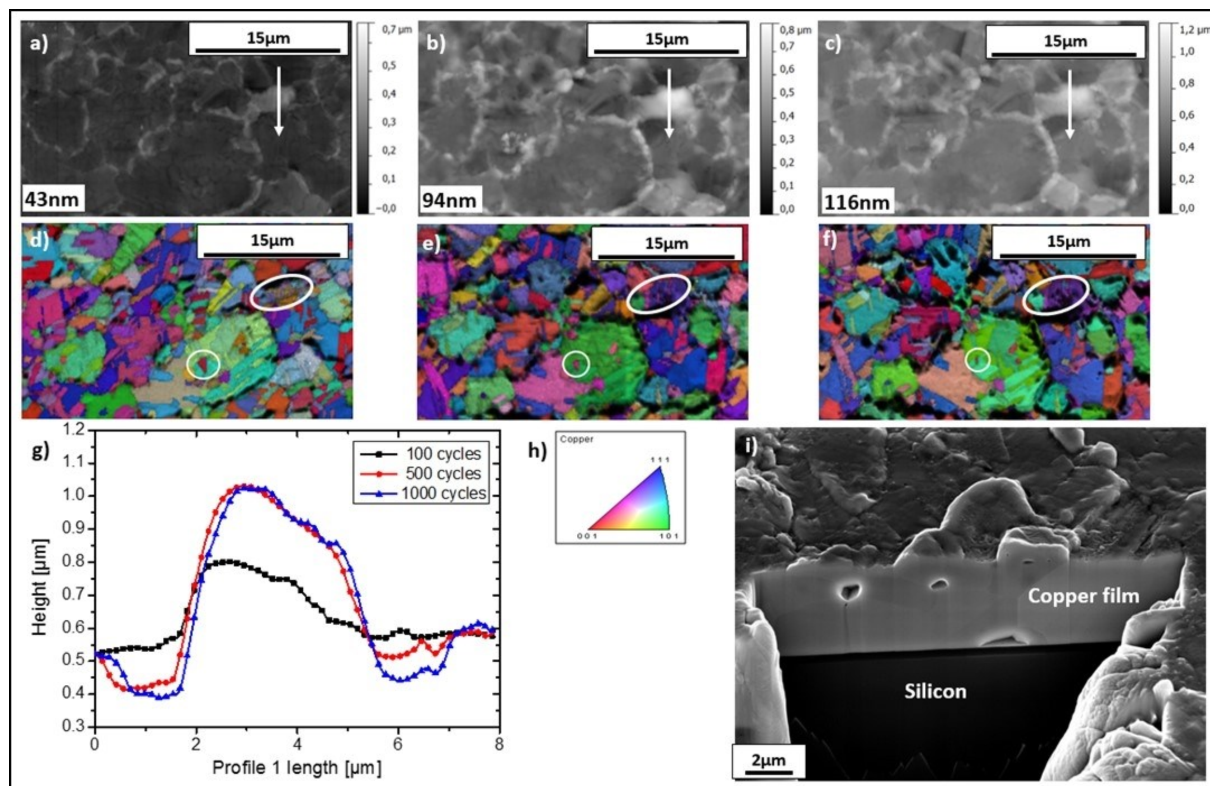

Figure 4: Combined tracking of thermally cycled copper films. (a-c) AFM height images for 100, 500, and 1000 cycles and (d-f) the corresponding EBSD images of the same scan area, with the inverse pole figure colour code given in (h). (g) Height evolution of the large circled twinned grain. (i) FIB cross section of a copper film after 3000 cycles indicating void formation

To underline the advanced tracking technique capabilities, Figure 4 highlights the potential of combining topographical and crystallographic information. Figures 4a-c contain the topographical evolution and corresponding RMS roughness after 100, 500, and 1000 cycles, respectively, matched by EBSD data from the scan area (Figure 4d-f). It can be seen that, even after 100 cycles, a distinct uprising between neighbouring grains takes place (Figure 4b,c). The profile evolution of a heavily purple twinned grain with an approximate orientation of (112) (Figure 4d) shows a growth in height about 400nm from 100 to 500 cycles (Figure 4g), and the profiles indicate mass transport at the two grain boundaries seen by the formation of the two valleys (increase from 500-1000 cycles). In the EBSD images, the selected grain is also growing in the lateral direction. Furthermore, the diminishing of a twinned sub-grain is highlighted (small circle). A FIB cross-section after 3000 cycles displays voids that formed within grains and at grain

boundaries, confirming that a significant proportion of the profile evolution is due to diffusional processes (Figure 4h).

4 Summary and Outlook

We show that specific sample areas can be tracked by AFM and EBSD imaging throughout thermo-mechanical cycling. The tracking method successfully combines topographical and crystallographic evolution of the same surface area to enable better interpretation of microstructural changes. This correlation allows a link between the microstructure and the surface evolution for any kind of mechanical loading. The site specific tracking method enables the precise determination of global structural parameters, such as roughness, average grain size, and grain boundary characteristics. Furthermore, grain boundary migration, reduction of sub-grains, and diffusional mass transport along certain grain boundaries were observed.

Since this site-specific tracking technique represents a universal method, experimental conditions can easily be extended. For example, different temperature ranges during the thermal fatigue experiments will result in an entirely different surface evolution. Using this tracking method will allow the study of shear band formation or any other surface damage, which is then correlated with the crystallographic parameters in a non-destructive manner.

5 Acknowledgements

The work was performed in the project EPPL, financially supported by grants from Austria, Germany, The Netherlands, France, Italy, Portugal, and the ENIAC Joint Undertaking (ENIAC JU Grant Agreement no. 325608). This project is co-funded within the programme “Forschung, Innovation und Technologie für Informationstechnologie” by the Austrian Ministry for Transport, Innovation and Technology.

6 References

[1] Bose, B. K.: Evaluation of Modern Power Semiconductor Devices and Future Trends of Converters, Industry Applications, IEEE Transactions on, 28 (1992), no. 2, 403-413

[2] Nix, W. D.: Mechanical Properties of Thin Films, Metallurgical transactions A, 20 (1989), no. 11, 2217-2245.

[3] Vinci, R.; Zielinski, E.; Bravman, J.: Thermal Strain and Stress in Copper Thin Films, Thin Solid Films, 262 (1995), no. 1, 142-153

[4] Flinn, P. A.; Gardner, D. S.; Nix, W. D.: Measurement and Interpretation of Stress in Aluminum-Based Metallization as a Function of Thermal History, Electron Devices, IEEE Transactions on, 34 (1987), no. 3, 689-699

[5] Zhang, G. P.; Volkert, C. A.; Schwaiger, R.; Mönig, R.; Kraft, O.: Fatigue and Thermal Fatigue Damage Analysis of Thin Metal Films, Microelectronics Reliability, 47 (2007), no. 12, 2007-2013

[6] Evans, A. G.; Hutchinson, J. W.: The Thermomechanical Integrity of Thin Films and Multilayers, Acta Metallurgica et Materialia, 43 (1995), no. 7, 2507-2530

[7] Robl, W.; Melzl, M.; Weidgans, B.; Hofmann, R.; Stecher, M.: Last Metal Copper Metallization for Power Devices, Semiconductor Manufacturing, IEEE Transactions on, 21 (2008), no. 3, 358-362

[8] Lloyd, J. R.; Clemens, J.; Snede, R.: Copper Metallization Reliability, Microelectronics Reliability, 39 (1999), no. 11, 1595-1602

[9] Heinz, W.; Dehm, G.: Grain Resolved Orientation Changes and Texture Evolution in a Thermally Strained Al Film on Si Substrate, Surface and Coatings Technology, 206 (2011), no. 7, 1850-1854.

[10] Lita, A.E.; Sanchez Jr, J.E.: Characterization of Surface Structure in Sputtered Al Films: Correlation to Microstructure Evolution, Journal of applied physics, 85 (1999), no. 2, 876-882

[11] Nečas, D.; Klapetek, P.: Gwyddion: An Open-Source Software for Spm Data Analysis [In English], Central European Journal of Physics, 10 (2012/02/01 2012), no. 1, 181-188

[12] Chavez, K.; Hess, D.: A Novel Method of Etching Copper Oxide Using Acetic Acid, Journal of the Electrochemical Society, 148 (2001), no. 11, G640-G643

[13] Field, D.P.; True, B.W.; Lillo, T.M.; Flinn, J.E.: Observation of Twin Boundary Migration in Copper During Deformation, Materials Science and Engineering: A, 372 (2004), no. 1–2, 173-179

V Publication B

Advanced characterization of thermo-mechanical fatigue mechanisms of different copper film systems for wafer metallizations

Stephan Bigl, Stefan Wurster, Megan J. Cordill, Daniel Kiener

Thin Solid Films (2016) Vol. 612; 153–164

Abstract:

In this study, two different electrodeposited 5 µm thick copper films were subjected to thermal cycling. The microstructural evolution of both films was studied with a site specific tracking technique. It was observed that the initially similar microstructures develop differently upon cycling with respect to grain size and texture. In detail, a Cu film which contains residual inorganic species from the organic additives used during Cu plating, in the ppm regime, showed a constrained surface roughness evolution and marginal grain growth coupled with a stable twin boundary network. Furthermore, voiding in the film interior was observed. In comparison, a high-purity Cu film exhibited strong surface roughening in conjunction with pronounced grain growth promoted by twin boundary migration. Moreover, the film showed a (100) texture intensity increase as a result of strain energy minimization upon cycling and no void formation. These observations underline the influence of film processing related impurities on the thermo-mechanical behaviour of Cu thin films.

1 Introduction

In modern power semiconductor industry, increasing performance, efficiency and reliability are the driving forces for fundamental materials research and new product development. Semiconductor devices are composed of many different material layers, such as dielectric layers, intermetallic diffusion barriers and metallic films [1]. These film materials strongly differ regarding their intrinsic properties, for example, the elastic modulus and the coefficient of thermal expansion (CTE), as well as the structure, which can be crystalline or amorphous. For crystalline metal films, the grain orientations can be randomly distributed or strongly textured. Due to these different structures, the mechanical behaviour can range from strong to soft, or from brittle to ductile [2].

In power devices, extreme electric power densities create fast temperature rises resulting in large thermal stresses due to the CTE mismatch between the different materials. These thermal stresses lead to plastic deformation events, inevitably changing the microstructure of the films. Available literature illustrates that such repetitive thermo-mechanical loading processes cause degradation in the material stack in the form of void formation and crack nucleation, which might grow into the metallization layer or along an interface [3]. In a worst-case scenario, these fatigue defects induce local hot spots and a thermal runaway of the device, because the heat generated by a power pulse can no longer be dissipated throughout the metallization layer. Hence, the integrity of metallizations for power devices play a key role in the operational lifetime and reliability.

In advanced power semiconductor technology, copper is the material of choice for metallization. The outstanding electrical and thermal properties and its reduced susceptibility to electro-migration are a few of the many reasons why copper increasingly substitutes aluminium as a power metal [4, 5]. The necessity of relatively thick metallizations (~5-20 µm) make electrochemical deposition the standard copper deposition process. The high degree of freedom of process parameters and the usage of additives lead to customized film microstructures.

However, electrodeposition processes can result in inorganic impurity levels after deposition and subsequent annealing steps due to the usage of additives in the

electrolyte. Such impurity levels can make up trace amounts, or reach up parts per million (ppm) concentration levels, altering the initial microstructure and surface morphology [6]. Previous studies showed that even trace quantities of inorganic impurity levels have a severe influence on the mechanical behaviour of the films [7, 8], while early research using pure, sputtered Cu films did not study the influence of impurities on the thermo-mechanical behaviour [5, 9, 10]. Therefore, the connection between inorganic impurity levels of electrodeposited films and the corresponding thermo-mechanical behaviour is of great importance, since electrodeposition represents the current industry standard.

In the literature, many different studies report the fatigue behaviour of copper films [11-15]. Such studies often show experimental restrictions, such as free standing copper films [8, 16], or pure mechanical cyclic testing [17-19]. Hence, results are not applicable for Cu metallizations used in semiconductor devices since plastic deformation is always achieved by a combination of thermal activation (thermal energy) and applied stress (mechanical energy) [20]. These previous investigations concluded that fatigue damage evolution of copper films is strongly dependent on film thickness and grain size [13], as well as crystal orientation of the grain [12]. The fatigue events are observed as surface roughening and extrusions formed on the film surface [14]. Furthermore, it is assumed that twin boundaries play a major role regarding the plastic deformation that acts as a non-regenerative dislocation source [21], and could serve as sites for void nucleation. Most of these studies do not resolve the on-going mechanisms throughout the fatigue experiment, hence making interpretation of results difficult. Therefore, the understanding of microstructural changes with respect to the remaining impurities in the copper layers upon cyclic thermo-mechanical loading is of fundamental importance to predict and improve lifetime and reliability of microelectronic devices.

In this work, experimental results of two different thermo-mechanically fatigued electrodeposited copper films are presented. One film system (Film A) was designed to contain relatively high amounts of inorganic impurities (mostly sulphur and chlorine), while the second film system (Film B) was processed resulting in a significantly lower amount of inorganic impurities. The experimental evaluation of the fatigue mechanism(s) was performed, using a site specific tracking technique [22].

Microstructural evolution was investigated by combining topographical information using atomic force microscopy (AFM) and crystallographic information with electron backscatter diffraction (EBSD) throughout the thermal fatigue experiment. This enabled the study of global structural parameters like roughness, average grain size and grain boundary characteristics, as well as investigate distinct microstructural features displaying twin grain boundary migration, grain growth, and diffusional mass transport along certain grain boundaries, throughout the thermo-mechanical loading experiment. The observations were then critically evaluated regarding the influence of inorganic impurities on the microstructural evolution.

2 Materials

For all of the presented data, 5 µm thick electrochemically deposited polycrystalline copper films were used. The two copper film systems where deposited on 725 µm thick silicon wafers of (100) orientation. As a diffusion barrier, a few nanometers thick tungsten-based layer was used followed by a 300 nm Cu seedlayer. After electrodeposition, a 30 min annealing step at 400 °C in an inert atmosphere was performed to ensure a room temperature stable microstructure. Film A was designed to result in a copper film with a high remaining inorganic impurity content (≤ 100 at ppm), and Film B resulted in an almost impurity-free copper film. For more details see [7].

3 Experimental

For an experimental imitation of the thermo-mechanical load in the copper films induced by the high power density in semiconductor devices, the samples were thermally cycled in an infrared furnace (IRF 10, Behr GmbH, Düsseldorf, Germany). The specimens were cut from a 200 mm wafer measuring about 5 mm x 10 mm and heated indirectly via strong quartz lamps in customized sample carriers. Using K type thermocouples brazed onto extra samples, the film temperature during the programmed temperature cycle was monitored. All specimens in this publication were subjected to thermal cycles between 170 °C and 400 °C. This results in a total applied strain due to the CTE mismatch per cycle of about 0.7% when using the average CTE values for Cu and Si in the corresponding temperature range [23, 24].

The basic thermo-mechanical characterisation of both films was performed using a wafer curvature system for in-situ film stress characterisation up to 1000 °C [25]. With a multiple optical beam sensor, kSA MOS (k-Space Associates, Inc. Dexter, 48130 USA) the film stress evolution was measured between room temperature to 400°C using a heating and cooling rate of 10°C/min.

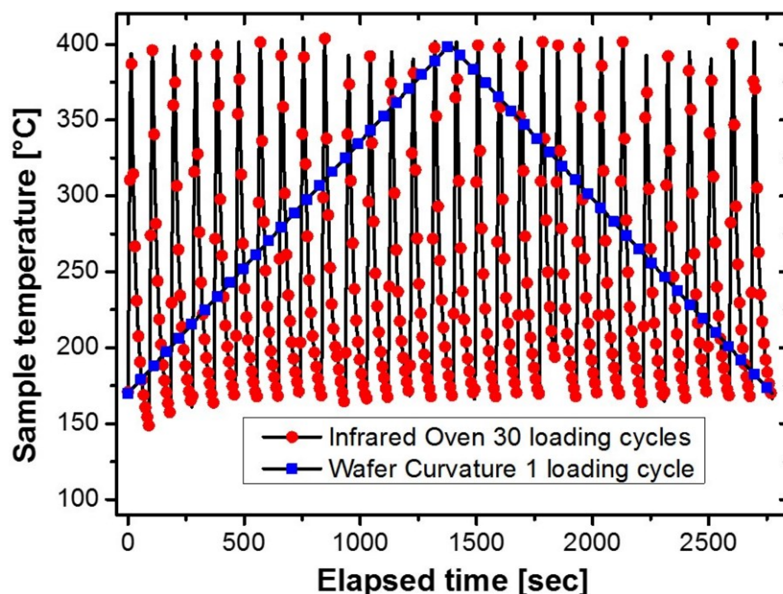

Figure 1: Comparison of the sample temperature-time response in a conventional wafer curvature experiment and the fast thermal cycling in an infrared furnace between 170°C and 400°C

Figure 1 shows a direct comparison of the time-temperature relation between a conventional wafer curvature experiment using a heating rate of 10 °C/min and the programmed thermal cycle in the infrared furnace (IRF) for the desired temperature range of 170 – 400 °C. Thereby, 30 cycles are achieved in the IRF, whereas in the same time span only one thermal cycle is performed in the Wafer curvature, indicating accelerated fatigue testing with respect to testing time. One thermal cycle corresponds to an average heating rate of 17 °C/sec (from 170 °C to 400 °C) and 3 °C/s cooling rate (from 400°C to 170°C) with a total cycle time of about 95 s. During the cycling process in the IRF a constant gas flow of N_2/H_2 (95vol% N_2) gas mixture of ~ 1 l/min through a quartz tube containing the specimens was used to minimize oxidation of the copper surface.

For thermal fatigue investigations of the copper films during the cycling process a surface area-specific tracking technique was used. A representative surface area was

marked with orientation indents (Vickers micro indents HV 0.02 & HV 0.05), to ensure the tracking of the identical film area throughout the whole experiment. The investigations were performed regarding microstructural evolution using EBSD and topographical evolution using AFM. A more detailed description of the applied technique and its features can be found in [22].

Using a Dimension 3100 AFM (Bruker Inc., Billerica, USA) and a scanning electron microscope (SEM) LEO 1525 (Zeiss Inc., Oberkochen, Germany) for EBSD analysis, specimens were examined throughout the thermal cycling process. AFM height images were between 30x30 µm² and 50x50 µm² in size with a scan resolution of 512 lines. AFM post image analysis was performed using Gwyddion 2.36 software [26]. The EBSD scans resulted in a scan size between 100x100 µm² and 150x150 µm², using a step size of 0.2-0.3 µm. The EBSD scanned area incorporated the AFM scanned area. For all EBSD scans 20 kV acceleration voltage and 120 µm aperture size were used. EBSD data analysis was performed using TSL OIM Analysis 5 software. For correct grain definition, identified pixels had a 15° tolerance angle and a minimum grain size of 3 pixels. For the presented inverse pole figure (IPF) images, overlaid with the image quality (IQ), a confidence index clean-up with a threshold value of 0.07 was performed. To reveal through-thickness fatigue mechanisms, film cross-sections were prepared using dual beam focused ion beam (FIB) workstations, either with a LEO 1540 (Zeiss Inc., Oberkochen, Germany) or an Auriga SEM equipped with Cu ion FIB (Zeiss Inc., Oberkochen, Germany). After cutting a large trench with an ion current of 20 nA, subsequent fine polishing steps with 1 nA and 100 pA produced a good quality for cross-section imaging of the cycled copper films. To maintain the surface quality needed for AFM and EBSD characterisation after several thousand thermal cycles, the specimens were treated with acetic acid after thermal cycling. Samples were put into a 100 vol% acetic acid at 35-40 °C for ~ 3 min, which selectively etches copper oxide and does not affect the actual copper surface [27].

4 Results

Figure 2 displays the initial microstructure of the two film systems. The 50 x 50 µm IPF-IQ images reveal the microstructural characteristics of the two films. The IPF standard triangle, used for every EBSD image in this work, can be found in Figure 6d.

For better illustration of the microstructure white lines (excluding ∑3 and ∑9) in Fig. 2 indicate high angle grain boundaries (HAGB, >15°), whereas black lines indicate primary (coherent and incoherent) twin boundaries (∑3). In both samples, low angle grain boundaries (red lines) and secondary twin boundaries (grey lines, ∑9) make up a negligible contribution to the total grain boundary characteristics.

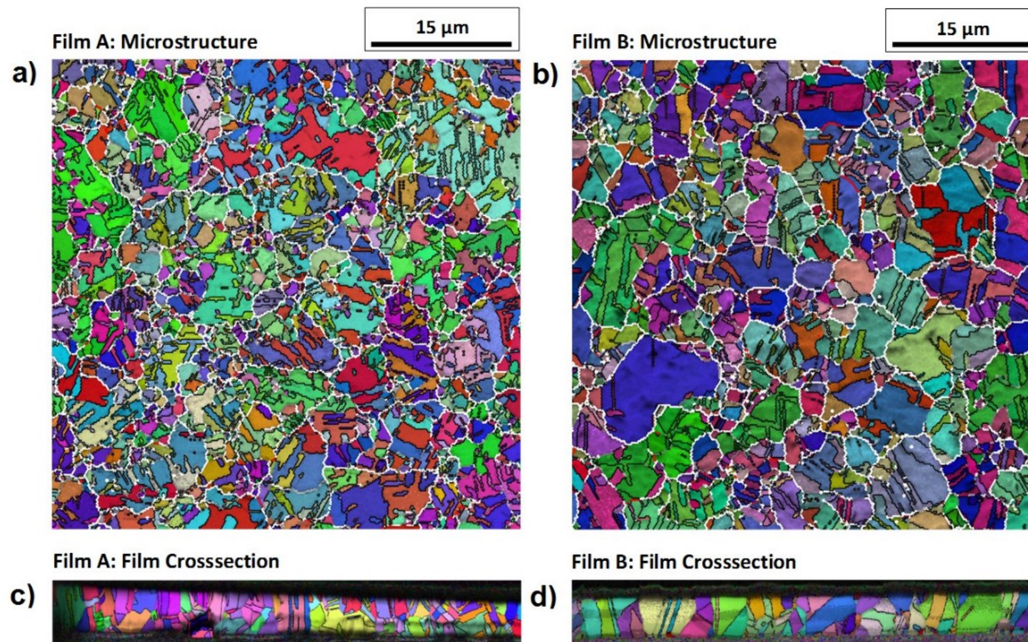

Figure 2: Initial surface microstructure of Film A (a) and B (b), where grain boundaries (white lines) and twins (black lines) are indicated. (c-d) Cross-sectional microstructure, where only twins are indicated (black lines).

Both film systems reveal a polycrystalline microstructure where the grains possess a significant portion of twin boundaries. The main microstructural distinction is that Film A has a higher initial fraction of twins than Film B, which can be also seen through the entire film thickness (Fig. 2c, d). The average initial grain size, including the twin boundaries resulted in 2.8 ± 0.9 µm for Film A and 3.2 ± 1.1 µm for Film B. Concerning the texture, both sample types reveal an almost randomly orientated polycrystalline microstructure with no preferable crystal orientation. Using the elastic constants of the stiffness tensor for copper (c_{11}: 168.4 GPa, c_{12}: 121.4 GPa c_{44}: 75.4 GPa) [28] the elastic modulus distribution and the mean elastic modulus of the initial scanned surface area was determined using the OIM Analysis software. The calculated elastic modulus is 110 ± 31 GPa for Film A and 112 ± 30 GPa for Film B. For determining the elastic modulus of absolutely randomly oriented copper, being equivalent to texture-less polycrystalline

copper, a custom EBSD scan file was generated and analysed, where the result for the average Young´s modulus was 109 GPa.

To evaluate the basic thermo-mechanical behaviour of the two sample types, film stresses were measured with wafer curvature. Figure 3 shows the stress vs. temperature evolution of Films A and B. The first cycle (starting from room temperature) and second cycle (80-400 °C) are plotted in comparison to the stress behaviour of the same samples after being exposed to 80 thermal cycles between 170 °C to 400 °C in the IRF. It can be seen that the evolving stresses in the initial cycle differ strongly between Film A and B. Film A (Fig. 3a) shows a very pronounced linear elastic behaviour between room temperature and about 100 °C, whereas Film B (Fig. 3b) deviates from a pure elastic behaviour around 75 °C. This can also be seen in the stress evolution at higher temperature, where Film B stresses relax at temperatures around 200 °C, compared to about 250 °C in Film A. Overall, Film A thermo-mechanically behaves stiffer (steeper thermo-elastic slope) and stronger (higher tensile flow stress, similar compressive flow stress) compared to the more compliant and softer Film B.

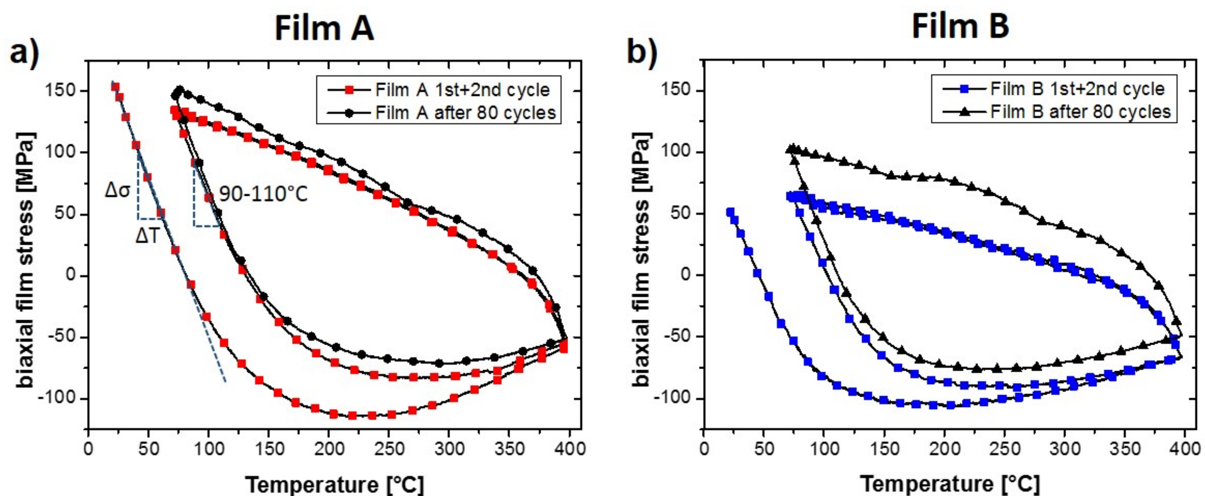

Figure 3: Basic thermo-mechanical behaviour of (a) Film A and (b) Film B between room temperature and 400°C.

The same behaviour can be observed in the second cycle starting from 80 °C. Treating the initial linear stress decrease as a pure elastic phenomenon due to the thermal expansion mismatch between Cu and Si, the stress slope $d\sigma_f/dT$ can be described as following [29]:

$$\frac{d\sigma_f}{dT} = \left[\frac{E_f}{(1-v_f)}\right] * (\alpha_s - \alpha_f). \qquad (1)$$

The stress slope is the product between the biaxial modulus of the film, where E_f denotes elastic modulus and v_f the Poisson's ratio of the film, and the expansion mismatch between the substrate α_s and the film α_f. Determining the thermo-elastic slope for both samples between 90 and 110 °C, Film A results in -2.49 MPa/°C and Film B in -2.09 MPa/°C. Using the elastic moduli for A and B determined from the EBSD, the average CTE value of 3.28 ppm/K for silicon in the corresponding temperature range and 0.35 as the Poisson´s ratio for polycrystalline copper, results in CTE values for Cu of 17.8 ppm/K and 15.3 ppm/K for Film A and B [24, 28]. Film A displays an almost perfect correlation to literature data of measured thermal expansion, which is ~ 17.4 ppm/K in the corresponding temperature region [23]. Film B results in a lower equivalent CTE value and deviates from the literature bulk value.

A clearer picture of the CTE can be obtained when Film A and B are compared after 80 thermal cycles in the IRF. Figure 3 indicates that in both film systems the stress hysteresis is shifted towards the tensile stress state. Besides this shift, the elasto-plastic behaviour of Film A itself remained unchanged, but for Film B the thermo-mechanical behaviour changes as function of cycle number. The elastic regime becomes more pronounced, which can be seen in the initial heating and cooling after reaching 400 °C in the 80th cycle, indicating that the stress-temperature evolution in Film B approaches that of Film A. This is also found in the thermo-elastic behaviour, where the slope of Film B between 90-110 °C results in -2.51 MPa/°C compared to -2.63 MPa/°C for Film A. Hence, the obtained wafer curvature results of the two film systems indicate that Film A and B exhibit a different global thermo-mechanical behaviour, although starting with very similar initial microstructures. Therefore, there is a need for a closer look during the cycling to illustrate the on-going microstructural changes, which will enable the classification of the present fatigue mechanisms in the two film systems.

For the global characterization of the copper film evolution, the grain size, including the twins as grain boundaries, the fractional twin boundary length, the root mean square (RMS) surface roughness and the normalized texture intensity in the (100) out of plane crystal direction, were examined between the initial stage and 3500 thermal cycles.

In Figure 4a and 4b, a direct comparison of the two film systems regarding their grain structure development can be found. The grain diameter (with corresponding standard deviation) is very similar at the beginning, however, the grain size evolution throughout cycling significantly deviates. Film A shows a slight increase of the grain size. Starting from 2.8 ± 0.9 µm, the grain size increased up to 3.9 ± 1.2 µm after 3500 thermal cycles. In Film B, significant grain growth can be observed in the initial 1000 cycles, increasing the grain diameter from 3.2 ± 1.1 µm up to 5.1± 1.7 µm. Further cycling led to a final grain size of 5.8 ± 1.9 µm after 3500 cycles.

The evolution of the fractional twin boundary length (including measurement uncertainty) is also presented in Figure 4a, b, where the total measured twin boundary length is divided by the total scan area. This gives a quantitative parameter regarding the twin boundary evolution and can be used to evaluate the on-going plastic deformation. For example, Film A started with about 1.05 ±0.08 μm^{-1} fractional twin length which decreased to 0.78 ±0.07 μm^{-1} in the first 1000 cycles. This indicates a diminishing of twin boundaries, while the following 2500 cycles show a relatively stable twin boundary length resulting in 0.86 ±0.06 μm^{-1} final fractional length. Film B reveals an approximately 26% lower initial fractional twin boundary length of 0.83 ±0.07 μm^{-1}, which can be also seen qualitatively in Figure 2. The fractional twin length strongly decreased to 0.57 ±0.05 μm^{-1} after 1000 cycles and is further reduced to a final fractional length of 0.35 ±0.04 μm^{-1} after 3500 cycles. In direct comparison, the two film systems reveal quite different microstructural evolution. Film B shows an almost 100% increase of the average grain diameter, which is due to a continuous decrease of twin boundaries by more than a factor of two after 3500 cycles. On the contrary, Film A exhibits an increase of the grain size of only 40% and the initially decreasing twin boundary length remains constant after ~ 1000 cycles.

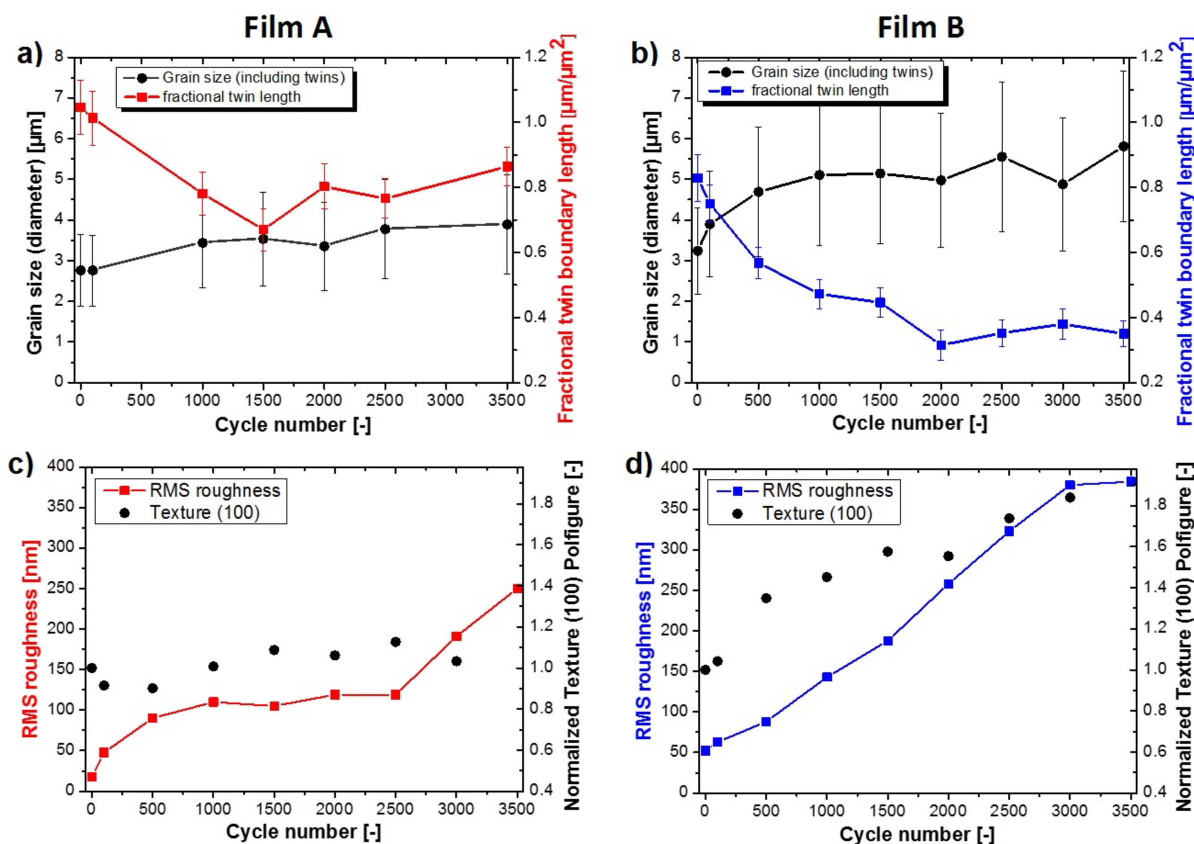

Figure 4: (a, b) Grain size and fractional twin boundary length evolution for Film A and Film B as a function of cycle number. (c, d) Surface roughness development and evolution of the (100) texture intensity for Film A and Film B, respectively.

Figures 4c-d present the topographical evolution, given by the RMS surface roughness and the texture evolution of the (100)-texture. The RMS roughness gives a quantitative parameter in regards to the height evolution due to mass transport or deformation event. The (100) texture was chosen because grains with a low biaxial modulus are preferred to grow in order to minimize the strain energy, thus giving an orientation-specific driving force which could influence the texture evolution [30]. The (100)-texture is presented perpendicular to the loading direction, since the thermo-mechanical loading generates stresses in the in-plane direction of the copper films.

Film A starts with an initially flat surface of ~ 17 nm RMS roughness, which increases up to ~ 100 nm after 1000 cycles. The surface roughening is then continued through cycling up to 250 nm, although with not much change between 1000 and 2500 cycles. Film B starts with an initially wavier surface of ~ 52 nm RMS roughness, which linearly increases throughout the fatigue experiment up to 384 nm. Both film systems show that throughout the cycling severe surface roughening occurs. Nevertheless, Film B has a 50

% rougher surface than Film A, indicating that more plastic deformation can be observed on the free film surface.

With respect to texture evolution, the analysis was performed identically for both film systems. The texture intensity regarding the (100)-texture was determined using the technique of series expansion of generalized spherical harmonics, a tool which is incorporated in the OIM software. All scans were analysed using 16 as the order of series expansion and 5° as the Gaussian half-width, a parameter for smoothing the texture plot. The obtained maximum intensity values (equivalent to a statistical probability) for each cycling stage were then normalized with regards to the value of the initial microstructure. There, Film A had 2.4, as absolute (100)-texture intensity and Film B 1.6. Film A reveals no change of the intensity of the (100)-texture throughout the cycling. In the case of Film B, the intensity of the out of plane orientation increased by a factor of 1.8, demonstrating that the thermo-mechanical loading leads to a texture change in the film.

Because of the global changes seen in Figure 4, a more specific and local investigation of the fatigue evolution is necessary. This would enable a correct interpretation of the presented global results, revealing the microstructural mechanism on the local scale for films A and B. Since excessive changes were observed in the first 1000 cycles, Figure 5 shows the combination of EBSD (Figure 5a-c) and AFM (Figure 5d-f) images of Film A for 0, 500 and 1000 cycles. Additionally, three height profiles (Figure 5g-i) are shown to reveal the height evolution for certain microstructural features. It should be pointed out that slight colour changes can be observed from one to another cycle stage in the EBSD image. This is due to the fact that even minor changes in the sample-detector alignment upon sample mounting can have an impact on the colour appearance of the grains. In the initial film topography (Figure 5d) Film A exhibits a very flat surface with pronounced grooves at high angle grain boundaries, as well as grooves at the twinned interfaces. The corresponding EBSD image (Figure 5a) shows that the initial microstructure is composed of fine grains with a strongly twinned substructure (black lines). Therefore, many grains consist of multiple twin configurations, indicating that more than one parent/twin configuration is present. The topographical evolution shows that after 500 cycles (Figure 5e) sharp elevations at the grain boundaries formed, as well

as distinct uprising of grains, which are further evolving in the subsequent cycles (Figure 5f). For example Profile 1 (Figure 5g) displays the uprise of two small twinned grains. After 1000 cycles, the two grains show a 250 nm difference in height compared to the surrounding grains. Profile 2 (Figure 5h) presents the interface evolution between neighbouring grains. In the three profiles, it can be seen that starting from a flat surface (0 cycles) with some grooves at the grain boundaries (purple line), severe hillocks formed. These pronounced walls rise up to about 400 nm after 1000 cycles. From the AFM images and the profile sections it can also be observed that mass transport of the in-between lying approximate (100)/(212)-twinned grain to the neighbouring grains forms these hillock-like features. Furthermore, the profile sections indicate that grain growth in Film A is hindered. It can be seen that the positions of evolving features do not change throughout the cycling process. In Profile 3 (Figure 5i), the topographical evolution between small grains can be observed. A large height gain evolves between two grains sharing a small angle grain boundary (position at 6 µm in Profile 3). It can be seen that deep grain boundary grooves develop due to diffusional mass transport from one grain to another grain. Notably, in all profiles no significant topographical evolution between 500 and 1000 cycles was observed. This is in accordance with the global RMS roughness evolution shown in Figure 4c.

For a more detailed interpretation of the microstructural changes of Film A during the initial thermo-mechanical loading process, Figure 6 presents a more localized depiction of the microstructural evolution of Film A between 0 and 1000 cycles. As a result of the increasing roughness formed at grain boundaries and growing grains in the out of plane direction, fewer points can be identified in the EBSD scanning in the later stage. This results in black areas due to the overlaid image quality and is present in all scans that do not display the initial microstructure. Despite the moderate grain growth and greater microstructural stability in Film A, certain crystallographic mechanisms can be identified. Therefore, five distinct microstructural features are labelled with numbers in the in the EBSD images (Figure 6a-c) to indicate these mechanisms in the early stage of fatigue (0-1000 cycles).

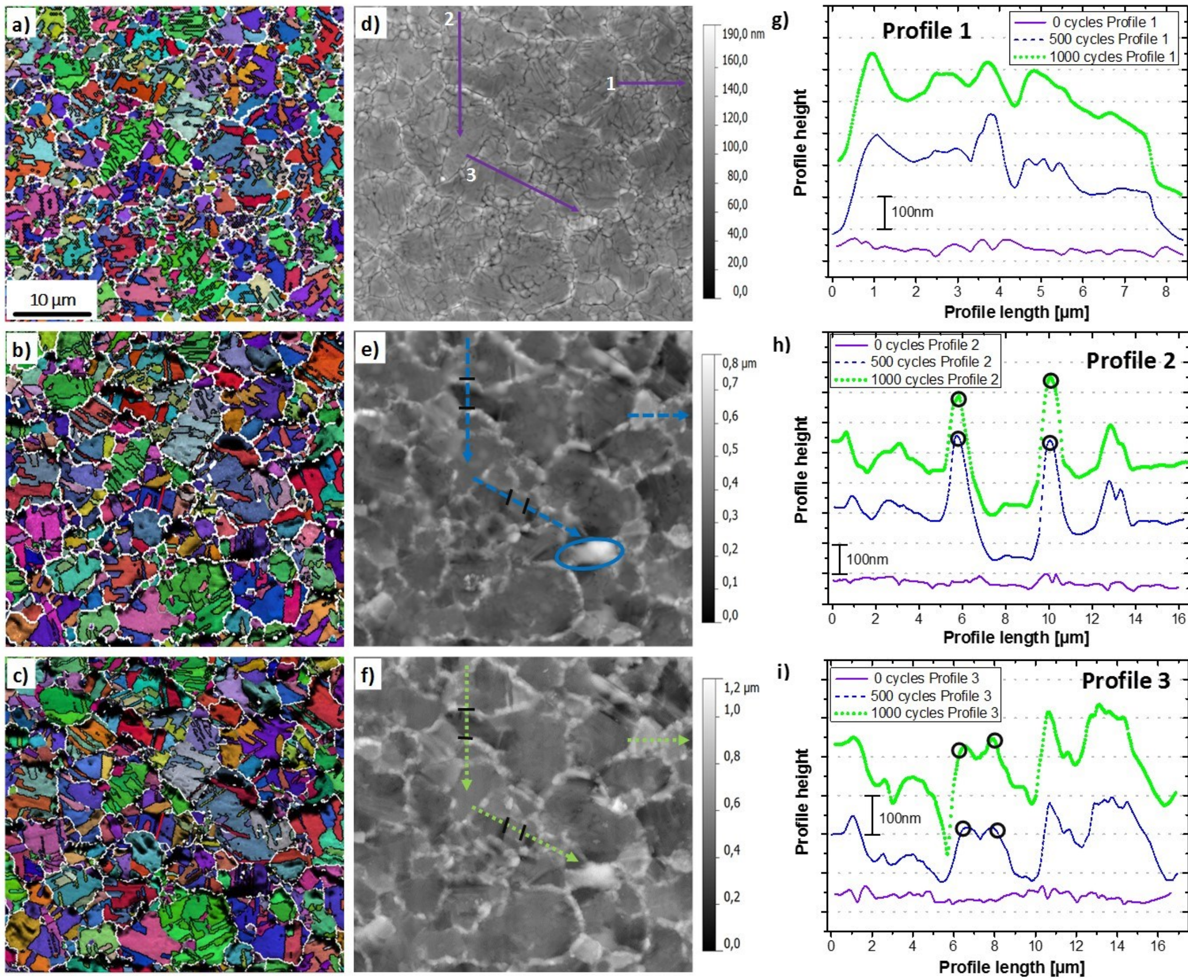

Figure 5: Early site specific microstructural evolution of Film A. Crystallographic evolution (a-c) is matched by the topographical evolution (d-f) of the same surface area for 0, 500 and 1000 cycles. Additionally, three selected microstructural features are examined regarding their topographical evolution, indicated by Profile 1-3 (g-i).

It can be seen that grain growth is achieved by certain twin/parent configurations in Film A. Grain growth is achieved via twin boundary migration (Feature 3), twinning/detwinning (Feature 2, 5), as well as distinct formation of new twin configurations (Feature 1). Additionally, localized roughening in the form of the uprise of Feature 1 can be observed, as identified in Figure 5e-f. The majority of grains show insignificant microstructural changes (Feature 4), where no microstructural changes occur, especially comparing 500 and 1000 cycles.

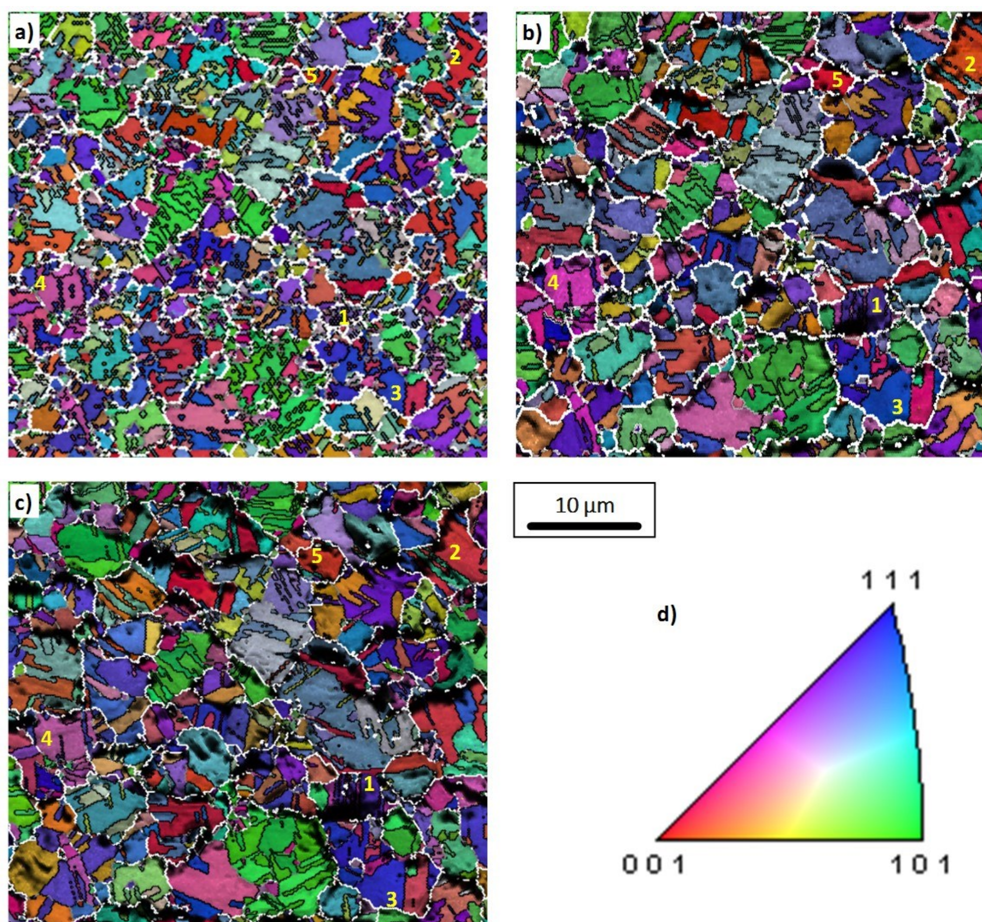

Figure 6: Microstructural evolution of Film A. The IPF images overlaid with the image quality display the changes in respect to the cycling stage of 0, 500 and 1000 thermal cycles (a-c). Five distinct microstructural feature are highlighted to describe the changes in Film A during thermo-mechanical loads in (b). See text for details.

Figure 7 highlights the site specific microstructural changes in the first 1000 thermal cycles of Film B. As for Film A, the crystallographic evolution (Figure 5a-c) is matched by the topographical evolution (Figure 7d-f) for 0, 500 and 1000 loading cycles. Three profile sections indicate the topographical evolution of distinct microstructural features. Additionally, four selected features are marked in the intermediate cycling stage (Figure 7b), used to describe the on-going microstructural changes in detail. The initial microstructure for Film B consists of small grains composed of many different twin configurations, similar to Film A. The deposition process resulted in a wavier and rougher film surface. From a film morphology point of view, the grains with high angle boundaries reveal grooves at the interfaces, which are matched with the boundaries (white lines) in the EBSD section (Figure 7a), although the twinned regions in Film B do not show such pronounced grooves as seen in Film A. As indicated in the

topographical evolution of Profile 1, grain growth is active throughout the thermo-mechanical cycling, as the distance between the peaks of the walls increases. By examining the profile section at the HAGB interface, it can be seen that the particular grain is growing continuously. A distinct uprise of the grain interface can be observed, although surface roughening is also occurring within the grain. Profile 2 highlights the uprise and growth of a small lamella twinned grain. After 1000 cycles the grain shows a distinct uprise of about 400 nm. Profile 3 displays the height evolution of several neighbouring small twinned grains. The profiles indicate that during the cycling the region is laterally shrinking, but a significant height evolution is observed.

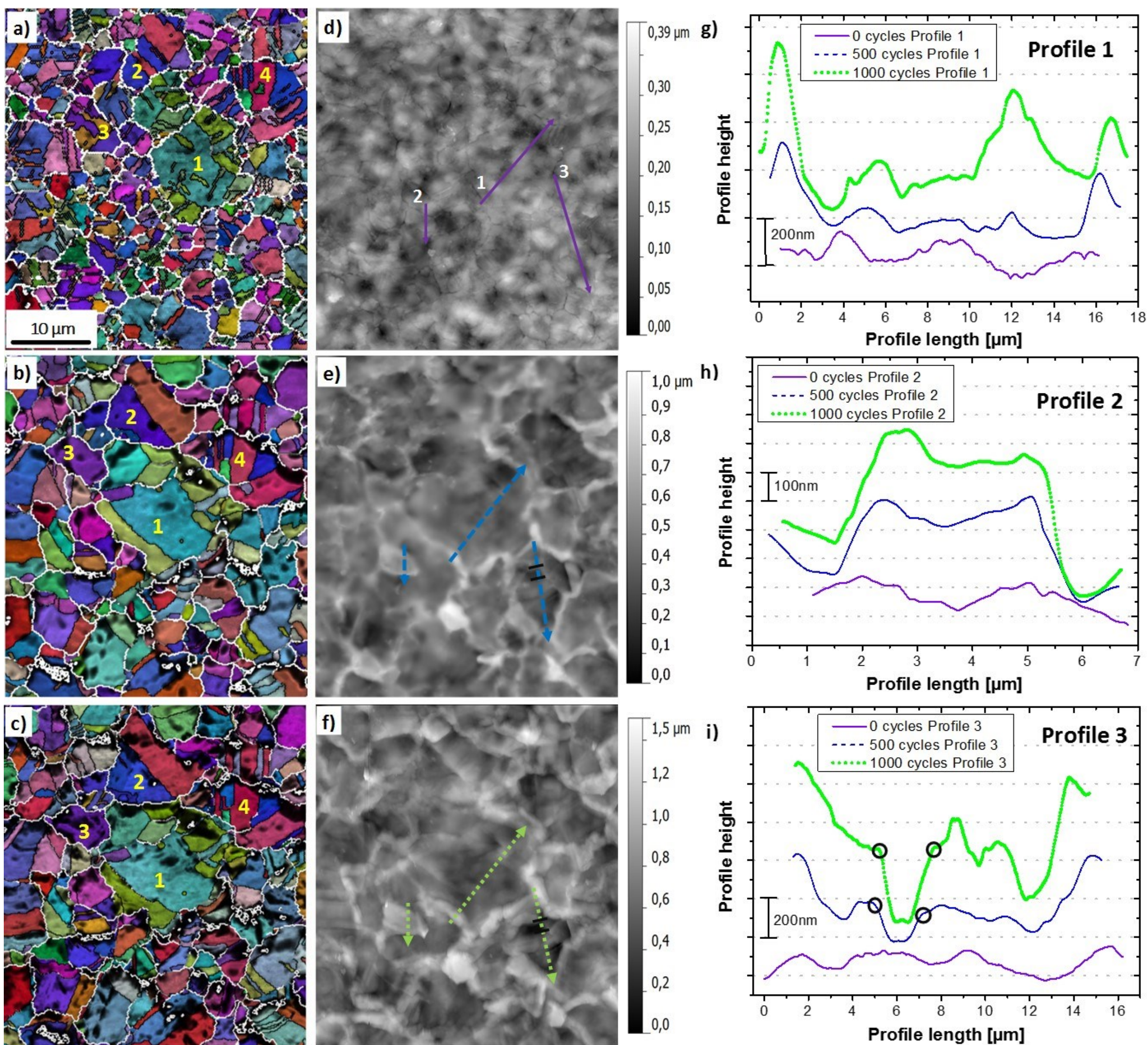

Figure 7: Early site specific microstructural evolution of Film B. Crystallographic evolution (a-c) is matched by the topographical evolution (d-f) of the same surface area for 0, 500 and 1000 cycles. Three selected microstructural features are examined regarding their topographical evolution, indicated by Profile 1-3 (g-i).

Therefore, the severe roughening occurs at twin boundary interfaces and high angle grain boundaries which form deep valleys upon cycling. In general, it can be stated that the film surface evolution for Film B leads to a rougher topography after 1000 cycles, which was already seen by the global RMS roughness evolution in Figure 4. It can be seen that the roughening in Film B is distinctively different from Film A, where the height evolution occurred at very confined regions such as high angle grain boundaries (see Figure 5d-i). In Film B, the roughening is not restricted to certain areas. Furthermore, grain growth can be quantitatively observed with AFM, indicating that HAGB are mobile and not hindered by certain mechanisms as seen in Film A. To classify the microstructural changes in Film B, four distinct features are indicated in the EBSD images (Figure 7a-c). In the first 500 cycles the majority of grains exhibited a significant reduction of the twin boundary length via twin boundary migration. This can be observed in Feature 1, 3 and 4. The approximately (212) oriented twinned grain (Feature 1) forms a stable parent/twin structure after losing a significant portion of twin boundary length in the first 500 cycles. A similar development is seen for Feature 4 where internal twins and smalI twin lamellae diminish, forming a stable twin/parent configuration (Figure 7b). In case of Feature 3, the multiple twinned grain, the first 500 loading cycles lead to a twin-free (112) oriented grain. To accommodate the externally applied thermo-mechanical load grains not only plastically deform via twin boundary migration, but also with normal grain growth via HAGB migration. This can be seen for Feature 1, where Profile 1 reveals the grain growth in the first 1000 cycles (Figure 7g). For Feature 2 the significant grain growth is along with the formation of two parallel twin lamellae by the expense of smaller grains (Figure 7b). Further thermal loading up to 1000 cycles (Figure 7c) indicates that the above mentioned microstructural changes are still occurring although in a less pronounced manner. Additionally, it can be seen that, once a stable microstructural configuration is formed (e.g. parent/twin substructure) processes such as faceting between certain boundaries as well as within coherent crystal regions can be observed. Such an example is indicated in Feature 2, where severe faceting between the (111)/(115)-oriented parent/twin region can be observed as well as a distinct uprise of the (115)-oriented twin region at the very top (Figure 7e-f). Moreover, the microstructure in Film B exhibits a pronounced surface

roughening within the grains, indicated by the black spots, due to the overlaid IQ (Figure 7c).

In the progressed cycling stage microstructural phenomena, such as twin boundary migration or normal grain growth, do not change very much, making a direct examination of the local changes essential. Figure 8 represents the microstructural changes for Film A on a local scale in the advanced state. A (30x30) μm^2 sample surface section is matched after 1500 cycles (Figure 8a, c) and 3500 cycles (Figure 8b, d) with respect to the crystallographic (EBSD) and topographical (AFM) changes. For further information two profile sections are used to indicate topographical changes of certain features (Figure 8e, f), and FIB-prepared trenches reveal the cross-section after 3500 cycles (Figure 8g, h).

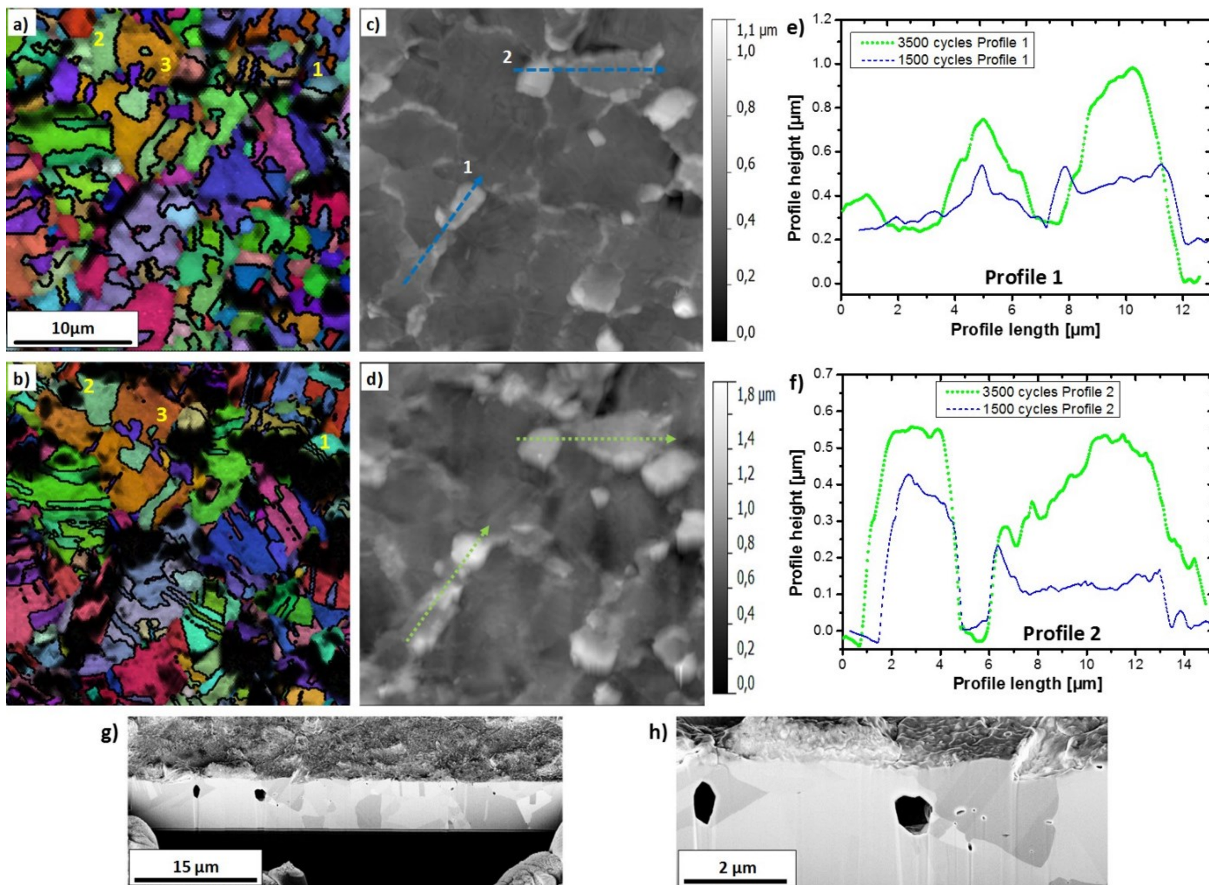

Figure 8: Film A, site specific microstructural and topographical comparison between 1500 (a, c) and 3500 cycles (b, d) of a 30x30 µm surface section. Two profiles indicate topographical changes (e, f) and film cross sections reveal microstructural changes after 3500 cycles (g, h). For 1500 cycles an EBSD scan resolution of 0.3 µm was used, after for 3500 cycles the scan was performed with a resolution of 0.2 µm.

It should be pointed out that for the ease of indication, in both cycle stages only twin boundaries were indicated with black lines in the EBSD image. From a topographical point of view, it can be stated that the surface morphology of Film A appears in a defined manner after 1500 cycles. Certain, especially smaller, grains are growing with respect to the out of plane direction, whereas within grains no significant roughness evolution due to plastic deformation can be seen with a pronounced the uprise next to grain boundaries occurs. Regarding the topographical evolution, Profile 1 highlights the roughening of an approximately (111)/(115) oriented, twinned grain. The two superimposed profile sections, set to a reference point, indicate that the small grain is shrinking in size and at the same time the height in the out of plane direction increased by more than a factor of two after 3500 cycles. From the two AFM images (Figure 8c, d) it can be seen that the shape has changed from an elongated grain to a circular shaped grain. Profile 2 represents the further uprise of two small, twinned grains. It can be seen that both grains are also growing in the lateral directions. The shape of the two hillock-like grains suggest that surface diffusional mass transport is still somewhat restricted, since significant gradients develop with respect to the lateral height variation of the surface topography. Regarding the microstructural development, the internal twin boundary length is growing although significant changes in the size of certain domains cannot be seen. In certain microstructural features, indicated by Features 1, 2 and 3 (Figure 8b), advanced damage within the grains can be revealed. Gradual changes of crystal orientation can be seen (Feature 3) leading to an equilibrium configuration of the dislocation network, forming small angle grain boundaries in the red twin lamellae (Features 1, 2). Further details for such small angle grain boundaries will be shown in Figure 9. The cross-section (Figure 8g, h) reveals that after 3500 thermo-mechanical loading cycles voids have formed. In Figure 8h it can be seen that pores reach a size up to the micrometer region and new, small pores also form in the material. These pores lie directly next to an out of plane grown grain, which could indicate that copper atoms were transported to this particular grain, leaving voids.

The progressed cycling state of Film B is presented in Figure 9. The microstructural evolution is characterized between 1500 (Figure 9a, c) and 3500 cycles (Figure 9b, d) using EBSD and AFM sections with a size of 30x30 μm^2. Comparing Figure 9a and 9b

no significant changes regarding the twin boundary length is observed, in agreement with Figure 4b, suggesting that the grains have reached an equilibrium state. Some features remained unchanged, displaying a stable configuration (see Feature 2).

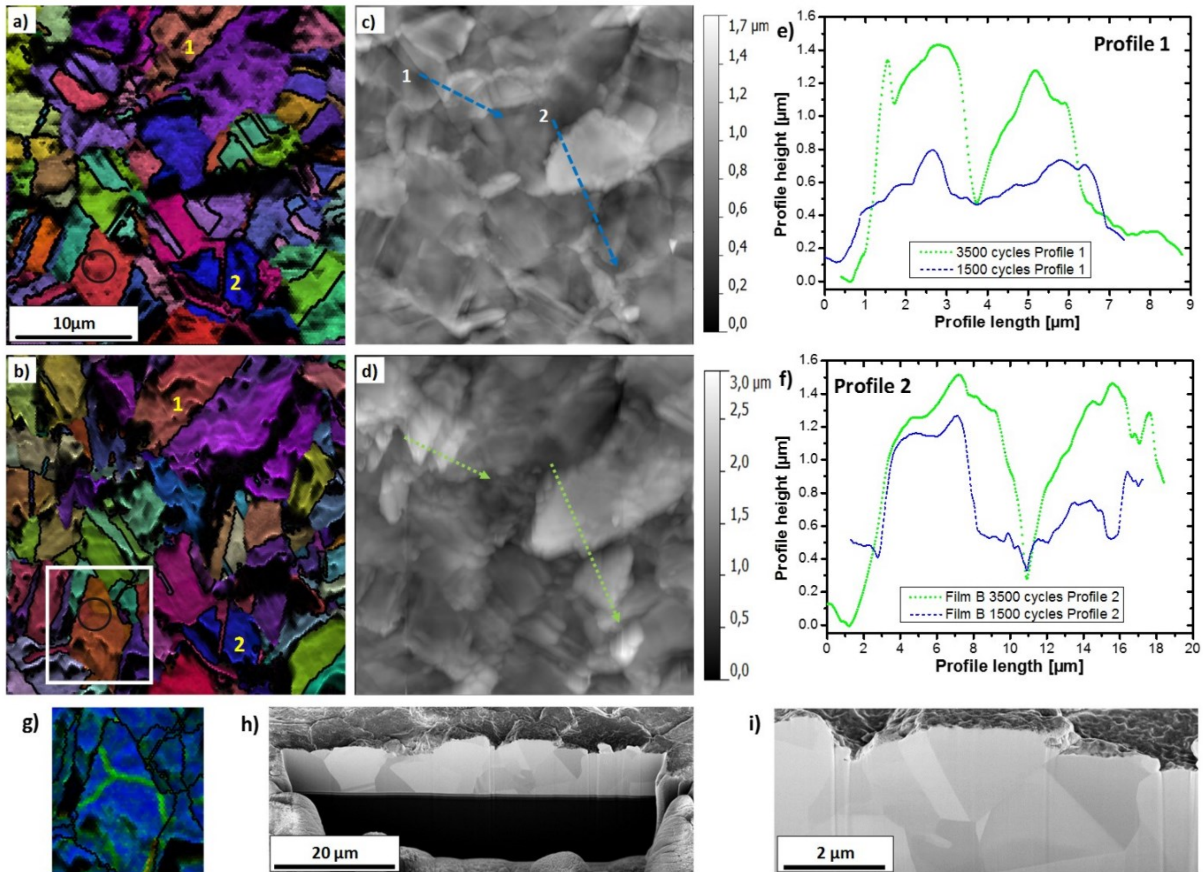

Figure 9: Film B site specific microstructural and topographical comparison between 1500 (a, c) and 3500 cycles (b, d) of a 30x30µm surface section. A magnified section (g) shows a formed small angle triple junction in a (100) oriented grain. Two profiles indicate topographical changes (e, f) and film cross sections reveal microstructural changes after 3500 cycles (h, i). Due to the on-going surface roughening process, only twin boundaries are indicated.

In Feature 1, the (113)-oriented twin, the crystal orientation gradually changes after 3500 cycles (Figure 9b), whereas for 1500 cycles (Figure 9a) a constant orientation is observed. A better illustration for such a substructure, evolving in coherent crystal segments (e.g. twins), can be identified in the circular marked (100)-oriented twin segment. After 1500 cycles, the twin segment reveals a colour gradient, indicating that the orientation of the crystal segment is gradually changing. After 3500 cycles a triple junction of three small angle grain boundaries is formed. For a better illustration, Figure 9g shows the triple junction using a magnified kernel average misorientation image. Thereby, a local misorientation value of the kernel is assigned with respect to the center

of the kernel, indicating the small angle grain boundaries as sharp green lines correspond to a mean misorientation angle of about four degrees. The dislocations, driven by the applied in-plane stress field, align in an equilibrium configuration forming such 120° segments. This special triple junction angle can be experimentally identified since half of a hexagon has formed, indicating that a polygonisation process is happening. Regarding the film thickness changes of Film B, Figures 9h and 9i show a film cross section after 3500 cycles. No pores are visible, even in the magnified image (Figure 9i). Rather, good interfacial integrity between boundaries can be observed. The overview image also reveals that the twins in Film B have been significantly reduced, resulting in a more columnar grain structure with less intersecting grains through the film thickness. The cross section also confirms the significant surface roughening, which reveals a change in film thickness with respect to the lateral dimensions.

Regarding the topographical changes in the later cycling stage, Profile 1 and 2 indicate the on-going surface roughening process. In both examples, significant changes due to mass transport on the free surface lead to changes in topography, giving rise to the assumption that in Film B atoms could more easily diffuse to other places.

5 Discussion

The presented results in the previous section show that the thermo-mechanical fatigue behaviour for Film A and Film B differ significantly. While they are nominally similar with respect to the initial microstructure, they reveal a very different thermo-mechanical fatigue behaviour. Summarizing the presented results, three main differences in the fatigue evolution between Film A and B are noted:

(1) the roughness evolution,

(2) the microstructural evolution, related to twin boundary migration, grain growth and texture development, and

(3) the higher driving force for void formation.

Figure 10 schematically highlights the microstructural differences between Film A and B, which develop during the thermo-mechanical loading process and will be discussed in the following paragraphs. It can be seen that Film A develops a constrained surface

roughness (1) which progresses at highly localized HAGB. In the case of Film B such observations were not found, since the roughness evolution was over the entire film surface. Regarding the microstructural evolution, Film A exhibited a very restricted behaviour, where no significant grain growth (2a) or twin boundary migration (2b) were observed. On the contrary, Film B exhibited significant grain growth with continuous reduction of twin boundaries achieved by twin boundary migration. With respect to the void formation potential (3), voids in the micrometer range formed in Film A and no voids were found in Film B regardless of the local microstructural conditions.

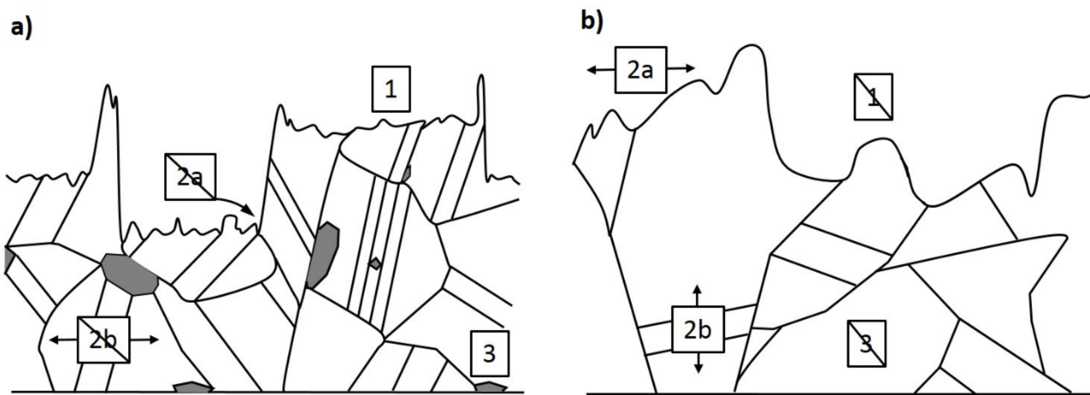

Figure 10: Schematic microstructural evolution of Film A (a) and Film B (b). Differences can be addressed in the constrained surface roughness evolution for Film A (1), present grain growth (2a) and twin boundary migration (2b) in Film B and the formation of voids (3) in Film A.

Before discussing these aspects in more detail, first the literature status regarding impurity effects in Cu films will be summarized. Previous time-of-flight secondary ion mass spectroscopy (ToF-SIMS) profiles revealed that the most important distinction between the two copper films is that Film A has a significantly higher sulphur and chlorine residual concentration than Film B [7]. Although ToF-SIMS measurements were used in this previous study to determine the impurity levels, quantification is not possible as the sputter yield of different atoms varies and only a relative comparison of the signal intensities is possible after normalizing the values to the copper signal. This relative comparison indicates that Film A has a significantly higher impurity concentration. Quantitative analysis, using XRF measurements revealed that the Cl and S contamination (Film A) is in the ppm range. Hence, it can be stated that both film system contain S and Cl as the main inorganic components, although Film A has a significantly higher concentration and Film B can be seen as a relatively pure copper

film. This allows for the discussion on the observed differences in the fatigue evolution of the two copper films with respect to the influence of inorganic impurities.

The initial microstructure already indicates the fundamental difference between Film A and B, where Film A has a 26% higher fractional twin boundary length per unit area than Film B, which is qualitatively indicated by EBSD surface and cross section microstructures (Figure 2). The fact that Film A has a higher twin density is most likely due to the fact that for the deposition process a different additive package was used compared to Film B. The main question is what role the significantly higher remaining S and Cl quantities play regarding twin nucleation/stability and subsequent twin densities. Studies propose that incorporated impurities enhance the formation of twins and leading to higher twin densities [31]. It was suggested that modifying elements (Sr, Na), with similar impurity levels (60ppm), are adsorbed on the solid-liquid interface of the growing crystal, promoting twin formation due to errors in the stacking sequence. This can be seen as impurity induced twinning, where interstitial atoms lower the stacking fault energy of the crystal. For electrochemical copper deposition similar results were obtained, where the increasing additive concentration resulted in a smaller grain size [32]. For electrodeposited copper, it was also observed that the implantation of gallium ions (using FIB) near the surface, right after electrochemical copper deposition, prevented recrystallization processes. This phenomenon can be directly related to the implanted impurity atoms, since copper layer underneath was not affected, hence completely recrystallizing [6].

This preventing effect is also indicated in the film stress evolution (Figure 3), where Film A showed no changes after 80 thermal cycles, whereas Film B exhibited significant changes. This can be observed in the significant change of the thermo-elastic slope in Film B, going from -2.09MPa/°C to -2.51MPa/°C after 80 thermal cycles and approaching the elastic behaviour of Film A. The lower elastic slope in the first cycles of the pure copper Film B might occur due to micro-plasticity and the film displays a thermo-elastic behaviour on the global scale. At the same time, some local regions in the microstructure plastically deform under the applied stress and temperature. This is in agreement with the significant increase of the grain size and diminishing twin boundary length in the first 100 cycles, revealed by the global microstructural data

(Figure 4). Furthermore, Film A exhibited a higher strength and greater elastic regime, indicating a potential benefit regarding the mechanical properties due to impurities pinning boundaries.

The surface morphology changes (1) show that Film A displays a very pronounced film surface structure. Both, HAGB and twin boundaries exhibit strong grooving (Figure 5a, d) while the inner surface of the grains remain perfectly flat. In Film B, HAGB can also be identified by grooves at the interface (Figure 7a, d), but the strong grooving at twin boundary interfaces was not observed. This observation is intriguing since the grooves are normally attributed to the local energy equilibrium of HAGB [33]. The morphology (depth, contact angle, etc.) of the developed grain boundary groove provide qualitative information on how much the free energy, G, is lowered by the minimization of the grain boundary energy, γ_g along with the rise of the surface energy, γ_s [34]. A strong decrease of interfacial energy is often related to the presence of impurities, because such interstitial atoms bond to the matrix element and lower the energy at the free surface [35, 36]. In the case of Film A, the microstructural investigations indicated that the sulphur and chlorine species are not only found at HAGB [7], but also segregate to twin boundaries significantly modifying their morphology. The subsequent thermo-mechanical loading resulted in a constrained surface roughness evolution for Film A. It appears that segregated impurities modify diffusional processes at the surface, leading to the localized roughening at boundaries. The purer Cu-film, Film B exhibited a consistent roughness evolution over the entire cycling experiment, indicating that diffusional processes at the surface are not hindered.

The differences of Film A and B with respect to the microstructural evolution (2) further emphasize the influence of impurities on the thermal fatigue behaviour of Cu films. The pure copper film, Film B, reveals significant grain growth which is going along with the constant diminishing of fractional twin boundary length. In comparison, in Film A such grain growth with coupled twin boundary migration was not observed, although many grains had the same parent/twin configuration as in Film B, as well as higher evolving stresses (see Figure 3). The global data regarding grain size and twin boundaries directly shows that in Film A deformation mechanisms have to act differently in order to accommodate the applied thermo-mechanical loads achieved by the thermal cycling.

Furthermore, the (100)-texture development for Film B clearly shows the increasing occurrence of the (100) crystal orientation, indicating the preferable growth of such grains or twin segments. This in agreement with basic literature studies where the strong elastic anisotropy in copper provides the driving force with regards to the strain energy minimization. The (100) orientation is energetically preferred if films of a certain thickness (greater ~1µm) are subjected to relatively large strains [30, 37, 38]. On the contrary, the impurity containing copper system, Film A, had hardly any (100)-texture intensity change during the thermo-mechanical fatigue experiment (Figure 4c), which shows that such an energy minimization process is prevented. The thermo-mechanical fatigue evolution reveals that in the pure Cu film, Film B, the externally applied thermo-mechanical energy is used to minimize the internally stored energy by microstructural mechanisms, such as grain growth, twin boundary migration/annihilation and texture changes, coupled with severe surface roughening. The impurity enriched Film A does not show such mechanisms.

The imposed thermo-mechanical energy and resulting plastic deformation induced new small angle boundaries within formerly coherent regions (twin lamellae) in the progressed stage of fatigue. The evolution of such microstructural features, predominately found in soft (100) oriented twin segments, shows that the dislocations are initially distributed laterally throughout the crystal segment creating a constant misorientation gradient (Figure 9a). The acting in-plane stresses caused by further cycling drive the dislocations into an equilibrium structure (hexagonal arrangement of LAGB). This polygonisation is well known in material science since it displays the minimum energy for grains and balances the surfaces tension [39]. Surprisingly the same structure is achieved by the arrangement of dislocations, minimizing their energy with regard to other dislocations, which originates from the elastic stress field of dislocations [40]. Hence, formation of new grain structures, achieved by thermal cycling, revealing a further microstructural fatigue mechanism.

Regarding the void formation potential (3), the film cross-sections for Film A (Figure 8g, h) revealed that after 3500 cycles voids were found. Furthermore, it appears that the voids seem to be situated underneath distinct upraised grains indicating that atoms come from the inside of the Cu film. Such fatigue features are well known from thermally

treated copper- tin solder joints in the microelectronics industry due to the Kirkendall effect [41]. In the case of electroplated copper films previous studies suggest that stress induced void formation occurs due to the misorientation angle between neighbouring grains [42], or due to high stress concentration between twin boundary interfaces and the increased copper diffusivity along grain boundaries [43]. If these conclusions, both based on the concept of stress migration, are used concerning the purer Cu sample type, Film B, one can see that this is not applicable. Voids did not form at HAGB interfaces (Figure 9h), nor did voids nucleate at the section of dense twin boundary network (Figure 9i) in the film. The direct comparison of the two Cu films with respect to void formation suggests that the higher S and Cl residual concentration in Film A lowers the free energy for void nucleation, thus promoting the formation of voids inside the copper film. This has also been discussed in other works, specifically dealing with the relationship between void formation in Cu metallizations and the impurity content [44, 45]. Such voids develop when the free energy barrier for void formation:

$$\Delta G = \frac{4\gamma_i^3 f_v}{\sigma^2} \qquad (2)$$

is low enough. In equation (2), γ_i is the interfacial energy, f_v is a geometrical factor of the void and σ is the local applied stress [46]. A reduced γ_i caused by impurities would significantly promote the void nucleation since γ_i scales to the power of three. The obtained results are also in agreement with other experimental and theoretical observations [47]. The presence of S impurities in Cu leads to a high concentration of excess vacancies in the material, due to the high affinity of the formation of a S-vacancy complex and the segregation of S at grain boundaries along with the energetically favourable formation of Cu_2S. This indicates that for stress induced voiding, impurities significantly alter the void formation potential, as well as revealing that pure copper films are very resistant to voiding.

6 Conclusions and Summary

In this work, the thermo-mechanical fatigue behaviour of two different electrodeposited copper film systems was examined. The microstructural evolution was quantitatively and qualitatively analysed via a site-specific tracking technique enabling the investigation of global parameters, as well as certain localized microstructural features.

The fatigue behaviour of Cu films was analysed with respect to the influence of inorganic impurities (mostly Cl, S), which are inevitably incorporated by the electrodeposition process of copper metallizations.

In direct comparison, the fatigue behaviour of a Cu-film with inorganic impurities (Cl, S) in the ppm region with similar initial microstructural parameters showed an altered fatigue behaviour. The microstructure of Film A exhibited insignificant grain growth with stable twins. A constrained roughness evolution was observed, indicating that diffusional processes at the film surface occurred in a restricted manner. Moreover, the impurity enriched Cu-film, Film A showed void formation within the film material. The higher film strength and the greater microstructural stability in Film A show that deliberate doping would result also in improvement of certain mechanical properties.

The significantly purer Cu-film, Film B, exhibited pronounced twin boundary migration as a main deformation mechanism along with grain growth. This occurred with continuous roughening of the film surface as well as an increase of the (100) texture throughout the thermo-mechanical loading process. The results revealed that the material response for Film B after the application of a cyclic thermo-mechanical load is linked to energy minimising processes. Furthermore, the experimental results showed that in the progressed state, where dislocations in coherent crystals form new small angle grain boundaries in a hexagonal arrangement.

7 Acknowledgement

The work was performed in the project EPPL (Enhanced Power Pilot Line), financially supported by grants from Austria, Germany, The Netherlands, France, Italy, Portugal, and the ENIAC Joint Undertaking (ENIAC JU Grant Agreement no. 325608). This project is co-funded within the programme “Forschung, Innovation und Technologie für Informationstechnologie” by the Austrian Ministry for Transport, Innovation and Technology.

8 References

[1] J.C. Anderson, Applications of thin films in microelectronics, Thin Solid Films, 12 (1972) 1-15.

[2] W.D. Nix, Mechanical properties of thin films, Metallurgical transactions A, 20 (1989) 2217-2245.

[3] M. Nelhiebel, R. Illing, C. Schreiber, S. Wöhlert, S. Lanzerstorfer, M. Ladurner, C. Kadow, S. Decker, D. Dibra, H. Unterwalcher, M. Rogalli, W. Robl, T. Herzig, M. Poschgan, M. Inselsbacher, M. Glavanovics, S. Fraissé, A reliable technology concept for active power cycling to extreme temperatures, Microelectronics Reliability, 51 (2011) 1927-1932.

[4] W. Robl, M. Melzl, B. Weidgans, R. Hofmann, M. Stecher, Last metal copper metallization for power devices, Semiconductor Manufacturing, IEEE Transactions on, 21 (2008) 358-362.

[5] R. Vinci, E. Zielinski, J. Bravman, Thermal strain and stress in copper thin films, Thin Solid Films, 262 (1995) 142-153.

[6] M. Stangl, Charakterisierung und Optimierung elektrochemisch abgeschiedener Kupferdünnschichtmetallisierungen für Leitbahnen höchstintegrierter Schaltkreise, DOI (2007).

[7] A. Wimmer, M. Smolka, W. Heinz, T. Detzel, W. Robl, C. Motz, V. Eyert, E. Wimmer, F. Jahnel, R. Treichler, G. Dehm, Temperature dependent transition of intragranular plastic to intergranular brittle failure in electrodeposited Cu micro-tensile samples, Materials Science and Engineering: A, 618 (2014) 398-405.

[8] A. Wimmer, W. Heinz, T. Detzel, W. Robl, M. Nellessen, C. Kirchlechner, G. Dehm, Cyclic bending experiments on free-standing Cu micron lines observed by electron backscatter diffraction, Acta Materialia, 83 (2015) 460-469.

[9] P.A. Flinn, Measurement and interpretation of stress in copper films as a function of thermal history, Journal of Materials Research, 6 (1991) 1498-1501.

[10] M.D. Thouless, J. Gupta, J.M.E. Harper, Stress development and relaxation in copper films during thermal cycling, Journal of Materials Research, 8 (1993) 1845-1852.

[11] G.P. Zhang, R. Moenig, Y.B. Park, C.A. Volkert, Thermal Fatigue Failure Analysis of Copper Interconnects under Alternating Currents, Electronic Packaging Technology, 2005 6th International Conference on, 2005, pp. 1-4.

[12] M. Aicheler, S. Sgobba, G. Arnau-Izquierdo, M. Taborelli, S. Calatroni, H. Neupert, W. Wuensch, Evolution of surface topography in dependence on the grain orientation during surface thermal fatigue of polycrystalline copper, International Journal of Fatigue, 33 (2011) 396-402.

[13] R. Mönig, R. Keller, C. Volkert, Thermal fatigue testing of thin metal films, Review of Scientific Instruments, 75 (2004) 4997-5004.

[14] O. Kraft, P. Wellner, M. Hommel, R. Schwaiger, E. Arzt, Fatigue behavior of polycrystalline thin copper films, Zeitschrift für Metallkunde, 93 (2002) 392-400.

[15] R. Schwaiger, G. Dehm, O. Kraft, Cyclic deformation of polycrystalline Cu films, Philosophical Magazine, 83 (2003) 693-710.

[16] R. Keller, J. Phelps, D. Read, Tensile and fracture behavior of free-standing copper films, Materials Science and Engineering: A, 214 (1996) 42-52.

[17] O. Kraft, R. Schwaiger, P. Wellner, Fatigue in thin films: lifetime and damage formation, Materials Science and Engineering: A, 319 (2001) 919-923.

[18] A. Wimmer, A. Leitner, T. Detzel, W. Robl, W. Heinz, R. Pippan, G. Dehm, Damage evolution during cyclic tension–tension loading of micron-sized Cu lines, Acta Materialia, 67 (2014) 297-307.

[19] M. Hommel, O. Kraft, Deformation behavior of thin copper films on deformable substrates, Acta Materialia, 49 (2001) 3935-3947.

[20] P.A. Flinn, D.S. Gardner, W.D. Nix, Measurement and interpretation of stress in aluminum-based metallization as a function of thermal history, IEEE Transactions on Electron Devices, 34 (1987) 689-699.

[21] D.P. Field, B.W. True, T.M. Lillo, J.E. Flinn, Observation of twin boundary migration in copper during deformation, Materials Science and Engineering: A, 372 (2004) 173-179.

[22] S. Bigl, S. Wurster, M.J. Cordill, D. Kiener, Site Specific Microstructural Evolution of Thermo-mechanically Fatigued Copper Films, BHM Berg-und Hüttenmännische Monatshefte, 160 (2015) 235-239.

[23] T.A. Hahn, Thermal Expansion of Copper from 20 to 800 K—Standard Reference Material 736, Journal of applied physics, 41 (1970) 5096-5101.

[24] C. Swenson, Recommended values for the thermal expansivity of silicon from 0 to 1000 K, Journal of physical and chemical reference data, 12 (1983) 179-182.

[25] S. Bigl, W. Heinz, M. Kahn, H. Schoenherr, M.J. Cordill, High-Temperature Characterization of Silicon Dioxide Films with Wafer Curvature, JOM, DOI 10.1007/s11837-015-1600-8(2015) 1-6.

[26] D. Nečas, P. Klapetek, Gwyddion: an open-source software for SPM data analysis, centr.eur.j.phys., 10 (2012) 181-188.

[27] K. Chavez, D. Hess, A novel method of etching copper oxide using acetic acid, Journal of The Electrochemical Society, 148 (2001) G640-G643.

[28] H. Ledbetter, E. Naimon, Elastic properties of metals and alloys. II. Copper, Journal of physical and chemical reference data, 3 (1974) 897-935.

[29] D.S. Gardner, P.A. Flinn, Mechanical stress as a function of temperature in aluminum films, Electron Devices, IEEE Transactions on, 35 (1988) 2160-2169.

[30] C.V. Thompson, R. Carel, Texture development in polycrystalline thin films, Materials Science and Engineering: B, 32 (1995) 211-219.

[31] S.-Z. Lu, A. Hellawell, The mechanism of silicon modification in aluminum-silicon alloys: Impurity induced twinning, Metallurgical transactions A, 18 (1987) 1721-1733.

[32] M. Stangl, M. Lipták, A. Fletcher, J. Acker, J. Thomas, H. Wendrock, S. Oswald, K. Wetzig, Influence of initial microstructure and impurities on Cu room-temperature recrystallization (self-annealing), Microelectronic Engineering, 85 (2008) 534-541.

[33] C.V. Thompson, Grain growth in thin films, Annual Review of Materials Science, 20 (1990) 245-268.

[34] W.W. Mullins, The effect of thermal grooving on grain boundary motion, Acta Metallurgica, 6 (1958) 414-427.

[35] J.W. Martin, R.D. Doherty, B. Cantor, Stability of microstructure in metallic systems, Cambridge University Press1997.

[36] A. Mersmann, Crystallization technology handbook, CRC Press 2001.

[37] R. Carel, C. Thompson, H. Frost, Computer simulation of strain energy effects vs surface and interface energy effects on grain growth in thin films, Acta Materialia, 44 (1996) 2479-2494.

[38] C.V. Thompson, R. Carel, Stress and grain growth in thin films, Journal of the Mechanics and Physics of Solids, 44 (1996) 657-673.

[39] A. Bhargava, C. Sharma, Mechanical Behaviour and Testing of Materials, PHI Learning Pvt. Ltd.2011.

[40] D. Hull, D.J. Bacon, Introduction to dislocations, Pergamon Press Oxford, 1984.

[41] E. Kirkendall, C. Upthegrove, L. Thomassen, Rates of diffusion of copper and zinc in alpha brass, New York, 1938.

[42] J. Nucci, R. Keller, D. Field, Y. Shacham-Diamand, Grain boundary misorientation angles and stress-induced voiding in oxide passivated copper interconnects, Applied physics letters, 70 (1997) 1242-1244.

[43] A. Sekiguchi, J. Koike, S. Kamiya, M. Saka, K. Maruyama, Void formation by thermal stress concentration at twin interfaces in Cu thin films, Applied physics letters, 79 (2001) 1264-1266.

[44] M. Stangl, J. Acker, S. Oswald, M. Uhlemann, T. Gemming, S. Baunack, K. Wetzig, Incorporation of sulfur, chlorine, and carbon into electroplated Cu thin films, Microelectronic Engineering, 84 (2007) 54-59.

[45] M. Stangl, M. Lipták, J. Acker, V. Hoffmann, S. Baunack, K. Wetzig, Influence of incorporated non-metallic impurities on electromigration in copper damascene interconnect lines, Thin Solid Films, 517 (2009) 2687-2690.

[46] J. Yu, J. Kim, Effects of residual S on Kirkendall void formation at Cu/Sn–3.5 Ag solder joints, Acta Materialia, 56 (2008) 5514-5523.

[47] P.A. Korzhavyi, I.A. Abrikosov, B. Johansson, Theoretical investigation of sulfur solubility in pure copper and dilute copper-based alloys, Acta Materialia, 47 (1999) 1417-1424.

VI Publication C

Correlative microstructure and topography informed nanoindentation of copper films

Stephan Bigl, Thomas Schöberl, Stefan Wurster, Megan J. Cordill, Daniel Kiener

Surface and Coatings Technology (2016) Vol. 308; 404–413

Abstract:

The effect of residual inorganic elements on the local plastic deformation behaviour of two different copper films was investigated. It was found that a film containing inorganic elements in the ppm range, has a distinctively higher hardness at twin boundaries and high angle grain boundaries compared to the grain interior. An almost pure copper film shows no distinct difference regarding the plastic deformation compared to the same microstructural features. The results suggest that such residual elements form hard boundaries, leading to higher hardness on a local microstructural level. Moreover, the influence of the local topography was demonstrated. The use of atomic force microscopy before and after indentation illustrated that significant errors in the determination of hardness occurs when the local surface topography matches the dimensions of the indenter tip. This was further confirmed by the quantitative comparison of the elastic properties of the loading and unloading segments of the corresponding load-depth curves using Hertzian contact mechanics and the Oliver-Pharr method. It will be demonstrated that the measured hardness values can be directly correlated to local microstructural and topography features.

1 Introduction

In modern material science great interest lies in the improvement of the mechanical properties of materials by modifying the initial microstructure. Especially in the microelectronics industry the need for customized metallization layers is of great interest, satisfying the requests for high strength or microstructural stability at elevated temperatures. Copper metallizations and interconnects represent one of the key material components used in microelectronic devices. Lower cross-sectional areas, high current densities, withstanding large thermal stresses, and the on-going reduction of the volume to surface ratio are only a few challenges of copper metallization layers [1-4]. Therefore, a deep understanding of the influence of the microstructure on the thermo-mechanical fatigue behaviour is needed to improve future copper metallizations with respect to product requirements and reliability during operational lifetime.

Strengthening mechanisms, such as the Hall-Petch effect, show that the grain size plays a key role in the enhancement of mechanical properties of bulk materials [5, 6]. Such effects can be also obtained for metallic thin films. Thereby, electrodeposited copper (Cu) showed a tensile strength about ten times higher than that of conventional (bulk) Cu while retraining bulk electrical conductivity was comparable to that of pure Cu [7]. The high strength is explained by the sub-micron grain size and the dense network of coherent twin boundaries serving as an effective blockade to dislocations. At the same time such coherent twin boundaries have an extremely low resistivity compared to other interfaces such as high angle grain boundaries (HAGB) ($\theta \geq 15°$). It should be clear that mechanical properties are specifically altered via grain boundary engineering through grain refinement or the generation of a high fraction of twin boundaries. Both the grain size and presence of twins can be easily modified in copper thin films since grain size is strongly influenced by the deposition parameters and the low stacking fault energy (SFE) promotes twin formation [8]. Furthermore, impurities incorporated through the deposition process can strongly alter interfacial energies and the subsequent material behaviour such as fatigue and electromigration [9]. It becomes clear that for such microstructures, grain boundaries become the dominant component which determines the initial mechanical properties and fatigue behaviour. Hence, the research of specific grain boundaries with respect to mechanical forces on the micro-scale is necessary to

predict the overall microstructural behaviour and basic information with regards to plastic deformation.

Nanoindentation is widely used to determine mechanical properties, such as elastic modulus and hardness, of bulk and thin film materials [10]. Previous works used this method to examine changes of mechanical properties with respect to local variation of chemical composition and microstructure [11-14]. For such localized investigations very low penetration depths in the nm range are used, which are sometimes below the measured surface roughness, raising the question of the validity of the indentation results [15]. Even though several papers [16-27] have examined the influence of surface roughness on the determination of mechanical properties, none of those studies experimentally show the local contact problem in a qualitative and quantitative manner as will be demonstrated in this work.

In a recent study the thermo-mechanical fatigue behaviour of two different copper films with respect to their impurity content originating from electrodeposition were investigated[28]. The almost impurity free Cu film showed pronounced grain growth, twin boundary migration, severe surface roughening and energy minimizing texture changes. The impurity containing Cu film revealed marginal grain growth coupled with insignificant twin boundary movement, a constrained roughness evolution and almost no texture change. This indicates that even a small amount of impurity elements strongly alters the microstructural evolution with respect to HAGB or twin boundaries. Therefore, the quantification of the mechanical response of specific grain boundaries with respect to impurity levels is needed. In this work, results are presented on the comparison of the global and local deformation behaviour of two different film systems as well as specific grain boundaries with respect to the impurity content using nanoindentation. Furthermore, the challenge of the determination of mechanical properties on a microstructural level is shown by the effect of the local contact situation (surface roughness and grain boundary grooves). Using indent-specific AFM imaging before and after indentation enables the verification of the influence of the local topography. These observations are then combined with the corresponding load-displacement curves and the grain boundary character determined from EBSD images to evaluate the role of impurities in copper films.

2 Experimental

For all experimental investigations two different 5 µm thick copper films were used. Both film system were prepared by electrochemical deposition and sputtering, which is the current state of the art process for wafer metallization [29]. Prior to electrodeposition, a thin tungsten-based adhesion layer was sputtered on a 725 µm thick silicon wafer of (100) orientation, followed by sputtering of a 300 nm Cu film seed layer. After seed layer deposition, electrochemical deposition was utilized to create the final 5 µm thick film. This enables an artefact-free substrate influence investigation of hardness and elastic modulus for low penetration depths (maximum depth: 3% of film thickness) as experimentally shown by Saha and Nix [30].To experimentally simulate the common problem of incorporated inorganic species (e.g. Sulphur (S), Carbon (C) and Chlorine (Cl)) the deposition process was designed to result in different impurity levels by the variation of the additive contents. Film A resulted in a high remaining inorganic impurity content (≤ 100 at% ppm), while Film B is an almost impurity-free pure copper film [31]. After electrochemical film deposition, both films were subjected to a 30 min heat treatment at 400 °C in inert atmosphere (forming gas) to guarantee a room temperature stable polycrystalline microstructure. Furthermore, the annealing step reduces microstructural defects generated during the film growth which imparts a microstructure with a low dislocation density, suitable for studying pop-in events at low strain rates [32].

Nanoindentation experiments were performed using a Hysitron Triboscope (Hysitron, Minneapolis, USA) in load control mode, an add-on instrument mounted on the scanner unit of a Dimension D3100 (Bruker Inc., Billerica, USA) atomic force microscope (AFM), which was used for AFM image acquisition. Data acquisition and analysis were done using the Triboscope 4.1.0 software package. All indents were performed using a blunt Berkovich tip (R~ 900 nm) where hardness and reduced modulus were calculated using the method of Oliver and Pharr [33]. The area function (dependence of the indenter contact area on the contact depth) was determined prior indentation using fused silica as the calibration material (E = 72 GPa). For the nanoindentation experiments linear loading was applied to the prescribed maximum load, held for 15 sec, and unloaded within 2 sec, minimizing the influence of thermal drift on specimens sized 8x8mm cut

from the wafers. For global indentation experiments 25 indenter were made using a loading rate of 1000 µN/s and a maximum load of 12 mN. The local microstructural investigations were carried out using 16 indents with a loading rate of 250 µN/s and a maximum load of 1 mN. Prior to performing the nanoindentation experiments, the specimens were cleaned with acetic acid at 35°C for about 2 min to selectively etch the potentially formed copper oxide [34], and were mounted on a magnetic iron platelet using a resin. In order to use the right machine compliance with respect to the mechanical testing, five bare silicon substrates (8x8mm) were mounted the same way as mentioned above. Thereby, machine compliance was varied until determination of the elastic unloading curve resulted in the reduced modulus of silicon. The determined machine compliance, which was used for the entire experimental data sets, was 1.5 nm/mN.

Roughness determination and surface topography imaging was performed with the above mentioned AFM using tapping mode. For the roughness determination 512x512 pixels scans of 50x50 µm^2 were acquired, while imaging of the indents (before and after) was made with areas of 30x30 µm^2. Post processing was performed using the Gwyddion 2.36 software [35]. In order to identify the microstructural boundaries and orientations of each indent, electron backscatter diffraction (EBSD) was performed with a step size of 30 nm. The EBSD system consists of an EDAX Digiview Camera attached to a LEO 1525 (Zeiss Inc., Oberkochen, Germany) scanning electron microscope. The TSL Analysis software was used for EBSD image processing. For the presented inverse pole figure (IPF) images, overlaid with the image quality (IQ), a confidence index clean-up with a threshold value of 0.07 was performed.

3 Results

The distinct differences observed in the crystallographic and surface scans of the same area between Film A and B are highlighted in Figure 1. For improved illustration HAGB (white lines), primary twin boundaries (∑3, black lines), and secondary twin boundaries (∑9, grey lines) are highlighted in the IPF-IQ images. The IPF standard colour triangle, used for every EBSD image, is displayed in Figure 3d. It can be seen that both films exhibit a similar microstructure with no texture differences, except for the fact that Film A (Figure 1a) has a slightly higher fraction of twins than Film B (Figure 1c). This is

supported by evaluation of a larger scan area (150x150µm) where Film A has a grain size of 2.8 ± 0.9 µm and Film B 3.2 ± 1.1 µm, including ∑3 boundaries.

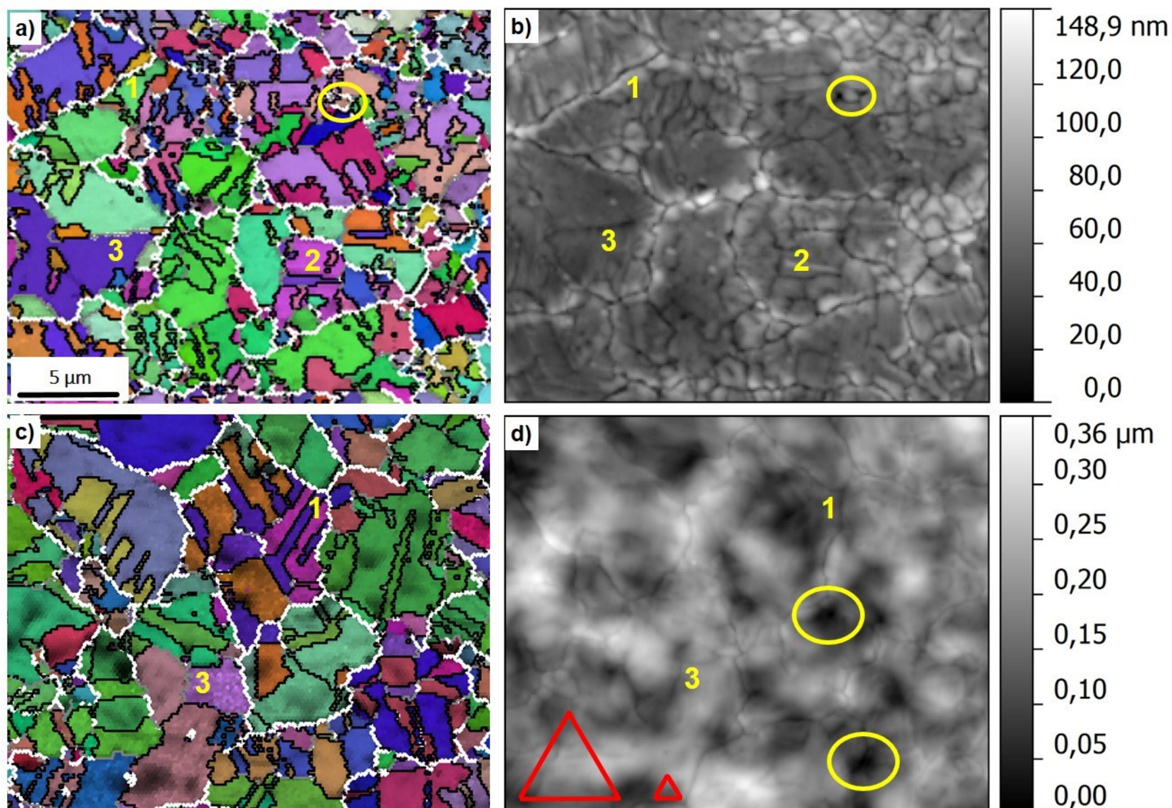

Figure 1: Initial microstructure of Film A (a) and B (c) illustrated by IPF-IQ images, matching the same area of surface topography for Film A (b) and B (d). Interfaces such as HAGB (1), primary twins (2) and secondary twins (3) are highlighted. Furthermore, topographical features are highlighted using circles and the approximate residual contact areas are shown for Film B (d). Scale bar in (a) valid for all sub images.

The determined elastic moduli using EBSD scan data (Film A: 110 ± 31 GPa; Film B: 112 ± 30 GPa) indicate that in both samples a very similar, texture-less polycrystalline copper material was deposited. As a comparison an artificial copper-EBSD file simulating a random texture resulted in an average elastic modulus of about 109 GPa. In the EBSD and AFM images in Figure 1, the three most common boundary types are highlighted. Boundary 1 displays a random HAGB. In both samples, this particular interface results in a defined grooved boundary between neighbouring grains, displayed by the AFM images (Figure 1b, d). Boundary 2, highlighting a primary twin (∑3) generates a defined groove-like substructure similar to the HAGB in Film A. For Film B (Figure 1c, d) a similar correlation was not observed. Rather, primary twins (black lines) do not show any distinct morphological feature in the AFM image. Boundary 3

illustrates a secondary twin (∑9) which exhibits grooving in both films. Further investigation will not include the particular deformation behaviour of secondary twins due to the fact that secondary twins are an uncommon feature in both films (Figure 1a, c). Regarding the surface roughness, Film A has a root mean square (RMS) surface roughness of ~17 nm and Film B reaches a value of ~60 nm. Film A has a very smooth inner grain surface where height differences only appear in the form of grooves at HAGB and twin boundaries (circular feature, Figure 1b). On the contrary, Film B has a very wavy and rough surface with strong local variation of surface curvatures and craters (indicated by circles). These distinct differences in the surface morphologies become even more important when looking at the two triangular shapes in Figure 1d which illustrate the approximate remaining indent contact areas of the performed indentation experiments. One can anticipate that the local topography can cause problems in the determination of site specific properties such as indenting into the craters.

Furthermore, it should be indicated that for indentation experiments performed with a high load of 12 mN (Figure 2a), the plastically influenced area is significantly larger compared to the indentation experiments performed with a maximum load of 1 mN. This means that indentation measurements performed with the high load will measure the global deformation behaviour because it involves a representative microstructural area and the low load indents for the local grain boundary behaviour. Figure 2b shows the hardness for the global indentation experiments. The 25 indents for each sample resulted in an average hardness of 1.08 ± 0.04 GPa for Film A and 0.89 ± 0.11GPa for Film B. Compared to Film B, Film A has a 21% higher hardness, a distinct difference in the mechanical properties. In addition, it can be seen that for the experimental variance Film A has an almost three times smaller standard deviation (indicated by error bars) than Film B. The experimental variance becomes evident when the corresponding load-displacement curves are compared. All load-displacement curves (Figure 2a) lie within a small range for the smooth Film A, but Film B has a greater scatter.

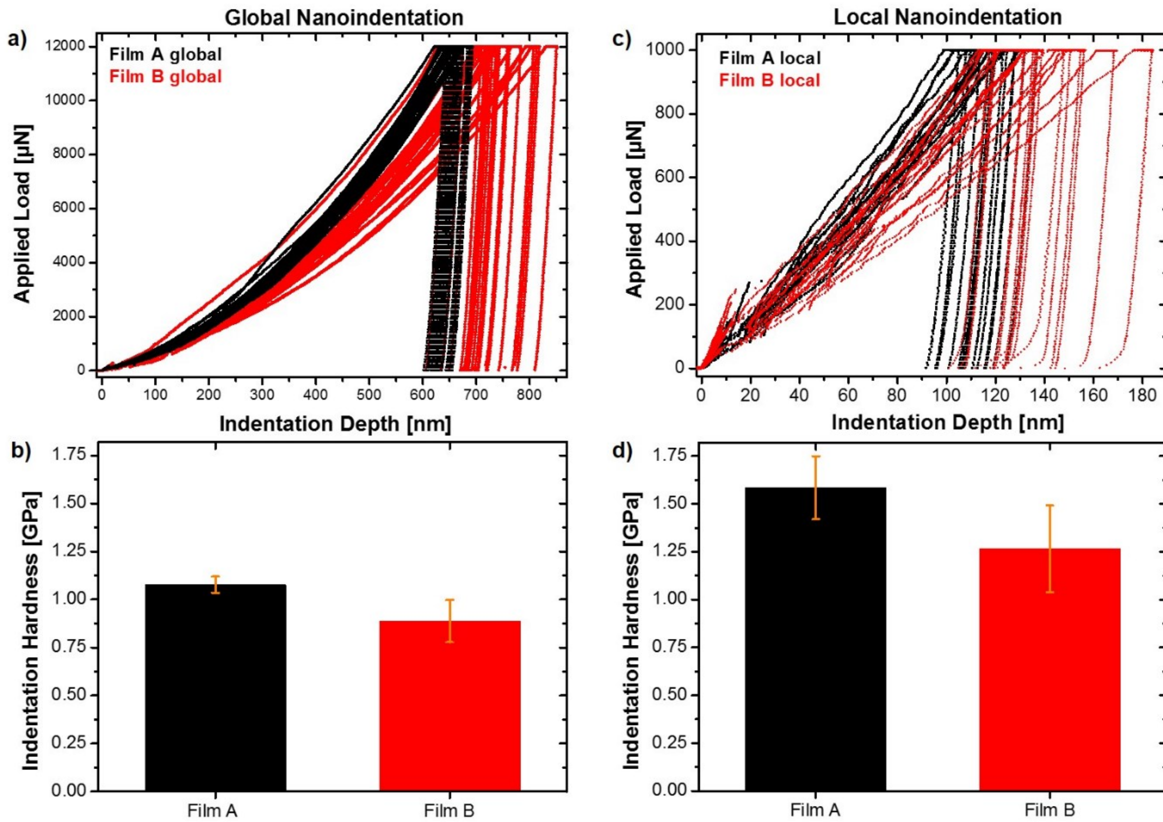

Figure 2: Global hardness results of Film A and B (b) with corresponding load-displacement curves (a) are shown on the left-hand side. On the right-hand side local hardness results of Film A and B (d) and corresponding load-displacement curves (c) are illustrated.

Besides the scattering, the load-displacement curves confirm a systematic difference in hardness because the two data sets are distinctively separated with respect to the final indentation depth. To understand the difference in the plastic deformation behaviour and to cancel out any effect of grain size (effect of Taylor hardening as a dependence of grain size), indentation experiments were performed at the local microstructural level. Figure 2d displays the hardness for the 1 mN indentation experiments using a maximum load of 1 mN. Film A resulted in an average hardness of 1.58 ± 0.16 GPa and 1.26 ± 0.23 GPa for Film B. Similar to the high load indentation results, Film A reveals a 25% higher hardness compared to Film B. The reason that local hardness results are significantly higher than the global hardness is due to the well-known indentation size effect [36, 37]. At the same time the standard deviation of the hardness of Film A increased by a factor of four which can be attributed to the localized situation of each particular indent. In the case of Film B only an increase of a factor of two for the standard deviation was observed. When looking at the corresponding load-displacement curves

(Figure 2c) one can see that on the local scale there is an overall difference between the indents in Film A and B, although the general trend remains the same.

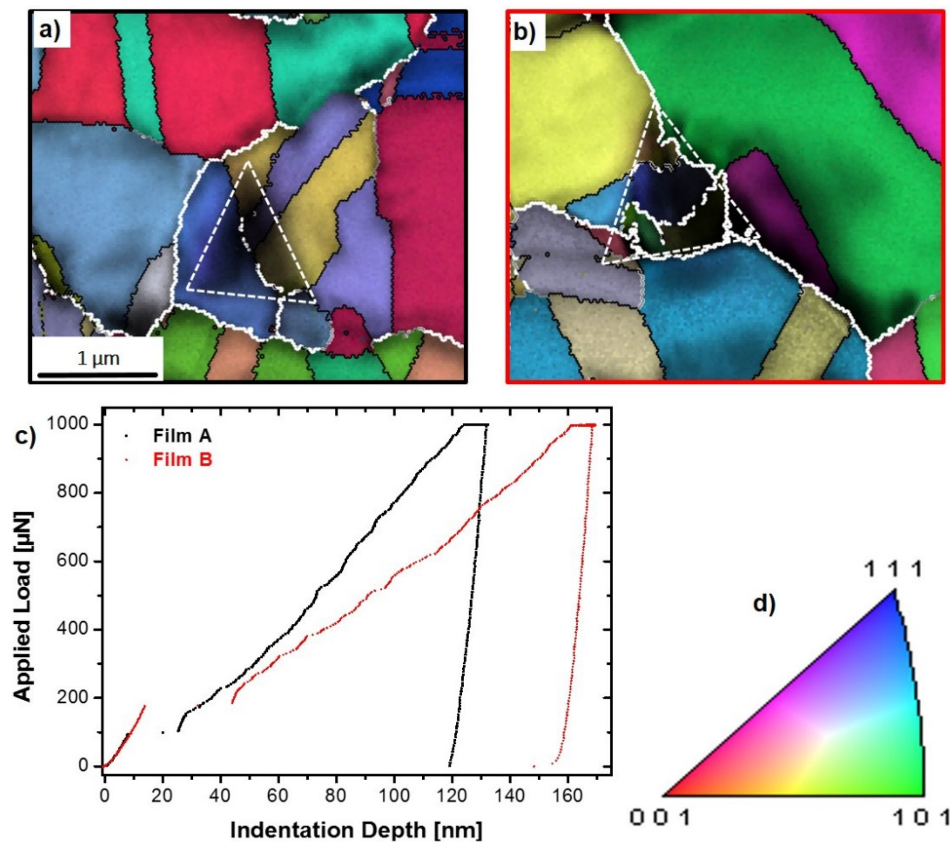

Figure 3: High resolution EBSD images (IPF-IQ) of Film A (a) and Film B (b) after local indentation at HAGB. The corresponding load-displacement curves illustrate the difference in plastic deformation. IPF colour code (d) is applicable for all EBSD images.

Two exemplary indents are shown in Figure 3 with high resolution EBSD scans taken of each indent illustrating the crystallographic situation of Film A (Figure 3a) and Film B (Figure 3b) after indenting at a HAGB. The hardness for the indent in Film A was 1.37 GPa, the indent in Film B resulted in a hardness value of 0.94 GPa. This presumes that in Film A the plastic deformation behaviour distinctively deviates from that found in Film B. The load-displacement curves (Figure 3c) confirm this with the initial elastic loading followed by a rapid excursion in depth at constant load (pop-in), indicating the onset of plastic deformation. Since further loading follows a geometrically necessary load-displacement curve, which is dependent on the particular flow stress of the material [32], the example in Figure 3 indicates that Film A and B reveal different local plastic

deformation behaviour. After the pop-in event, Film B shows a significantly flatter loading curve than Film A, resulting in the lower hardness value.

To make any appropriate conclusions regarding the differences in the local deformation behaviour further information is needed since it is not clear where the strengthening in Film A compared to Film B originates. EBSD images alone cannot provide detailed information about the exact position of the indent (see Figure 3a,b). Experimental errors due to the local surface topography (grain boundary grooves and roughness) cannot be evaluated with the crystallographic information. Therefore, another set of indents (16 indents of each film material) was performed to determine the local deformation behaviour with respect to boundaries and topography, where additional AFM images were acquired before and after the indentation experiments. Such topography imaging before and after indentation also allows for the explanation of the large scatter observed in the load-displacement curves of Film B illustrated in Figure 2.

Insights into such experimental errors and the demand for the critical analysis of the load-displacement curves using AFM-supported topography information are shown in Figure 4. Two distinct experimental errors are shown. Both can be attributed to a contact problem leading to an incorrect hardness value. In the case of the harder Film A, an experimental situation is shown in Figure 4b, d-f where the indentation at an edge of a HAGB led to a hardness value of 1.13 GPa, which distinctively differs from the mean value and its experimental variation (1.58 ± 0.16 GPa).

By taking a closer look at the load-displacement curve (Figure 4a), it can be seen that during the loading segment flatter elastic loading compared to Film B was recorded, followed by a pop-in and a very flat increase of the load up to about 70 nm can be observed (initial loading in Figures 4-7 is indicated by using equation (1), where $E^*=$ 110 GPa and $R=$ 900 nm). When looking at the two profile sections before and after indentation (Figure 4d) taken through the cross-section of the indenter tip from the two AFM images (arrows in Figure 4e, f), one can see that the indenter tip has contact with the corner of a grain.

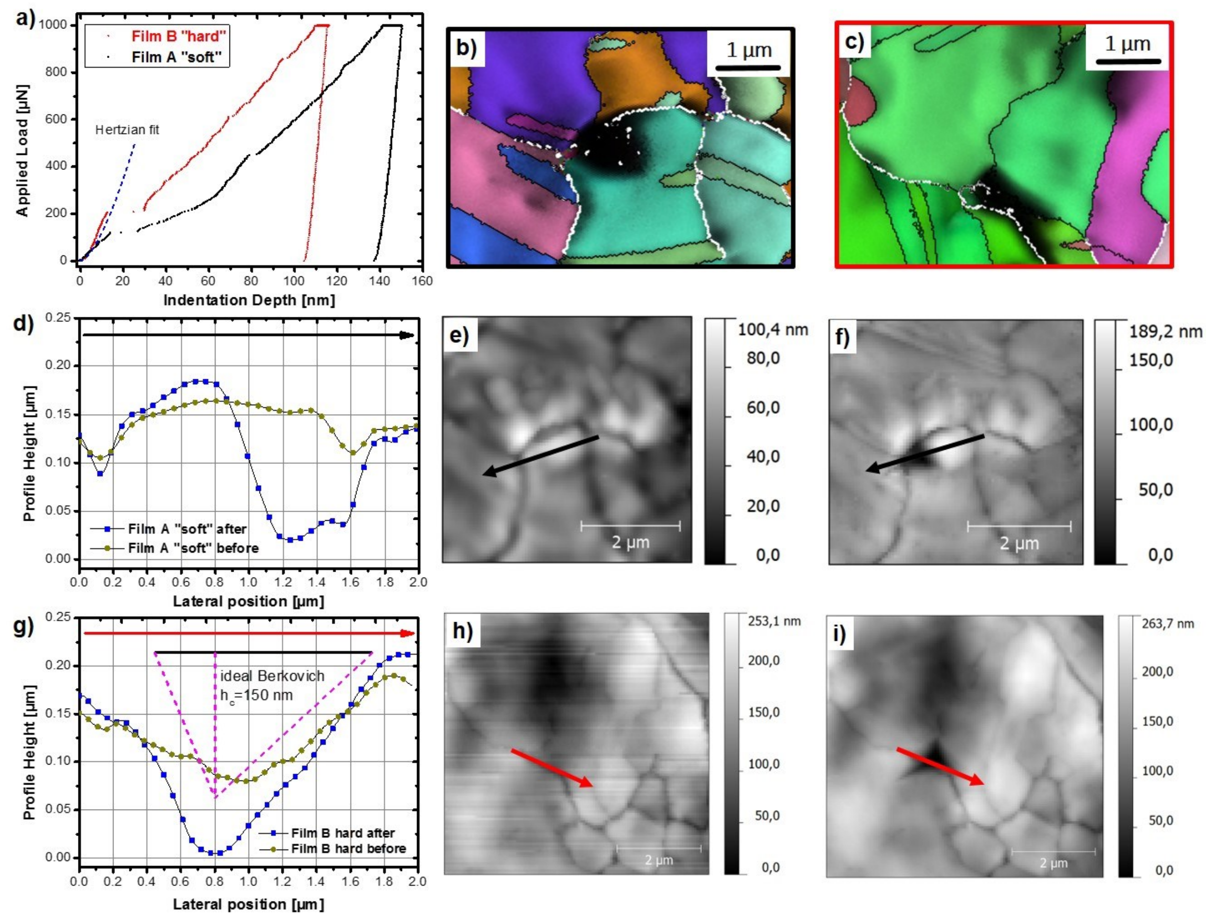

Figure 4: Load-displacement curves (a) of situations where localized contact problems between indenter tip and surface led to erroneously determined contact areas. The initial elastic loading of the indents is described with Hertzian contact mechanics (Hertzian Fit: E*= 110 GPa, R= 900 nm) . Indentation at the edge of a grain in Film A (b, d-f) leads to sideward slipping of the indenter tip (a) and a lower hardness. In Film B (c, g-i) the local topographical situation indicated by the shape of a perfect Berkovich indenter geometry, led to a very steep loading curve (g) and therefore a higher hardness value.

The residual cross-section suggests that during the initial loading (up to ~70 nm) the tip did not have full contact with the surface. The tip appears to be sliding along the surface. With further loading, the tip follows a typical elasto-plastic loading curve (parallel to second curve). The sliding phenomena becomes even more plausible when looking at Figure 4g where the profile section before indentation follows approximately the shape of an ideal Berkovich indenter (drawn to scale), which is not the case for the indent in Film A (Figure 4d).

The second experimental error illustrates the influence of the local topography, shown for an indent on the surface of Film B (Figure 4c, g-i). It can be seen that the indenter tip was placed in an area where the local asperities match the indenter geometry to a

certain extent (laterally, as well as the contact angle). The profile of an ideal Berkovich tip (h_c: 150 nm) indicates that during loading the contact area is significantly increased, resulting in a greater stiffness response and a steeper load-displacement curve (Figure 4a). This led to an apparent hardness of 1.65 GPa, significantly higher from the mean value (1.26 ± 0.23 GPa), showing that local topography can lead to a severe overestimation in hardness.

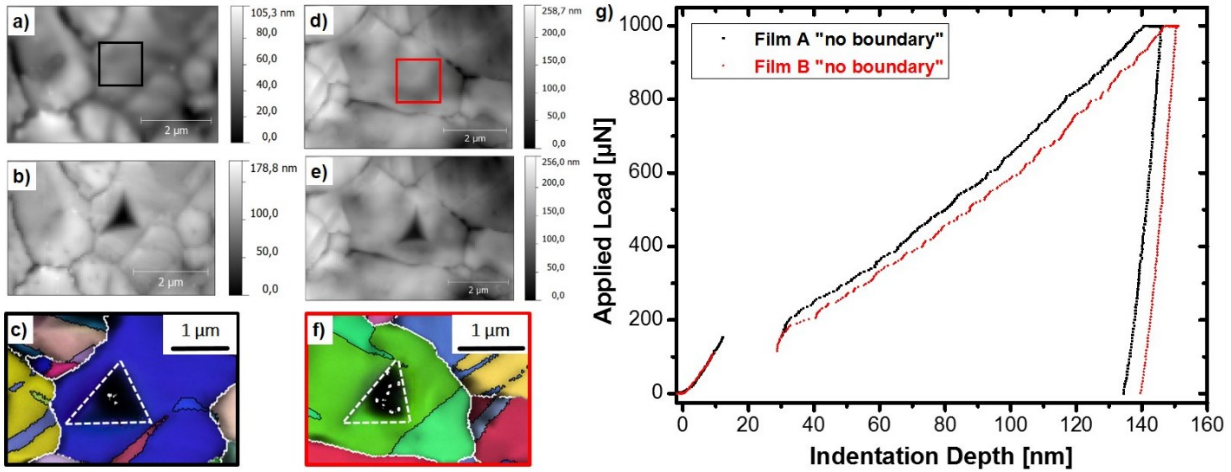

Figure 5: Local indentation experiments in a coherent regions. AFM images before and after indentation are shown in combination with the particular crystallographic situation for Film A (a-c) and Film B (d-f). The corresponding load-displacement curves (g) show that within a grain the plastic deformation behaviour does not differ much and similar initial elastic loading following Hertzian theory is observed (Hertzian Fit: E*= 110 GPa, R= 900 nm).

After elimination of such contact problems, three representative situations, with respect to grain boundaries are presented in Figure 5-7 and the experimental analysis is supported by AFM imaging. Figure 5 illustrates the case of the deformation behaviour in a grain interior (no boundary involved) of the two films. AFM images before and after indentation are shown in combination with the particular crystallographic situation for Film A (Figure 5a-c) and Film B (5d-f). The EBSD and AFM images indicate that in both films no grain boundaries are present during the indentation experiments. The fact that the out of plane crystal orientation is not the same (Film A ~ {111}, Film B ~ {110}) can be neglected for the plastic deformation behaviour in copper since the plastic strain field under the indenter tip leads to activation of multiple slip systems and an averaged hardness of these slip systems [38]. The AFM images show the identical surface areas which allow the evaluation of the indentation sites. The specific areas (marked as rectangles) prior to nanoindentation were investigated using profile sections for Film A

(Figure 5a) and Film B (Figure 5d). Indentation experiments would have been discarded if potential errors, such as topography-induced indentation artefacts (addressed in the discussion) occurred. In the presented results of the pre-indent surfaces do not show any tilted surfaces or cavities which could influence the indentation experiments. This can be also seen in the load-displacement curves (Figure 5g) of the two indents. Both indents show an initially elastic loading behaviour, followed by spontaneous pop-ins at similar load/pop-in length and further similar deformation behaviour. This led to a hardness of 1.17 GPa for Film A and 1.12 GPa for Film B, indicating that within the grain interior no differences in the mechanical response can be detected.

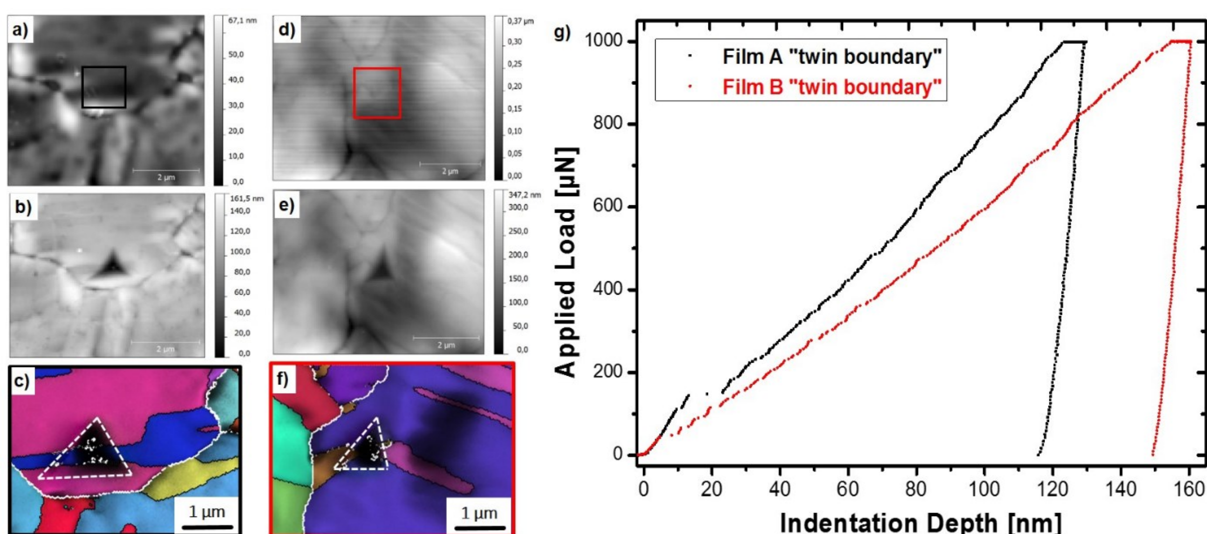

Figure 6: Local indentation experiments at twin boundary interfaces. AFM images before and after indentation are displayed in combination with the particular crystallographic situation for Film A (a-c) and Film B (d-f). The corresponding load-displacement curves (g) show a distinct difference in the plastic deformation behaviour between the two film systems, but similar initial Hertzian elastic loading (Hertzian Fit: E*= 110 GPa, R= 900 nm).

The local deformation behaviour for Film A and B begins to distinctively deviate when it comes to interactions with grain boundaries. Figure 6 shows indentation experiments which were performed directly at a ∑3 twin boundary. As one can see, Film A (Figure 6a-c) shows a different deformation behaviour to Film B (Figure 6d-f). The two films deviate in their load-displacement curves (Figure 6g) after reaching the yield stress (pop-in). Therefore, a hardness value of 1.41 GPa for Film A and 1.02 GPa for Film B was obtained, suggesting that in Film A notable resistance to plastic deformation near the twin boundary is observed, which is not the case for Film B.

An even greater difference was observed when it comes to the interaction with HAGB. Figure 7 illustrates the situation where in indents in both films were performed at the grooved HAGB. For Film A (Figure 7a-c) the pop-in occurs at a load of ~344 µN with a corresponding length of 17 nm (see Figure 7g). In comparison, Film B shows an overlapping elastic loading up to 144 µN and pop-in length of 22 nm. This qualitatively indicates that Film A withstands higher elastic shear stresses when it comes to grain boundaries and also shows a higher flow stress than Film B. Therefore, the two load-displacement curves resulted in a hardness of 1.57 GPa for Film A and 1.02 GPa for Film B.

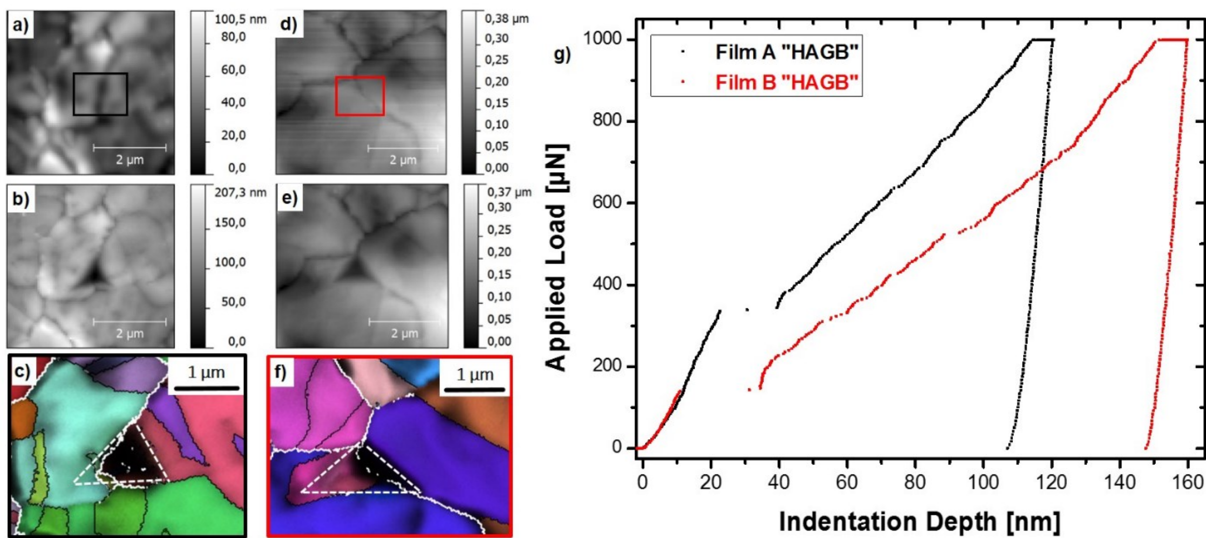

Figure 7: Local indentation experiment at a HAGB interface. AFM images before and after indentation are illustrated in combination with the particular crystallographic situation for Film A (a-c) and Film B (d-f). The corresponding load-displacement curves (g) show that indentation for Film A resulted in a high pop-in load and lower contact depth compared to Film B, along with similar initial Hertzian elastic loading (Hertzian Fit: E*= 110 GPa, R= 900 nm).

4 Discussion

With respect to the results shown in the previous section, two main topics will be discussed in more detail. First, the possible experimental errors (roughness, indenter shape) which become important when local indentation experiments are performed. Secondly, the material inherent differences in the local deformation behaviour of the two film systems with respect to boundaries and the concentration of residual inorganic elements.

Dependence of material properties on topography-induced errors

In order to substantiate the overall result that Film A has a higher hardness due to distinctively different deformation behaviour at grain boundaries, possible experimental errors will be discussed. When looking at Figure 2 the experimental scatter of the load-displacement curves becomes evident. On a global as well as local scale, the hardness is higher for Film A than for Film B, with a higher deviation from the mean. Indentation on a global scale (12 mN load) can be seen as hardness test involving a representative volume of each sample including twins, HAGB and grain interiors, while the localized indents (1 mN) lead to area-specific indents and are influenced by the local surface topography. Such topographical contact errors were illustrated in Figure 4 where AFM imaging revealed that local contact difficulties can lead to a significant error in the obtained load-displacement curve, thus, incorrect hardness values. To quantify the local influence of the topography, the elastic properties were evaluated from the examples in Figure 4. The elastic loading in both films (Figure 4a) prior to pop-ins should be well-described by Hertzian contact theory [39]. In the examples presented in Figures 5-7, elastic loading segments were almost perfectly overlapping, indicating a similar elastic response and reliable indentation data. This is not the case for the presented load-displacement curves in Figure 4 and a comparison of the reduced elastic modulus, E^*, from the loading and unloading curves support the experimental contact error. Therefore, elastic loading and unloading segments of the curves in Figure 4a are compared to the load-displacement curves of Figure 5g, which will be used as a reference since the indents were in a grain interior. The reduced elastic modulus, E^*, was determined from the initial elastic loading segment with Hertzian theory (Eqn. 1) and from the unloading curves using the Oliver-Pharr method [10]. In order to evaluate

E^*, Hertzian contact mechanics is used for the first tens of nanometres where the required load P is related to:

$$P = \frac{4}{3} E^* \sqrt{R h^3} \qquad (1)$$

and R as the radius of the indenter tip (900 nm) and h the depth of penetration [40].

In Table I, the E^* determined from the initial loading and unloading curves for Figures 4a and 5g are compared for both films. By comparing these values the determined elastic moduli from the EBSD scans of the two films mentioned in the Results section (Film A: 110 GPa, Film B: 112 GPa) and neglecting the slight changes due to the elastic influence of the indenter and the substrate material at such indentation depths [30], one can conclude the following: For the indents with the experimental errors presented in Figure 4, the E^* calculated with Hertzian theory and the Oliver-Pharr method do not correspond to one another as they should for either film system. The difference in elastic modulus implies different elastic material behaviour during loading and unreliable indentation data.

Table 1: Comparison of the reduced elastic moduli of Film A and B determined by Hertzian contact (initial loading) and the Oliver-Pharr method (unloading segment) using the corresponding load-displacement curves from Figure 4a and Figure 5g. Significant difference is found for the two experimental errors in Figure 4a, whereas the topography evaluated indents from Figure 5g exhibit very similar values.

Evaluated Segment	E* [GPa] Film A	E* [GPa] Film B
Hertz Figure 4a	80	155
Oliver Pharr Figure 4a	102	139
Hertz Figure 5g	116	128
Oliver Pharr Figure 5g	117	108

Considering that both films represent a texture-less polycrystalline copper material this directly indicates an error in the indenter contact, which translates to a miscalculation of the contact area, A_c, necessary for accurate elastic modulus and hardness measurements

using the Oliver-Pharr method. In case of the topography-evaluated indents from Figure 5, the determined reduced elastic moduli (both loading and unloading segments) are close to the elastic modulus determined with the EBSD data (Film A: 110 GPa, Film B: 112 GPa), indicating that indents were not affected by experimental contact errors.

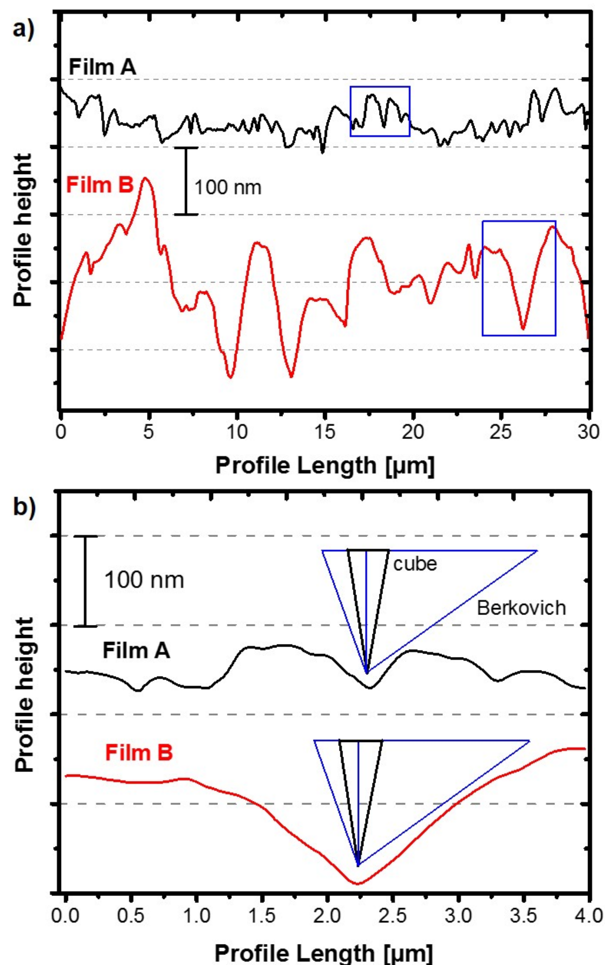

Figure 8: Surface profiles of Film A and B qualitatively indicate the difference in roughness (a). Two rough surface sections are presented in more detail with respect to the topographical influence by displaying a drawn to scale Berkovich and cube corner indenter (b).

To further substantiate such local contact problems, Figure 8a illustrates the influence of the topography with respect to the indenter geometry. In Figure 8a, a 30 µm line profile for each film is presented. The direct comparison indicates that Film B has a rougher surface topography than Film A. In Figure 8b a "rough" appearing surface section (highlighted by boxes) is shown in greater detail for both films. For both topography situations a drawn to scale ideal cross-section (h_c: 150 nm) of a Berkovich (blue lines) and cube corner (black lines) indenter are illustrated. For the examples

presented, the comparison indicates that the cube corner tip is less influenced by the local topography since its dimensions relative to the Berkovich tip are significantly smaller. This observation emphasizes that the indenter geometry can play a crucial role for certain film topographies. The surface section of Film B indicates a similar situation as already presented in Figure 4, where the depression matches the geometry of the Berkovich indenter. The particular problem does not represent the usual contact situation of a sphere [40] or a cone [41] and a half space. Therefore, an increased geometric stiffness can be expected, which would further result in a steep elasto-plastic loading curve and in unreliable hardness and E^* values.

Influence of boundaries with respect to inorganic residual elements

The reason why Film A has an overall higher hardness than Film B most likely originates from the different plastic deformation behaviour at HAGB and twin boundaries. In a previous study, chemical investigations revealed that as a result of the designed deposition processes, residual concentration of S and Cl in the ppm range are present in Film A, which is in contrast to the almost impurity-free Cu in Film B [31]. Local chemical analysis, using laterally resolved secondary ion mass spectroscopy showed that after the annealing step, both Cl and S species accumulated at grain boundaries. This is in agreement with the current literature where such elements reveals a very low equilibrium solubility in copper-based materials [42]. The authors suggested that the segregation of such non-metallic atoms to grain boundaries leads to embrittlement and a deterioration of the mechanical properties [31].

Figures 5-7 illustrate the difference in the plastic deformation behaviour with respect to the influences of grain boundaries of the two films. Within the grain interior (Figure 5), both films show a very similar deformation behaviour. This emphasizes that Film A has the same mechanical properties as Film B within coherent regions. This is also in agreement with the lateral secondary ion mass spectroscopy profiles, where most of inorganic atom species where found at grain boundaries and do not influence the grain interior. Of note is that Film A shows a distinct grooving at twin boundaries (Figure 1b), while grooving was not observed for Film B. The grooving is a very peculiar phenomena, since twin boundaries are simply stacking faults composed of either Shockley or Frank partial dislocations [43]. From a thermodynamic point of view, such

unusual grooving can be directly related to segregation of inorganic impurity atoms to the boundary. The morphology (depth, contact angle, etc.) of the grooves provide qualitative information on how much the free energy, G, is lowered by the minimization of the grain boundary energy, γ_g along with the rise of the surface energy, γ_s [44]. A strong decrease of interfacial energy is often related to the presence of impurities, because such interstitial atoms can bond to the matrix element and lower the energy at the free surface [45, 46]. For Film B the residual concentrations of Cl and S are significantly lower and grooving is not observed. Therefore, Figure 6 indicates that Film A has an about 40% higher hardness than Film B due to the incorporation of inorganic atomic species at a twin boundaries. An even more significant difference can be seen when a HAGB is involved (Figure 7). Besides the ~55% higher hardness of Film A compared to Film B, the corresponding load-displacement curves (Figure 7g) indicate that for Film A a significantly higher load is needed (~335 μN) to initiate plastic deformation than for Film B (~135 μN).

These results clearly illustrate that there is a fundamental difference in the deformation behaviour when it comes to decorated twin boundaries and HAGB. In Film A the segregated inorganic elements (Cl and S) form bonds with the copper atoms at the boundaries. Both, Cl and S have a high tendency to form strong ionic bonds with copper in various modifications [47]. For S the high diffusion coefficient in Cu, the high formation energy of Cu_2S (-0.14eV/atom) and the partly covalent nature of bonding suggest the presence of very strong grain boundaries in Film A [42].

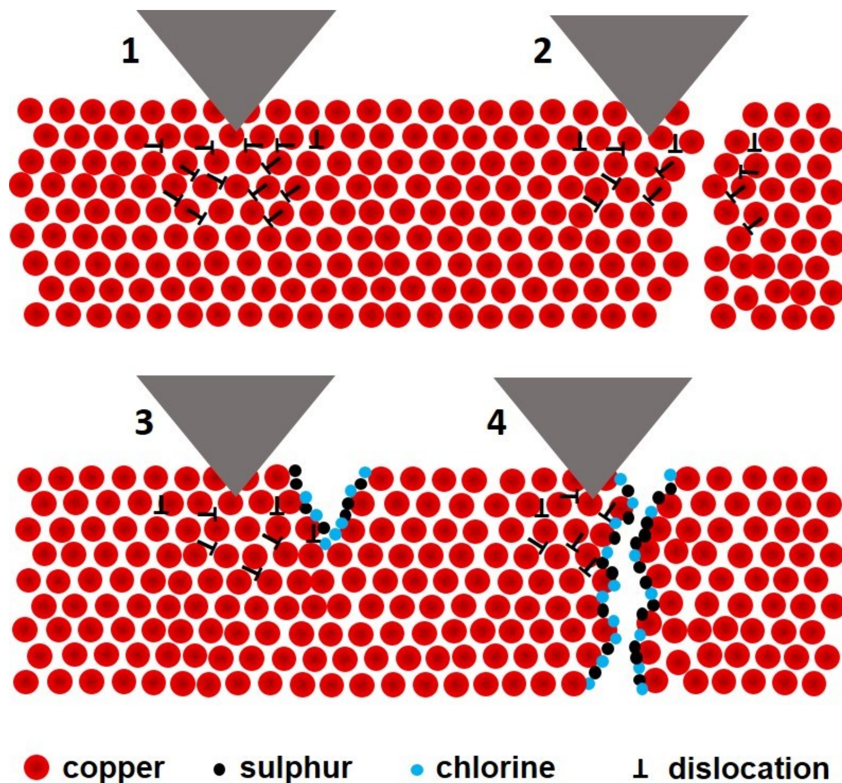

Figure 9: The influence of the presence of a strong interface involving ionic bonding of copper with Cl and S species is illustrated. Dislocation motion is not hindered when indenting in the grain interior (1) and boundaries without the presence of inorganic species (2). In comparison, dislocation shielding is possible when it comes to a twin boundary (3) and HAGB (4) with segregated Cl and S atoms. Note: atoms not drawn to scale.

Figure 9 schematically demonstrates the observed findings and provides a better visualisation of difference in the local mechanical properties in Film A and B. Under the complex strain field of an indenter tip many dislocations are generated due to the particular resolved shear stresses on the slip planes. In the grain interior (1) where no inorganic species are present, no obstacles result in a higher shear stress for dislocation generation and therefore, a similar (lower) hardness was observed for Film A and B. With respect to the local mechanical properties at HAGB in a pure copper material (2) the generated dislocations are absorbed at the grain boundary, but new dislocations can be easily nucleated in the neighbouring grain. Such behaviour was observed for Film B, where the mechanical properties with respect to boundaries did not deviate much compared to the hardness value obtained from the grain interior. In case of Film A, a distinct difference of the plastic deformation behaviour was observed when a twin boundary (3) or a HAGB was involved. In both cases the presence of a strong Cu-S/Cu-Cl ionic interface led to a higher resistance with respect to plastic deformation. This can

be attributed to the shielding effect of such formed obstacles at the boundaries. The generated dislocations are partly blocked and a comparably higher shear stress (equivalent to a higher indenter load) is needed to further promote dislocation motion.

5 Conclusions and Summary

It has been demonstrated that the local mechanical behaviour at grain boundaries is strongly affected by the presence of residual inorganic atomic species (Cl and S) on the global and local scales. At the local scale, surface topography was taken into account in order to report reliable hardness and elastic modulus values on the influence of boundaries. Nanoindentation experiments revealed that within the grain interior Films A and B showed a very similar plastic deformation behaviour, leading to about the same hardness value. A distinct difference was observed for indentation experiments performed at microstructural twin boundaries and HAGB. Film A, containing residual Cl and S in the ppm range showed a significantly higher hardness at twin boundaries and HAGB. Film B, an almost pure Cu film, showed no changes in hardness with respect to twin boundaries and HAGB. The difference can be attributed to the higher local impurities concentration at grain boundaries in Film A. Such interstitial atoms easily diffuse to the free surfaces and grain boundaries, forming strong bonds with the copper atoms. Interestingly, such high hardness was also observed at twin boundaries where the presence of impurities was indicated by the presence of distinct grooves. The almost pure Cu Film B exhibited no distinct differences between the grain interior and boundaries. Large errors in the obtained hardness can occur when the local topography matches the dimension (tip angle, contact depth) of the indenter tip or when microstructural features lead to imperfect indenter contact situations. These findings suggest that the RMS roughness value itself can be only treated as a global surface parameter where no general criteria can be established with respect to the validity of a performed indentation. Instead, the presented experimental results show that the determination of accurate mechanical properties is coupled with the local contact situation which depends geometric relationship between the indenter shape (indenter geometry, final contact depth), the surface geometry (curvature, grooves) and the local microstructure (grain boundaries).

6 Acknowledgement

The work was performed in the project EPPL, financially supported by grants from Austria, Germany, The Netherlands, France, Italy, Portugal, and the ENIAC Joint Undertaking (ENIAC JU Grant Agreement no. 325608). This project is co-funded within the programme "Forschung, Innovation und Technologie für Informationstechnologie" by the Austrian Ministry for Transport, Innovation and Technology.

7 References

[1] S.P. Murarka, R.J. Gutmann, A.E. Kaloyeros, W.A. Lanford, Advanced multilayer metallization schemes with copper as interconnection metal, Thin Solid Films, 236 (1993) 257-266.

[2] R. Vinci, E. Zielinski, J. Bravman, Thermal strain and stress in copper thin films, Thin Solid Films, 262 (1995) 142-153.

[3] M. Nelhiebel, R. Illing, C. Schreiber, S. Wöhlert, S. Lanzerstorfer, M. Ladurner, C. Kadow, S. Decker, D. Dibra, H. Unterwalcher, M. Rogalli, W. Robl, T. Herzig, M. Poschgan, M. Inselsbacher, M. Glavanovics, S. Fraissé, A reliable technology concept for active power cycling to extreme temperatures, Microelectronics Reliability, 51 (2011) 1927-1932.

[4] M. Nelhiebel, R. Illing, T. Detzel, S. Wöhlert, B. Auer, S. Lanzerstorfer, M. Rogalli, W. Robl, S. Decker, J. Fugger, M. Ladurner, Effective and reliable heat management for power devices exposed to cyclic short overload pulses, Microelectronics Reliability, 53 (2013) 1745-1749.

[5] E.O. Hall, The Deformation and Ageing of Mild Steel: III Discussion of Results, Proceedings of the Physical Society. Section B, 64 (1951) 747.

[6] N.J. Petch, The cleavage strength of polycrystals, The Journal of the Iron and Steel Institute, 174 (1953) 25-28.

[7] L. Lu, Y. Shen, X. Chen, L. Qian, K. Lu, Ultrahigh strength and high electrical conductivity in copper, Science, 304 (2004) 422-426.

[8] X.W. Zhou, H.N.G. Wadley, Twin formation during the atomic deposition of copper, Acta Materialia, 47 (1999) 1063-1078.

[9] C.K. Hu, B. Luther, F.B. Kaufman, J. Hummel, C. Uzoh, D.J. Pearson, Copper interconnection integration and reliability, Thin Solid Films, 262 (1995) 84-92.

[10] W.C. Oliver, G.M. Pharr, Measurement of hardness and elastic modulus by instrumented indentation: Advances in understanding and refinements to methodology, Journal of materials research, 19 (2004) 3-20.

[11] J.L. Cuy, A.B. Mann, K.J. Livi, M.F. Teaford, T.P. Weihs, Nanoindentation mapping of the mechanical properties of human molar tooth enamel, Archives of Oral Biology, 47 (2002) 281-291.

[12] P. Mondal, S.P. Shah, L. Marks, A reliable technique to determine the local mechanical properties at the nanoscale for cementitious materials, Cement and Concrete Research, 37 (2007) 1440-1444.

[13] S. Hengsberger, A. Kulik, P. Zysset, Nanoindentation discriminates the elastic properties of individual human bone lamellae under dry and physiological conditions, Bone, 30 (2002) 178-184.

[14] S. Pathak, D. Stojakovic, S.R. Kalidindi, Measurement of the local mechanical properties in polycrystalline samples using spherical nanoindentation and orientation imaging microscopy, Acta Materialia, 57 (2009) 3020-3028.

[15] J. Ye, M. Kano, Y. Yasuda, Evaluation of Local Mechanical Properties in Depth in MoDTC/ZDDP and ZDDP Tribochemical Reacted Films Using Nanoindentation, Tribology Letters, 13 41-47.

[16] S.W. Wai, G.M. Spinks, H.R. Brown, M. Swain, Surface roughness: Its implications and inference with regards to ultra microindentation measurements of polymer mechanical properties, Polymer testing, 23 (2004) 501-507.

[17] M.S. Bobji, S.K. Biswas, Deconvolution of hardness from data obtained from nanoindentation of rough surfaces, Journal of materials research, 14 (1999) 2259-2268.

[18] Y. Xia, M. Bigerelle, S. Bouvier, A. Iost, P.-E. Mazeran, Quantitative approach to determine the mechanical properties by nanoindentation test: Application on sandblasted materials, Tribology International, 82 (2015) 297-304.

[19] J.-Y. Kim, S.-K. Kang, J.-J. Lee, J.-i. Jang, Y.-H. Lee, D. Kwon, Influence of surface-roughness on indentation size effect, Acta Materialia, 55 (2007) 3555-3562.

[20] M. Laurent-Brocq, E. Béjanin, Y. Champion, Influence of roughness and tilt on nanoindentation measurements: A quantitative model, Scanning, 37 (2015) 350-360.

[21] Y. Xia, M. Bigerelle, J. Marteau, P.-E. Mazeran, S. Bouvier, A. Iost, Effect of surface roughness in the determination of the mechanical properties of material using nanoindentation test, Scanning, 36 (2014) 134-149.

[22] J.-Y. Kim, J.-J. Lee, Y.-H. Lee, J.-i. Jang, D. Kwon, Surface roughness effect in instrumented indentation: A simple contact depth model and its verification, Journal of materials research, 21 (2006) 2975-2978.

[23] J. Jamari, D. Schipper, Deformation due to contact between a rough surface and a smooth ball, Wear, 262 (2007) 138-145.

[24] P. Berke, F. El Houdaigui, T. Massart, Coupled friction and roughness surface effects in shallow spherical nanoindentation, Wear, 268 (2010) 223-232.

[25] C. Walter, T. Antretter, R. Daniel, C. Mitterer, Finite element simulation of the effect of surface roughness on nanoindentation of thin films with spherical indenters, Surface and coatings technology, 202 (2007) 1103-1107.

[26] M. Qasmi, P. Delobelle, Influence of the average roughness Rms on the precision of the Young's modulus and hardness determination using nanoindentation technique with a Berkovich indenter, Surface and coatings technology, 201 (2006) 1191-1199.

[27] W.-G. Jiang, J.-J. Su, X.-Q. Feng, Effect of surface roughness on nanoindentation test of thin films, Engineering Fracture Mechanics, 75 (2008) 4965-4972.

[28] S. Bigl, S. Wurster, M.J. Cordill, D. Kiener, Advanced characterisation of thermo-mechanical fatigue mechanisms of different copper film systems for wafer metallizations, Thin Solid Films, 612 (2016) 153-164.

[29] W. Robl, M. Melzl, B. Weidgans, R. Hofmann, M. Stecher, Last metal copper metallization for power devices, Semiconductor Manufacturing, IEEE Transactions on, 21 (2008) 358-362.

[30] R. Saha, W.D. Nix, Effects of the substrate on the determination of thin film mechanical properties by nanoindentation, Acta Materialia, 50 (2002) 23-38.

[31] A. Wimmer, M. Smolka, W. Heinz, T. Detzel, W. Robl, C. Motz, V. Eyert, E. Wimmer, F. Jahnel, R. Treichler, G. Dehm, Temperature dependent transition of intragranular plastic to intergranular brittle failure in electrodeposited Cu micro-tensile samples, Materials Science and Engineering: A, 618 (2014) 398-405.

[32] D.F. Bahr, D.E. Kramer, W.W. Gerberich, Non-linear deformation mechanisms during nanoindentation, Acta Materialia, 46 (1998) 3605-3617.

[33] W.C. Oliver, G.M. Pharr, An improved technique for determining hardness and elastic modulus using load and displacement sensing indentation experiments, Journal of materials research, 7 (1992) 1564-1583.

[34] K. Chavez, D. Hess, A novel method of etching copper oxide using acetic acid, Journal of The Electrochemical Society, 148 (2001) G640-G643.

[35] D. Nečas, P. Klapetek, Gwyddion: an open-source software for SPM data analysis, centr.eur.j.phys., 10 (2012) 181-188.

[36] W.D. Nix, H. Gao, Indentation size effects in crystalline materials: a law for strain gradient plasticity, Journal of the Mechanics and Physics of Solids, 46 (1998) 411-425.

[37] K. Durst, B. Backes, M. Göken, Indentation size effect in metallic materials: Correcting for the size of the plastic zone, Scripta Materialia, 52 (2005) 1093-1097.

[38] J.J. Vlassak, W. Nix, Measuring the elastic properties of anisotropic materials by means of indentation experiments, Journal of the Mechanics and Physics of Solids, 42 (1994) 1223-1245.

[39] H. Hertz, On the contact of Rigid Elastic Bodies and on Hardness, Miscellaneous Papers, Macmillan, London, 1886.

[40] K.L. Johnson, Contact mechanics, Cambridge university press1987.

[41] I.N. Sneddon, The relation between load and penetration in the axisymmetric Boussinesq problem for a punch of arbitrary profile, International journal of engineering science, 3 (1965) 47-57.

[42] P.A. Korzhavyi, I.A. Abrikosov, B. Johansson, Theoretical investigation of sulfur solubility in pure copper and dilute copper-based alloys, Acta Materialia, 47 (1999) 1417-1424.

[43] D. Hull, D.J. Bacon, Introduction to dislocations, Pergamon Press Oxford, 1984.

[44] W.W. Mullins, The effect of thermal grooving on grain boundary motion, Acta Metallurgica, 6 (1958) 414-427.

[45] J.W. Martin, R.D. Doherty, B. Cantor, Stability of microstructure in metallic systems, Cambridge University Press1997.

[46] A. Mersmann, Crystallization technology handbook, CRC Press 2001.

[47] A.E. NN Greenwood, Chemistry of Elements, Pergamon Press, Oxford, 1984.

VII Publication D

Accelerated thermo-mechanical fatigue of copper metallizations studied by pulsed laser heating

Stefan Wurster*, Stephan Bigl*, Megan J. Cordill, Daniel Kiener

Microelectronic Engineering (2017) Vol. 167; 110–118

Abstract

Fatigue is an important reliability issue for microelectronics. In this work, a technique for fast thermal cycling of thin films on substrates is introduced using an infrared laser beam. The advantages of this method are the significantly increased heating and cooling rates compared to conventional slow furnace processes, and the use of readily available small pieces of metallized wafers, which avoid complicated sample preparation. To demonstrate the applicability of the new experimental setup two copper metallization films, differing in their content of additives used for film deposition, on silicon substrates were investigated with respect to microstructural, topographical and electrical changes due to pulsed thermo-mechanical loading. The results, such as grain growth and roughness evolution are compared to results from specimens which experienced slow infrared furnace cycling. Furthermore, changes in electrical sheet resistance are shown. When analysing the outcomes from processes of different heating/cooling rates, it can be stated that accelerated laser heating leads to faster changes in these properties which enables fast screenings of metallization materials under development.

*** Both authors contributed equally to this work.**

1 Introduction

During switching operations temperatures in semiconductor devices rise substantially. As these devices are composed of a stack of different materials, having differences in elastic (Young's Modulus), plastic (e.g. yield strength) and thermal (coefficient of thermal expansion, CTE) properties, stresses evolve. Repeated switching, i.e. repeated cycles of heating and cooling, leads to changes of the film microstructure. The driving force for this phenomenon, besides diffusional processes at elevated temperatures, is the existence of stresses within the layered material. Considering a two material system, such as a thin copper layer on a thick silicon substrate, these stresses originate from differences in the CTEs leading to biaxial compressive or tensile stress states. The CTE for silicon is between ~3.45 ppm/°C for 170°C and ~3.97 ppm/°C for 400°C [1], whereas the CTE-values for polycrystalline copper are between ~17.9 ppm/°C and ~19.3 ppm/°C [2] at the same temperatures. In other words, heating of the specimen leads to compressive stresses in the faster expanding metallization layer, while tensile stress states prevail at low temperatures [3–5]. The combined effects of temperature (diffusion) and stresses might be grain growth, surface roughening and texture changes [5,6]. Texture changes can originate from rotations of the crystals or growth of preferentially oriented grains. Thus, microstructural and topographical changes are very likely to be observed due to thermal cycling. In a progressed state of thermo-mechanical cycling, voids can nucleate [5] or cracks might form, thereby degrading the mechanical and electrical properties and limiting the operational life-time. Thus, the investigation of thermo-mechanical fatigue and the integrity of metallization layers is a key issue regarding reliability of semiconductor devices.

Copper, being one of the main materials for metallizations in semiconductor technology due to its outstanding thermal and electrical properties, was chosen as the material to be subjected to thermo-mechanical cycling. To achieve thicknesses of several micrometres commonly used for metallization layers, electrochemical deposition was applied for the material used in this study. With the usage of electro-deposited materials comes the freedom of process parameters and the usage of different additives leading to differently microstructured films having the desired properties. In this publication, changes and similarities in the fatigue behaviour of two films containing different amounts of

inorganic residuals, originating from the deposition process is one of the topics that will be addressed.

For thermal cycling of materials, a variety of experimental procedures is available. Usage of the wafer curvature technique offers the possibility to directly determine the evolving stresses [4,7,8]. However, the heating and cooling rates are very low, in the regime of 0.17°C/s. Slightly accelerated heating and cooling is offered by infrared furnaces [3,5], which was used for previous works on equivalent materials [4,5]. With conventional heating techniques, it is difficult to achieve high cycle numbers (e.g. $>10^5$ cycles). When it comes to a fast screening of thermo-mechanical fatigue behaviour of new materials and stack-designs, a method that i) uses easily available cut pieces of metallized wafers that did not undergo any further processing towards the device level and ii) has a high repetition rate is desirable. These requirements are fulfilled by the laser-driven thermo-mechanical cycling technique introduced in this work.

2 Materials and Experimental Methods

Laser setup

The proposed accelerated thermal cycling method uses an infrared laser (LM250 diode laser, passively water cooled, company: Dr. Mergenthaler GmbH & Co KG, Neu-Ulm, Germany). It operates in the near infrared regime at a wavelength of 940 nm. The experimental setup relies on a laser beam hitting the silicon surface, heating the silicon and in an indirect way through heat conduction, heating the metallization layer. Silicon has a certain transmissivity at 940 nm [9], thus, adequate parts of the substrate volume and not only the surface near region is heated during a short laser pulse (~0.25 s). The copper film temperature is measured in a contact-free way via a pyrometer pointing at the metallized surface. The pyrometer points to the exact opposite site of the specimen (front side), where the laser beam hits the silicon backside. One representative thermal cycle, defined by laser output power, measured temperature and the resultant heating/cooling rate is presented in Figure 1. To avoid any effects from the running-in period of the laser process, the single cycle was taken from a later stage of the cycling process. To gain the possibility to operate in vacuum or any desired inert atmosphere, the specimen is positioned within a vacuum chamber.

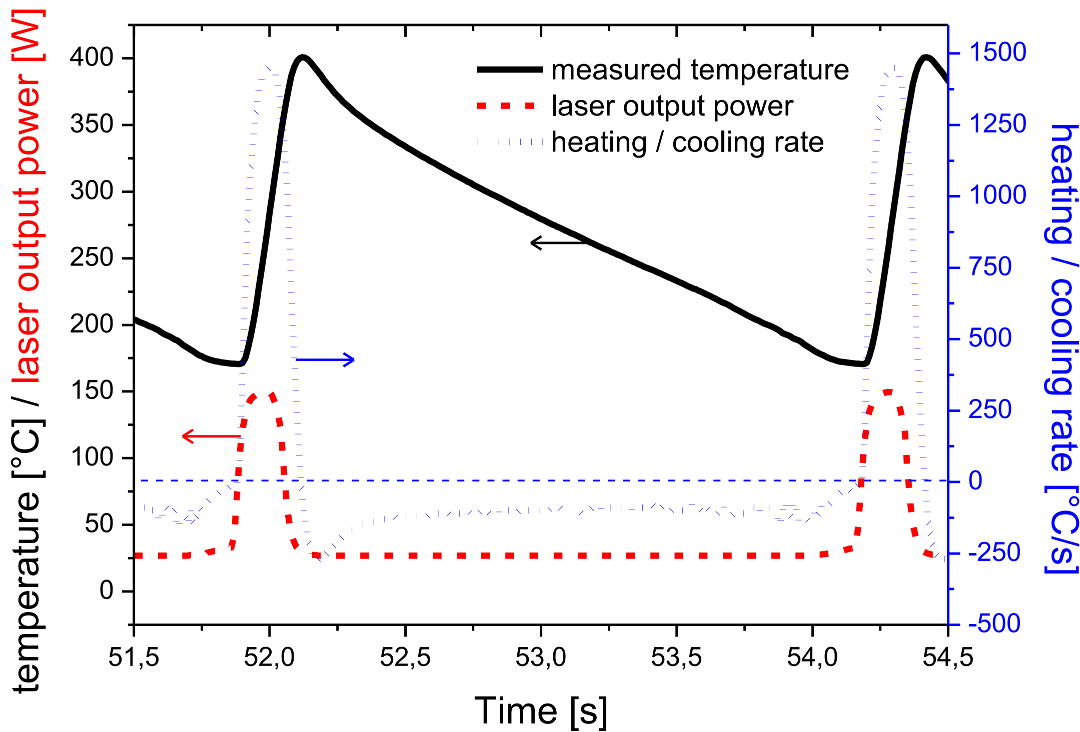

Figure 1: A representative heating/cooling cycle showing the pyrometer-measured temperature (continuous black line), the used laser power (dashed red line) as well as the achieved heating and cooling rates (dotted blue line).

The laser optics collimating the laser beam, which exits from the light conducting cable, are positioned within a safety housing for laser safety reasons. A similar safety housing is available for the pyrometer, positioned outside of the vacuum chamber. The laser beam enters into the vacuum chamber through a special vacuum-sealed window which reduces reflection and optimizes transmission of the desired wavelength. Using a silver mirror within the vacuum chamber, the laser light is deflected by ~90°. The specimen is positioned within a dedicated specimen holder without any fixation, since any fixation would interfere with the intrinsic specimen deformation and would lead to fracture of the expanding and bowing specimen during thermal cycling.

An important experimental detail is that, for programming the laser power cycles via the measured temperature, not the desired temperature of 400°C but a lower temperature has to be used. As the laser beam irradiates the backside of the specimen, the heat generated in the backside near region has to be conducted through the substrate and metallization layer to the upper metallized surface. This is the place where the temperature is measured with the calibrated pyrometer. The time needed for heat conduction leads to a delay in the measured temperature signal compared to the set

temperature as well as to the defined laser power pulse, as it is shown in Figure 1. Thus, depending on the thickness of the used specimen and its heat conductivity, the set temperature must not be set to the desired temperature, but to a lower value.

To prevent the metallization layer from oxidation, as it would be the case for copper at elevated temperatures, the vacuum chamber is first evacuated using a membrane pump to a pressure of approximately 3 mbar and then carefully vented again to a pressure of ~160 mbar using forming gas composed of N_2/H_2 with 95 vol% N_2. Furthermore, forming gas provides active cooling through convection.

The slow furnace process [5] had a maximum heating rate of 17°C/s and the maximum cooling rate was -3°C/s. With the new experimental setup, this value is considerably increased to a maximum heating rate of 1450°C/s and a maximum cooling rate of -280°C/s (blue dotted line in Figure 1). Comparing furnace and laser cycling, the heating rate and, thus, the strain rate are increased by two orders of magnitude. Hence, the time for diffusional processes is considerably smaller.

To bridge the gap between infrared furnace cycling and fast laser cycling experiments, thermal cycling was performed at a low pressure of approximately 3 mbar forming gas atmosphere. This led to cycle times of about 9 s, which is 10 times faster in comparison to infrared furnace cycles (~95 s) but three times slower compared to fast laser cycling using forming gas cooling at a pressure of 160 mbar. Despite careful experimental control, an evolution of surface oxides cannot be completely suppressed. Thus, the specimens were put into 100 vol% acetic acid for 3 min at a temperature of 35-40°C. This procedure does not affect the copper surface [10] and has already proven very useful [5,11].

Metallization Systems

For the investigation of the thermo-mechanical fatigue behaviour resulting from fast laser heating and the comparison to slow furnace heating performed in [5], 5 µm thick electrochemically deposited polycrystalline copper films on 725 µm thick silicon wafers of (100)-orientation were used. Copper is deposited on a thin layer of a tungsten-based diffusion barrier, which can be seen as a bright region between copper and silicon in the cross-sectional micrographs. After electrodeposition, annealing for half an hour was performed at 400°C in an inert atmosphere, which guarantees stable microstructures at room temperature.

Two different copper metallizations were used for this study. One film system, Film A, was designed with a high amount of additives, whereas the second customized material, Film B, was deposited using significantly less inorganic additives and can be regarded as a pure copper film. Details on the chemical composition of both films can be found in Wimmer et al. [12]. The occurring changes during comparatively slow thermal cycles have extensively been discussed in a previous publication [5], where restricted microstructural changes in Film A can be attributed to the presence of incorporated inorganic residual elements. Furthermore, the films were designed in a way to show identical starting microstructures, as will be shown in a forthcoming section. Insignificantly small differences in grain size (Figure 3a), texture or twin occurrence rule out these starting parameters to influence the outcome of thermo-mechanical fatigue experiments. Besides the difference in content of inorganic elements, Film B is slightly rougher compared to Film A (Figure 3b).

Experimental Methods

To monitor microstructural and topographical changes, a tracking method, proposed by the authors in [11] was used. It is possible to observe the same site throughout the complete thermal cycling process. This tracking relies on marking a representatively large area with small Vickers microindents, using a force of 20 gf or 50 gf. These indents can easily be found using a scanning electron microscope (SEM) or an atomic force microscope (AFM).

Keeping some distance from the indents in order not to incorporate the plastically deformed regions close to the indents into the investigation, an area of at least 120x120 μm^2 is scanned with a constant step size of 0.2 µm with Electron Backscatter Diffraction (EBSD, EDAX Digiview Camera in combination with TSL Data Collection and TSL Analysis software, version 5). The EBSD system is attached to a SEM of type LEO 1525 (Zeiss, Oberkochen, Germany). For the definition of a grain to determine the mean grain size, a maximum tolerance angle of 15° and a minimum grain size of 3 pixels was allowed. The Inverse Pole Figure (IPF) maps overlaid with the image quality (IQ), were processed using a confidence index clean up with a threshold value of 0.07.

In addition, an area of 50x50 μm^2 is scanned using an AFM (Bruker Inc., Billerica, USA), where the AFM-scanned area is incorporated within the EBSD-scanned area. AFM height images have a scan resolution of 512 lines and were post-processed using Gwyddion 2.36 software [13]. With EBSD and AFM data at hand, it is possible to track microstructural (grain size and texture) and topographical (roughness) changes of the same area throughout the whole experiment. To reveal microstructural changes underneath the surface, film cross-sections were made with a dual beam Focused Ion Beam (FIB) workstation (Auriga SEM/FIB, Zeiss, Oberkochen, Germany). For cutting rough trenches, a gallium ion beam of 5 nA was used. Fine polishing was performed with a lower current of 200 pA. No deposition of heavy elements on top of the region of interest by a gas injection system was used.

To determine changes in the electrical resistivity of the material, the sheet resistance of the as-received and thermo-mechanically cycled thin metallic films was measured with a colinear four-probe array, as it is described in ASTM F390 [14]. The experimental setup consisted of a Keithley 2400 sourcemeter supplying a constant current of 50mA, a Keithley 2182 nanovoltmeter and a Cascade C4S four probe array. Omitting discrepancies between different specimens (such as the exact specimen size and shape, slight differences in metallization thickness), a tracking method was again used. The specimens of Film A and Film B, used for resistivity measurements after 0, 250 and 1000 cycles, were the same specimens only cleaned with acetic acid prior to measurements; then cycled again. The film thickness, a quantity needed for calculating the resistivity, was determined from FIB cross-sections of the starting material. The

additional layer of metallic tungsten-based diffusion barrier was not taken into account. This decision was made because of its low thickness (~5% of the copper layer) and its high resistivity (~3 times the resistivity of copper), leading to a constant total contribution of ~1% to film conductivity. The resistivity ρ was calculated via the sheet resistance $R_{\square}$ and the film thickness d according to Equation (1)

$$\rho = d * R_{\square} = d * R_{avg} * c * F * F_{sp}. \qquad \text{(Equation 1)}$$

To calculate the sheet resistance $R_{\square}$ from the average specimen resistances R_{avg}, correction factors, c, taking into account the lateral dimensions of the specimen, F, comparing the film thickness (5.1 µm) with the probe distance (1 mm) and F_{sp}, considering the probe spacing, are needed. Due to the thin film in relation to the thick substrate F can be set to 1. More details on the correction factors can be found in [14].

3 Results

Initial metallization microstructures

Figure 2 shows the initial microstructures of Film A and Film B presented as IPF maps with cross-sections of the film and scanning electron micrographs of the surface. The standard triangle shown is the colour code for reading the IPF maps and it is valid for all presented maps. The slight (111)-texture of both films (see Figure 4a for Film B, N=0) becomes evident through a slight surplus of blue coloured grains. To emphasize the grain structure, high angle grain boundaries (HAGB) with orientation changes larger than 15° are represented by white lines and Σ3 twin boundaries, HAGB having orientation changes between 59° and 61° to be precise, are shown as black lines. Both materials reveal a polycrystalline, slightly textured microstructure with a high amount of twin boundaries. The area weighted twin boundary length is ~1 µm/µm², whereas the area weighted HAGB length is ~0.5 µm/µm² for both materials. The average initial grain size is identical for all three tracked regions (see Figure 3a) and ranges between 3.2 µm ± 1.0 µm and 3.4 µm ± 1.1 µm for Film A and Film B, respectively. The determination of the grain size distribution and the mean grain size does not take into account the Σ3 twin boundary as a special coincidence site lattice boundary but as any arbitrary HAGB. The grain size would increase when removing ∑-boundaries from the calculations and only considering randomly oriented HAGBs.

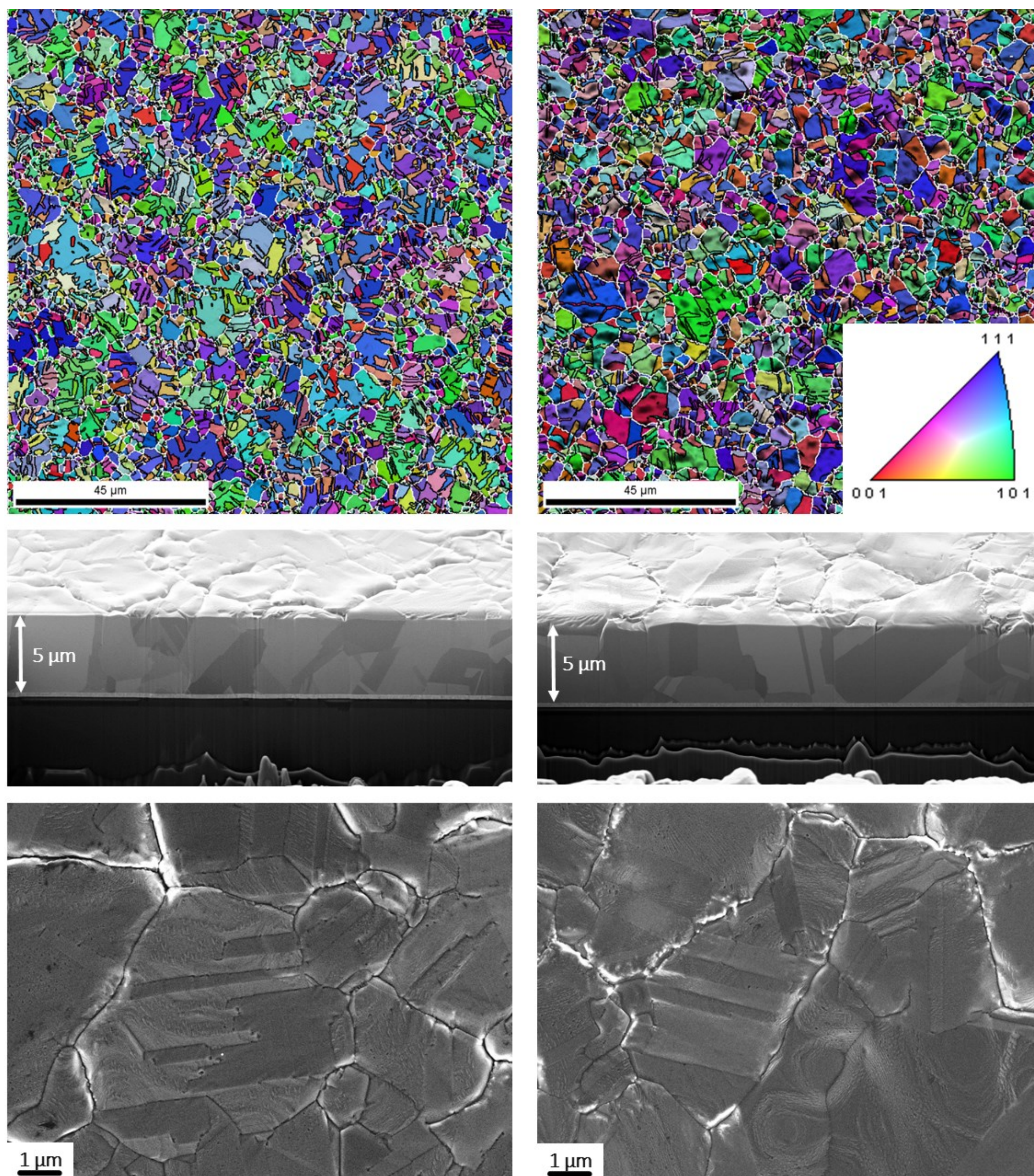

Figure 2: Initial microstructures of Film A (left column) and Film B (right column). The IPFs (first row), FIB cross-sections (second row) and scanning electron micrographs (third row) of both materials demonstrate the almost identical starting microstructure with similar grain sizes, twin occurrence, texture and film thickness. HAGB are added to the IPF maps. The standard triangle, needed for reading the IPFs, applies for all figures in this publication. Contrast and brightness of scanning electron micrographs were altered for better visibility of microstructural features.

The measured resistivities of 1.81×10^{-8} Ωm (Film A, higher inorganic element content) and 1.77×10^{-8} Ωm (Film B, pure copper) in the non-cycled state are in good accordance to the reference value of 1.68×10^{-8} Ωm (pure bulk Cu at 293K [15]). The root-mean-squared (RMS) roughness of the metallization, measured within the tracking area, are

as follows: 34 nm for Film A and 88 nm and 82 nm for the tracking regions of Film B, used for investigations of fast and slow thermal cycling. Comparing left and right side of Figure 2 and from the data given above, it can be stated that both films are, besides a slightly smoother surface of Film A, very similar in their microstructural and electrical properties.

Change of global parameters during thermo-mechanical cycling

With regard to thermo-mechanical cycling, the evolution of global film parameters such as grain size, strength of texture, resistivity and roughness are presented in this section. The grain size, an easily accessible parameter via EBSD-results, shows an increase for all three investigated specimens (Figure 3a).

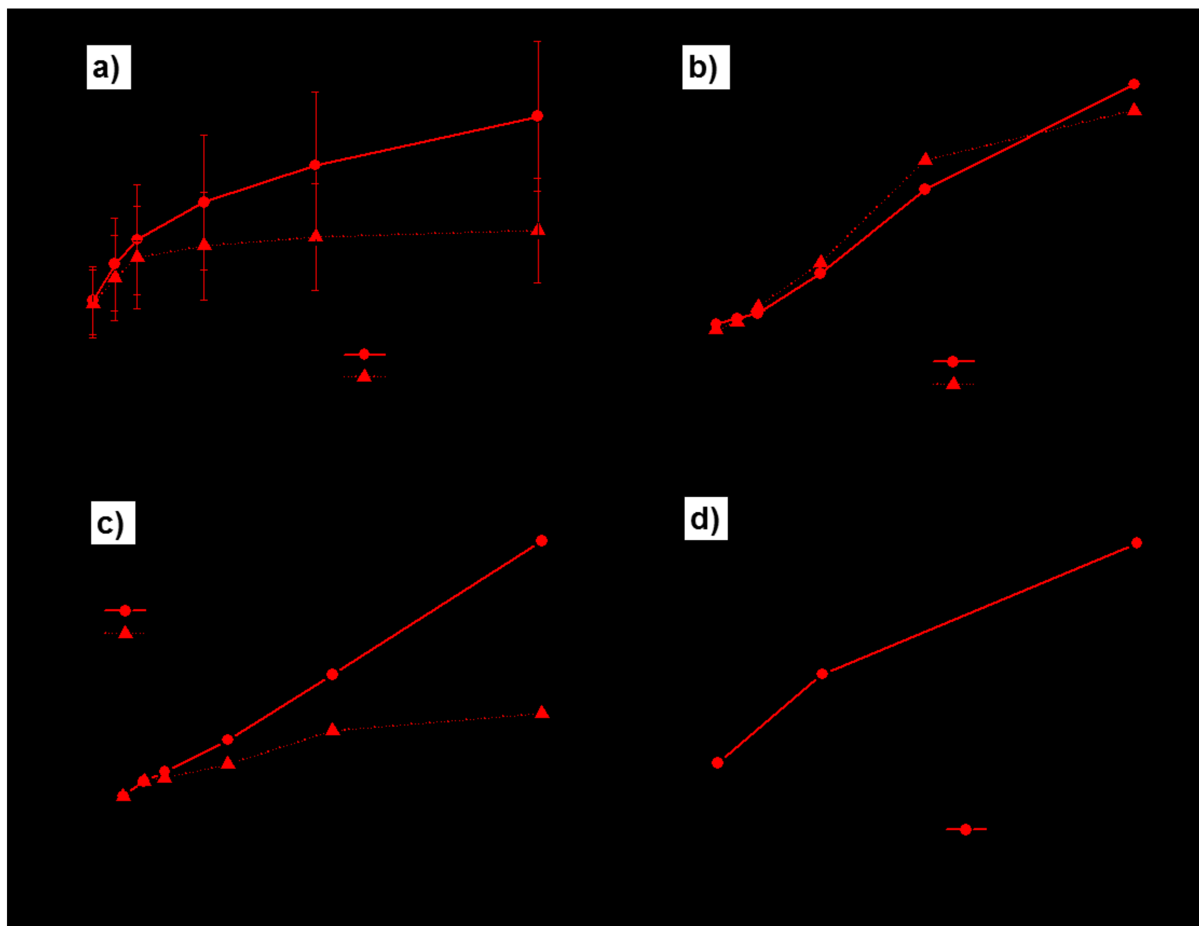

Figure 3: Change in global parameters grain size, surface roughness, texture and resistivity with increasing number of thermo-mechanical cycles. Both films were subjected to fast thermal cycling. Film B was also subjected to a slower process. a) Grain size calculated from EBSD scans. The mean grain size value and the standard deviation of a log-normal grain size distribution are shown. b) Increase in RMS roughness measured with AFM. The roughness was determined on identical regions in tracking mode. c) Change in intensity of the (100)-pole in the IPFs (see Figure 4), normalized to the intensity of the non-cycled state. The texture changes faster the higher the heating/cooling rates. While the texture of Film A almost stays constant, there is a pronounced change for the fast cycled Film B. d) Increase in resistivity of Film A and Film B with increasing number of cycles, normalized to the initial resistivity of the non-cycled specimen. No specimen that experienced the slow laser-based thermal cycling was included in this investigation.

The increase in grain size for Film B is larger compared to Film A. When only considering Film B, the fast cycling led to an increase in grain size from 3.4 µm ± 1.1 µm to 9.4 µm ± 2.5 µm after 1000 cycles, whereas the slow cycling changed the grain size from 3.3 µm ± 1.1 µm to 5.7µm ± 1.7 µm. The increase in grain size for Film A (only fast laser cycling data available) is less compared to the slow thermal cycling of Film B. There is a small increase from 3.2 µm ± 1.0 µm to 5.2 µm ± 1.8 µm after 1000 cycles. The evolution of roughness is quantified by using the RMS roughness (Figure 3b). The roughness of Film A, which is smoother in the initial stage, catches up after about 250 cycles, and the further increase in roughness is very similar. After 1000 cycles, the three films reach RMS roughness values between 320 nm and 368 nm. With respect to the initial RMS roughness, the roughness of Film A increases by a factor of 10, and the RMS roughness of Film B only increases four times. By taking the likelihood of the appearance of (100)-oriented grains from the IPFs (Figure 4 and similar data for the remaining two specimens), it is possible to derive Figure 3c. A significant increase in the (100)-texture intensity for Film B (fast cycling) can be observed, while the slow process applied to Film B exhibits a less pronounced increase. Film A revealed a marginal increase in (100)-texture. This confirms earlier work [5], where it was shown that Film B, subjected to identical thermal cycling as Film A, changes its texture faster than Film A.

To demonstrate the texture evolution of the metallization, the IPFs are presented in Figure 4, where the increasing strength of the (100)-poles with cycle number is clearly visible. From a qualitative point of view, there is a change of the appearance of IPF maps, especially for the pure material Film B, when comparing Figure 6a with Figure 6e. A typical example, which is in coincidence with the IPFs of Figure 4, is the (111)-oriented, blue grain in the upper left corner of Figure 6a containing several twins. The most prominent twin is a (100)-oriented, red region within the centre of the grain. Both processes, a growth of the whole grain, as well as an increase of the size of the twinned, red region take place. In total, the red coloured area is growing substantially, which is represented in the sequence of Figure 4.

With increasing number of thermo-mechanical cycles, there is an increase in roughness and the formation of voids may also occur [5]. Both roughness and voids could lead to

an increase in electrical resistivity ρ of the material. For the resistivity investigation, again, a tracking technique was used and the diagram shown in Figure 3d was generated from single specimens of each material using the fast cycling process. Normalized on the resistivity of the non-cycled state, ρ_0, the increase in resistivity ρ is identical for both films and reaches approximately $1.1\rho_0$ after 1000 cycles.

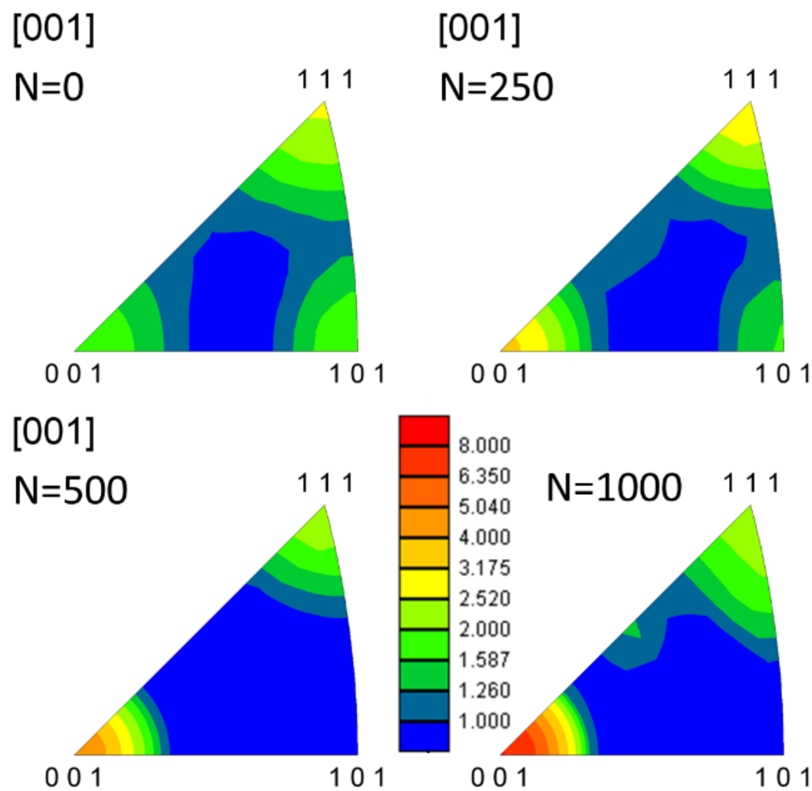

Figure 4: IPFs for Film B, fast cycling mode. Only identified grains were allowed to contribute to the texture evolution. The change in texture from a slight (111)-texture for the initial state to a pronounced (100)-texture after 1000 cycles is evident. The colour shows the likelihood of appearance of certain crystal orientations compared to a random orientation (=1, border blue/dark blue). The colour applies to all four IPFs in the figure.

Local microstructural evolution during thermo-mechanical cycling

As already shown in Figure 3, both film systems undergo significant changes of their microstructure. For a detailed mechanism-based description of these changes, Figure 5 and Figure 6 reveal crystallographic and topographical changes of Film A and Film B throughout the whole process. In both cases the same surface sections are shown after 0, 100 and 1000 cycles. For the ease of illustration, only twin boundaries are indicated in the IPF-IQ images for 1000 cycles (Figure 5e, 6e).

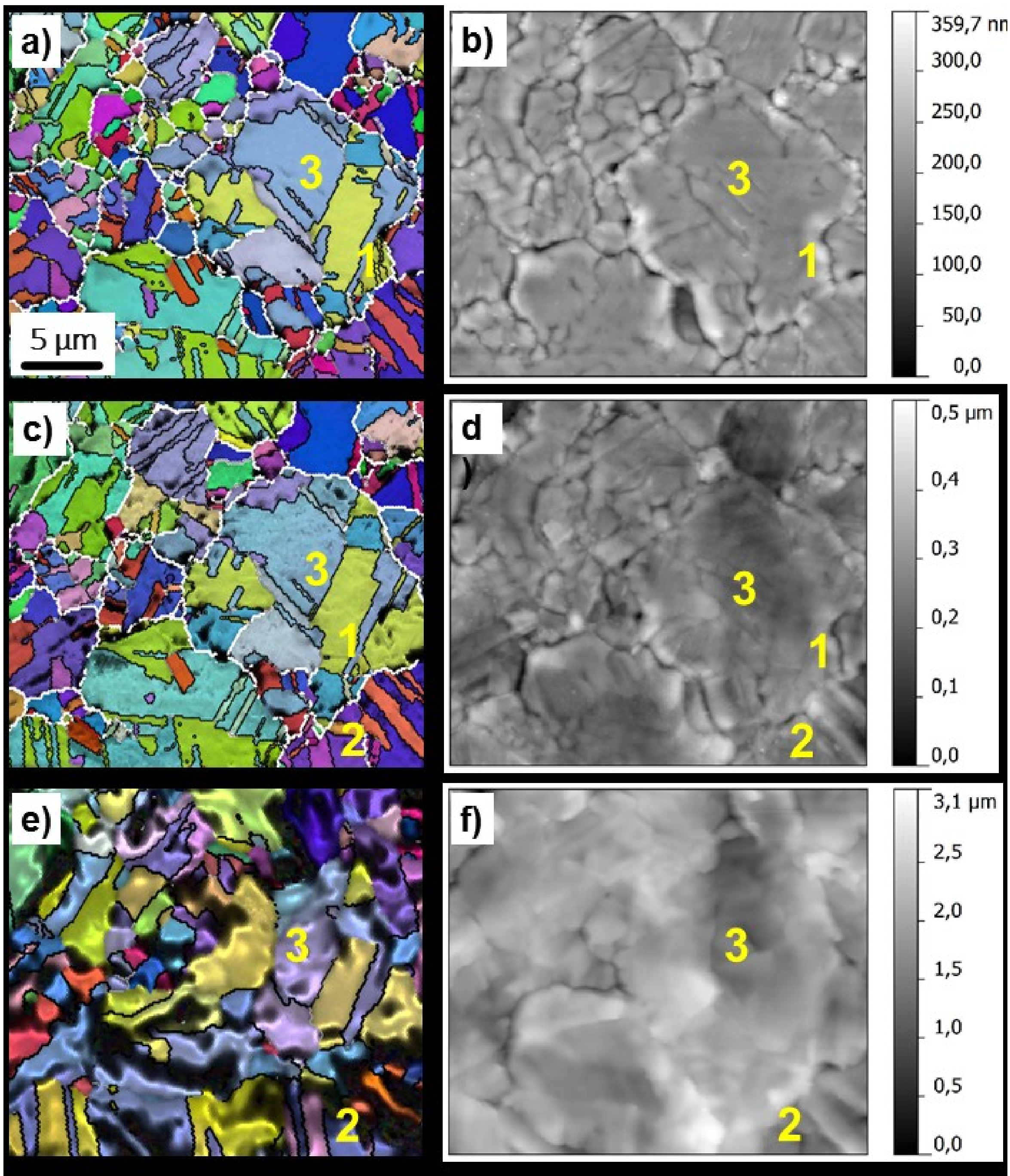

Figure 5: Site specific microstructural evolution of Film A. Crystallographic evolution (a, c, e) is matched with the topographical evolution (b, d, f) of the same surface area for 0, 100 and 1000 cycles. Additionally, three distinct features (1, 2, 3) described in the text highlight microstructural changes.

The film system with the higher inorganic element concentration, Film A, exhibits an initially non-textured microstructure (Figure 5a,b) with a dense network of twins with different twin-parent configurations within a grain. Initial cycling led to slight grain growth (Figure 5c,d), whereas further cycling up to 1000 cycles (Figure 5e,f) resulted in severe roughening at grain boundaries as well as faceting of shear band like fatigue

structures between twin-configuration. After 1000 cycles, the fraction of twin boundaries is significantly reduced compared to the as received state. Furthermore, it appears that certain grains undergo rotation throughout cycling, and therefore changing their colour in the IPF maps (Figure 5a,c,e). To highlight the most notable changes, three microstructural features are highlighted in the graphs. Feature 1 indicates normal grain growth between 0 and 100 cycles of a twinned grain. From the AFM images (Figure 5b,d) it can be seen that the original HAGB groove from the initial microstructure (Figure 5b) still exists, even though grain growth occurred. Feature 2 highlights the evolution of a shearband-like faceting of a twinned grain between 100 and 1000 cycles. Finally, grain rotation is indicated by Feature 3 where it can be seen that colour changes throughout the cycling.

Figure 6 illustrates microstructural changes with respect to thermo-mechanical cycling of Film B. The initial microstructure (Figure 6a) comprises to a randomly oriented network of grains and a wavy surface topography (Figure 6b). Upon cycling, significant grain growth can be observed, even in the early stage (Figure 6c). Further cycling led to severe roughening, indicated by faceting between grains and certain twin-parent configurations, and an overall reduction of twin boundary length. As also seen for Film A, initial cycling for Film B, did not lead to a severe change in roughness, even though pronounced grain growth was found after the first 100 cycles. The subsequent cycling led then to severe roughening. To point out dominant microstructural mechanisms, three distinct features are marked. Feature 1 represents the significant growth of a (100)/(212) parent/twin grain due to thermal cycling. This preferred growth illustrates the strong texture intensity increase of the (100) out-of-plane orientation, which can be seen in Figure 3d. This follows with a constant shrinkage of (110) oriented grains and its twins, indicated by Feature 2. This texture evolution is in agreement with Figure 4, which shows the corresponding IPFs. Feature 3 presents pronounced grain growth in the first 100 thermal cycles. The large (111) oriented grain (Figure 6c) had emerged at a site with initially randomly oriented smaller grains (Figure 6a). When looking at the topographical changes, it becomes obvious that these crystallographic changes are not necessarily linked to the topographical evolution. After 100 cycles (Figure 6d) one can

see still the distinct grooves of the small grains, which are also present in the initial stage (Figure 6b).

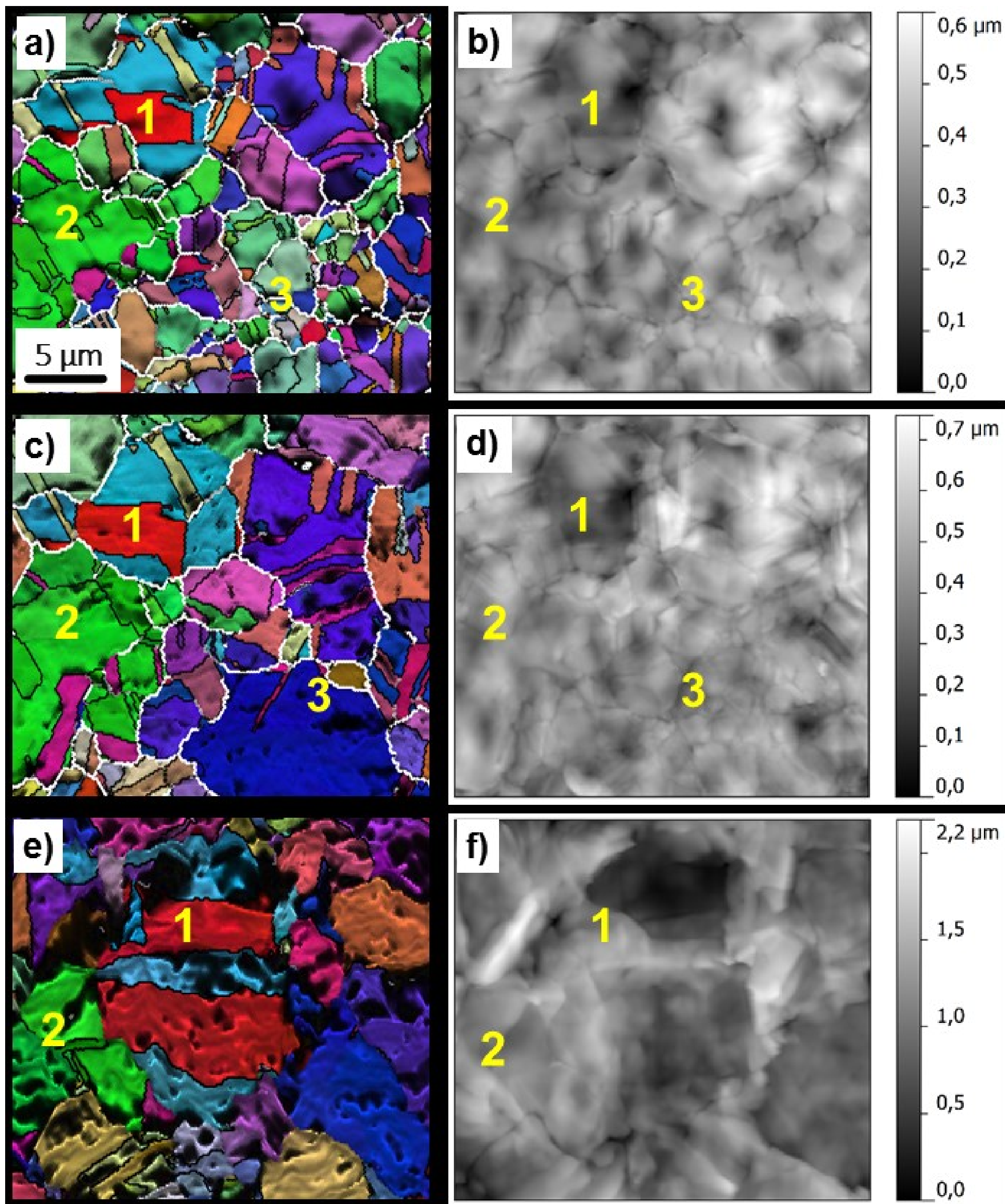

Figure 6: Site specific investigations of Film B. Crystallographic evolution (a, c, e) is matched by the topographical evolution (b, d, f) of the same surface area for 0, 100 and 1000 cycles. Three distinct features (1, 2, 3) highlight microstructural changes described in the text.

4 Discussion

When summarizing the results from the previous section, it becomes evident that distinct differences in the thermo-mechanical fatigue behaviour between Film A and Film B are present. The main differences can be addressed to grain growth, texture evolution and potential void formation.

Compared to the initial state, the grain size of Film A increases by about 60%, while Film B showed a larger increase in grain size of about 176% compared to the grain size in the as-received state. This follows the significant increase of the (100)-texture component, as will be discussed later. The presence of inorganic species in the ppm range (mostly chlorine and sulphur) in Film A are the reason for the stable microstructure, whereas the distinctively lower inorganic residual concentration of Film B leads to higher grain boundary mobility and grain growth.

Regarding the resistivity / sheet resistance, both film types show a very similar trend in increasing resistivity. Starting from about the same value of resistivity (~$1.8*10^{-8}$ Ωm for both films), the values increase by about 10% after 1000 cycles. When comparing the FIB cross-sections of both films (Figure 7 a and b), voids formed in Film A which do not seem to influence the resistivity. However, the identic behaviour in increasing resistivity matches very well to the increase in absolute values of RMS roughness, where both films again show the same behaviour with an approximately linear increase from below 100 nm (0 cycles) to above 300 nm (1000 cylces). Figure 7c and d show micrographs of the surface of cycled specimens emphasizing the similar roughness evolution. For a further discussion, the sheet resistance $R_{\square}$ shall be used instead of resistivity ρ, as the determined resistivity becomes dependent on extrinsic film properties such as the changing film thickness and voids within the material. It does not represent an intrinsic material property anymore. Assuming a small number of additional vacancies and dislocations after thermal cycling, a constant copper resistivity ρ_{Cu} throughout the whole cycling process can be used. Thus, the increase in sheet resistance comes from a changing morphology of the films with the contribution of roughness being more dominant than the contribution of the voids. It seems that the electric current can bypass small, globular or columnar voids easily without a significant increase in the current pathway, whereas the long-range changes in surface topography,

and thus film thickness, are responsible for the resistivity increase. An increasing value of RMS roughness can also be seen as a wider spread of the film thickness distribution that leads to a higher sheet resistance, which scales with $1/d$. In other words, a serial connection of two identical resistors, with their resistance being defined by their thickness d, would increase its total resistance when changing the thicknesses of both resistors to d+Δd and d-Δd.

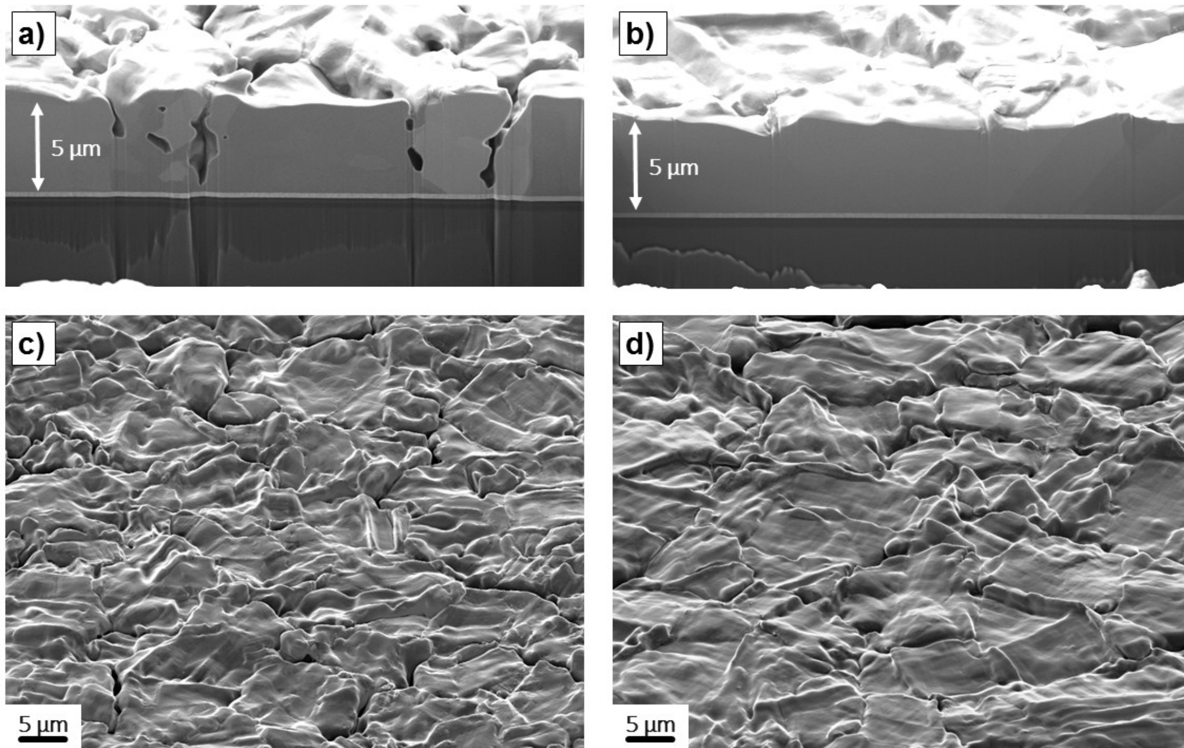

Figure 7: SEM images of FIB-made cross-sections (top row) and the surface (bottom row) and of Film A (left column) and Film B (right column). The micrographs of the surfaces were taken at an inclination of 54°, also used for FIB-cutting, emphasizing the roughness evolution of the films. Although the roughness evolution of both films is very similar (see Figure 3b), the difference becomes evident in the cross-sections. Voids formed during thermo-mechanical cycling in Film A. Contrast and brightness were altered for better visibility of microstructural features.

Comparing the results on the development of grain size and roughness with results described in [5] one can judge that the higher the heating / cooling rates, and thus the externally applied strain rate, led to a faster increase in roughness and grain size. For Film B, the infrared cycling with the same temperature range (170°C – 400°C) led to a grain size of 5.3 µm ± 1.8 µm after 1000 cycles. When using the fast laser cycling mode, however, the increase in grain size is significantly larger after the same amount of cycles (9.4 µm ± 2.5 µm). Such accelerated grain growth can also be found for Film A. Here,

slow infrared cycling increased the grain size by a small amount from 2.8 µm ± 0.9 µm to 3.5 µm ± 1.1 µm after 1000 cycles, whereas fast laser cycling increased the grain size from 3.2 µm ± 1.0 µm to 5.2 µm ± 1.8 µm after 1000 cycles.

The same trend holds true for RMS roughness values, where the increase is faster for laser cycling in comparison to slow testing. For slow furnace cycling, the roughness values only changed from about the same starting values to 100 nm (Film A) and 150 nm (Film B) after 1000 cycles. Laser cycling led to higher RMS roughness values between 320 nm and 368 nm, respectively.

Based on works of Flinn et al. [16] and Ashby et al. [17], these amplified changes in grain growth and roughness at higher strain rates might be attributed to the critical stress required for dislocations to surpass obstacles of a free energy ΔF. This critical stress at the transition from linear elastic behaviour to stress relaxation in a stress vs. temperature diagram is given by Equation (2)

$$\sigma = \tau \left\{ 1 - \left[\frac{kT}{\Delta F * \ln(\dot{\varepsilon_p}/\dot{\varepsilon_0})} \right] \right\}, \qquad \text{(Equation 2)}$$

with τ being the stress that is required to reduce the effective height of the obstacle to zero, k being the Boltzmann constant, T the temperature, $\dot{\varepsilon_0}$ a characteristic constant and $\dot{\varepsilon_p}$ the plastic strain rate. Although the dependence of stress on strain rate is logarithmically weak, the occurrence of plastic behaviour is, nevertheless, a function of the heating and cooling rate. The higher stresses for higher strain rates could lead to stress driven grain boundary migration, whereas the limited time for diffusional processes could hinder the surface from being smoothened after dislocation activity had generated a rough surface.

The statement that higher stresses develop during faster cycling is supported by experimental results of the (100)-texture evolution. A preferable growth of the (100) out-of-plane orientation led to an occurrence, which is five times more likely after 1000 cycles for Film B. For the slow infrared cycling, the appearance of the (100)-texture component was increasing only by a factor of about 1.45 after 1000 cycles for Film B [5]. The reason for the preferential growth of the (100)-component is that the amount of applied total strain is externally defined by the difference of the coefficients of thermal

expansion. For copper, the (100) texture minimizes the elastic strain energy density since it has the lowest biaxial modulus [18], thus, the difference in elastic strain energy density can be seen as driving force for preferable (100) texture evolution. An example for the difference in strain energy ΔW_{ε} for the fully plastic case is given by

$$\Delta W_{\varepsilon} = \frac{{\sigma_{111}}^2}{M_{111}} - \frac{{\sigma_{100}}^2}{M_{100}} \quad , \qquad \text{(Equation 3)}$$

where σ_{111} and σ_{100} are the arising stresses in the particularly oriented grains with the corresponding biaxial moduli M_{111} (261 GPa [19]) and M_{100} (115GPa [19]) The example uses (111) and (100)-oriented grains, since they have the largest difference in the biaxial modulus. From Equation 3 it becomes evident that the driving force and, hence, the accelerated texture evolution are strongly dependent on the resulting stresses within the grains. In both experimental cases (infrared furnace, laser heating device), the temperature change was between 170°C and 400°C, thus, there was no difference in the total applied strain. Therefore, it seems that for the laser cycling the elastic regime becomes larger, resulting in larger stresses and a higher driving force ΔW_{ε}.

The question whether this behaviour holds true for even shorter heating/cooling pulses, e.g. in the milliseconds range or below, as they are achieved in real devices, cannot be answered within this study and is subject to future research.

5 Conclusion

The investigation of copper metallizations on silicon substrates that where repeatedly heated with a newly developed laser setup provide the following insights:

- The increase of grain size, related to the applied thermo-mechanical load (thermal cycling) of copper metallizations was investigated. Film A, with a notable incorporation of inorganic species (~100 ppm) revealed a significantly slower grain growth.
- The texture of the tracked regions changes, especially for the fast laser cycled pure Film B, to a pronounced (100)-texture. This is because of growth of grains featuring a preferential orientation in relation to the biaxial tensile/compression stress field within the metallization. Grain rotations are existent but too weak, to lead to significant contributions to texture changes.

- Results are in agreement with investigations using slowly cycled material. The higher the heating / cooling rate, thus, the higher the externally applied strain rate, the faster the changes in grain size, RMS roughness and texture occur. This is less evident for pure Film A.
- The surface topography, quantified by RMS roughness values, shows for both films a linear increase with cycle number.
- The relative increase in sheet resistance is identical for both films, which leads to the assumption that this is due to the increase in film roughness, but not due to the localized formation of voids.
- The laser setup is a very versatile tool for quick screening of thermo-mechanical fatigue of metallizations on silicon substrate. Pieces from wafers can already be used without any further preparation.
- The current experimental setup can easily be adjusted to be used for any other bulk or layered material.

6 Acknowledgements

The work was performed in the project EPPL, financially supported by grants from Austria, Germany, The Netherlands, France, Italy, Portugal, and the ENIAC Joint Undertaking (ENIAC JU Grant Agreement no. 325608). This project is co-funded within the programme “IKT der Zukunft” by the Austrian Ministry for Transport, Innovation and Technology. Support from the company Dr. Mergenthaler GmbH & Co KG (Neu-Ulm, Germany) is gratefully appreciated.

7 References

[1] C.A. Swenson, Recommended Values for the Thermal Expansivity of Silicon from 0 to 1000K, Journal of Physical and Chemical Reference Data. 12 (n.d.) 179–182.

[2] T.A. Hahn, Thermal Expansion of Copper from 20 to 800 K—Standard Reference Material 736, Journal of Applied Physics. 41 (1970) 5096–5101. doi:10.1063/1.1658614.

[3] A.A. Taylor, S.H. Oh, G. Dehm, Microplasticity phenomena in thermomechanically strained nickel thin films, Journal of Materials Science. 45 (2010) 3874–3881. doi:10.1007/s10853-010-4445-0.

[4] W. Heinz, R. Pippan, G. Dehm, Investigation of the fatigue behavior of Al thin films with different microstructure, Materials Science and Engineering: A. 527 (2010) 7757–7763. doi:10.1016/j.msea.2010.08.046.

[5] S. Bigl, S. Wurster, M.J. Cordill, D. Kiener, Advanced Characterization of thermo-mechanical fatigue mechanisms of different copper film systems for wafer metallizations, Thin Solid Films, Submitted. (n.d.).

[6] W. Heinz, W. Robl, G. Dehm, Influence of initial microstructure on thermomechanical fatigue behavior of Cu films on substrates, Microelectronic Engineering. 137 (2015) 5–10. doi:10.1016/j.mee.2014.10.024.

[7] W.D. Nix, Mechanical properties of thin films, MTA. 20 (1989) 2217–2245. doi:10.1007/BF02666659.

[8] S. Bigl, W. Heinz, M. Kahn, H. Schoenherr, M.J. Cordill, High-Temperature Characterization of Silicon Dioxide Films with Wafer Curvature, JOM. 67 (2015) 2902–2907. doi:10.1007/s11837-015-1600-8.

[9] M.A. Green, M.J. Keevers, Optical properties of intrinsic silicon at 300 K, Prog. Photovolt: Res. Appl. 3 (1995) 189–192. doi:10.1002/pip.4670030303.

[10] K.L. Chavez, D.W. Hess, A Novel Method of Etching Copper Oxide Using Acetic Acid, J. Electrochem. Soc. 148 (2001) G640–G643. doi:10.1149/1.1409400.

[11] S. Bigl, S. Wurster, M.J. Cordill, D. Kiener, Site Specific Microstructural Evolution of Thermo-mechanically Fatigued Copper Films, Berg Huettenmaenn Monatsh. 160 (2015) 235–239. doi:10.1007/s00501-015-0355-4.

[12] A. Wimmer, M. Smolka, W. Heinz, T. Detzel, W. Robl, C. Motz, et al., Temperature dependent transition of intragranular plastic to intergranular brittle failure in electrodeposited Cu micro-tensile samples, Materials Science and Engineering: A. 618 (2014) 398–405. doi:10.1016/j.msea.2014.09.029.

[13] D. Nečas, P. Klapetek, Gwyddion: An open-source software for SPM data analysis, Central European Journal of Physics. 10 (2012) 181–188. doi:10.2478/s11534-011-0096-2.

[14] F390 - 98, Standard Test Method for Sheet Resistance of Thin Metallic Films With a Collinear Four-Probe Array, 2003.

[15] CRC Handbook of Chemistry and Physics, 87th Edition, Taylor and Francis, 2007.

[16] P.A. Flinn, D.S. Gardner, W.D. Nix, Measurement and Interpretation of stress in aluminum-based metallization as a function of thermal history, IEEE Transactions on Electron Devices. 34 (1987) 689–699.

[17] M.F. Ashby, H.J. Frost, The kinetics of inelastic deformation above 0K, in: Constitutive Equations in Plasticity, MIT Press, Cambridge, MA, 1975: pp. 117–147.

[18] C.V. Thompson, R. Carel, Texture development in polycrystalline thin films, Materials Science and Engineering: B. 32 (1995) 211–219. doi:10.1016/0921-5107(95)03011-5.

[19] P. Sonnweber-Ribic, P. Gruber, G. Dehm, E. Arzt, Texture transition in Cu thin films: Electron backscatter diffraction vs. X-ray diffraction, Acta Materialia. 54 (2006) 3863–3870. doi:10.1016/j.actamat.2006.03.057.

VIII Publication E

Film thickness dependent microstructural changes of thick copper metallizations upon thermal fatigue

Stephan Bigl, Claus O. W. Trost, Stefan Wurster, Megan J. Cordill, Daniel Kiener

Journal of Materials Research (2016); submitted-revised-submitted

Abstract:

With increasing performance requirements in power electronics, the necessity has emerged to investigate the thermo-mechanical behaviour of thick Cu metallizations (≥ 5 µm). Cu films on rigid substrates in the range of 5-20 µm were thermally cycled between 170-400°C by a fast laser device. Compared to the initial microstructures, a texture transition towards the {100} out of plane orientation with increasing film thickness was observed during thermo-mechanical cycling, along with abnormal grain growth in the {100}-oriented grains and a gradual development of sub-structures in a crystallographic arrangement. Compared to the well-studied thin Cu film counterparts (≤ 5 µm), the surface damage showed a $1/h_f$ dependency. Transition from an orientation independent (h_f = 5 µm) to an orientation specific thermo-mechanical fatigue damage (h_f = 10, 20 µm) was observed following a higher damager tolerance in {100} oriented grains.

1 Introduction

Since the large scale production of integrated circuits in the 1960s, thin film materials for microelectronic devices have become a major topic in the modern materials science community. The ongoing performance increase with the number of transistors and switching frequency coupled with the miniaturization of semiconductor components require sophisticated deposition processes and excellent film material properties [1]. In many silicon-based microelectronic devices increasing power densities lead to significant temperature rises up to ~ 400°C within the microsecond regime during switching operations [2]. This results in large thermal stresses due to different coefficients of thermal expansion (CTE) of the materials, where plastic deformation can occur if the yield stress of the metallization is reached [3]. Such a repetitive dynamic temperature rise leads to thermo-mechanical damage of the metallization in the form of severe surface roughening and voiding. These features can result in local excess temperatures leading to a thermal runaway and local melting of silicon [2].

In order to overcome these problems one key concept of metallization development is to increase the film thickness (h_f), which leads to a greater specific heat capacity and longer operational lifetime. In a previous study, it has been shown that increasing the copper metallization thickness to 20 µm will result in the largest relative benefit gain such as the maximum peak temperature during a power pulse [4]. Copper, used in modern power semiconductor metallization schemes [5], exhibits very interesting structural properties. Besides its excellent electrical and thermal properties, copper has a very low stacking fault energy (SFE) resulting in a high number of twin boundaries [6], as well as a large elastic anisotropy factor [7]. These attributes result in a large variety of initial microstructural characteristics, such as grain size, *d*, and texture, because they are directly coupled to the corresponding film thickness [8]. In copper films a pronounced texture transition from a dominating {111} texture at small thickness (< 1 µm) to a high fraction of {100}-oriented grains at greater film thickness (5-10 µm) can be observed, as well as a different grain size distribution between the two texture components [9]. These initial microstructural differences in thicker Cu films lead to the presumption that regardless of the chosen fatigue experiment, the microstructural

evolution and related fatigue damage in copper films will depend on the particular film thickness.

In literature numerous studies report on the (thermo)-mechanical fatigue of copper films in the range of h_f = 0.1-5 µm on thick substrates [10-19]. Fatigue damage, which is often described by extrusions/intrusions and severe roughening on the film surface, is directly correlated to film thickness where the height and extrusion density decrease with decreasing thickness [16]. Other studies attribute localized differences in the fatigue damage to the distinctly different behaviour of {100} and {111} out-of-plane oriented grains [13, 16, 20-22]. Although mechanisms are not fully understood, authors emphasized that dislocation substructures (e.g. {100} walls) being more likely in {100}-oriented grains [16], and the large difference in grain resolved in-plane stress σ ($\sigma_{111}/\sigma_{100}$ ~ 2.3) due to elastic anisotropy [22], are potential reasons why film microstructures with different fraction of {100} and {111} grains behave differently with respect to fatigue testing.

The question arises as to which thermo-mechanical behaviour can be observed when $h_f \geq 5$ µm where the fraction of {100}-oriented grains is expected to significantly increase [9]. Current literature on Cu foils indicates a lower tensile strength for 20 µm foils due to the increase of the soft {100} texture component but does not provide results with respect to thermo-mechanical fatigue [23]. Presented here are experimental results of thick thermo-mechanically loaded copper films, ranging from 5 to 20 µm film thickness and with various initial film textures. The local microstructural evolution, which is based on a site-specific tracking method [24], in combination with wafer curvature measurements, local scanning electron microscopy (SEM) studies, and surface roughness measurements are used to evaluate the film thickness influence upon thermo-mechanical fatigue.

2 Materials and Experimental

Materials synthesis and preparation

All samples were prepared via sputter and electrochemical deposition. First, a tungsten-based (~100 nm) adhesion layer was sputtered on 725 µm thick silicon wafers with a (100) orientation, followed by a 300 nm sputtered Cu seed layer. On top of the seed

layer, electrochemical deposition was used and the deposition time was adjusted so that final copper film thicknesses of 2.5, 5, 10 and 20 μm were obtained. The electrolyte was designed to result in an almost impurity-free Cu film [25, 26]. All samples were subjected to a 30 min heat treatment at 400 °C in a reducing atmosphere (forming gas) to establish a stable room temperature microstructure.

Experimental techniques

The basic thermo-mechanical characterisation of the films was performed using a wafer curvature system for in-situ film stress characterisation up to 1000 °C [27]. With a multiple optical beam sensor, kSA MOS (k-Space Associates, Inc. Dexter, 48130 USA), the film stress evolution was measured from room temperature to 400°C using a heating and cooling rate of 10°C/min.
To experimentally simulate rapid temperature rises comparable to thermo-mechanical loading of the copper metallizations by high power pulses in power electronics, samples with lateral dimensions of 7 x 7 mm were thermally cycled in a custom-built fast thermal laser cycling device in an reducing atmosphere (forming gas, chamber pressure ~160 mbar) [28]. The samples were thermo-mechanically loaded between 170 °C and 400 °C, resulting in a total applied thermal strain of about 0.7% per cycle due to the CTE mismatch using the average CTE values for Cu and Si in the corresponding temperature range [29, 30]. One laser cycle corresponds to an average heating rate of 1050 °C/s and a cooling rate of 110 °C/s with a total cycle time of approximately 2 s. For details on the cycling process see [15, 28].

After marking the film surface with Vickers orientation indents, the surface and microstructural evolution within a representative surface area was studied using a Dimension 3100 (Bruker Inc., Billerica, USA) atomic force microscope (AFM) and a SEM LEO 1525 (Zeiss Inc., Oberkochen, Germany) with electron backscatter diffraction (EBSD) analysis. For more information about the site specific evaluation see [24]. Between thermal cycling, samples were subjected to a selective etch to remove any copper oxide using a 100 vol% acetic acid solution at 35-40 °C for 2 - 4 minutes [31]. AFM images were made in tapping mode and post image analysis was performed using Gwyddion 2.45 software [32]. For EBSD investigations, depending on the grain size, the scan size varied from 120x120 μm^2 to 500x500 μm^2 with a step size between 0.2 and

0.9 µm. For all scans an acceleration voltage of 20 kV and a 120 µm aperture size were used and post EBSD analysis was performed with the TSL Analysis v5 software. SEM micrographs were obtained using the secondary electron mode with a 20 µm aperture size and 6 kV acceleration voltage.

3 Results and Discussion

Initial microstructural analysis

The specimens in the as-received state showed a clear film thickness dependence with respect to initial grain size and texture for $h_f \geq 5$ µm (Figure 1). A randomly oriented polycrystalline grain structure was obtained for $h_f = 2.5$ and 5 µm (Figure1a, 1b). With increasing film thickness a predominant {100}-texture was observed for $h_f = 10$ µm (Figure 1c) and for $h_f = 20$ µm (Figure 1d). The stereographic coloured triangle in Figure 1a was used for every grain orientation map (EBSD image) in this study. The grain size is a function of film thickness (see Table I). An average grain size of 2.5 ± 0.8 µm (including primary twin boundaries) was observed for the thinnest Cu film ($h_f = 2.5$ µm) and d increased to 17.4 ± 3.9 µm for $h_f = 20$ µm. The initial {100} out-of-plane orientation fraction scales linearly with h_f and a significant increase of the grain size (including primary twins) was observed. This is in good agreement with literature [8, 33], where driving forces such as the minimization of interfacial energy $\Delta\gamma_i$ and strain energy ΔW_ε explain the increase of the grain size and preferable {100} out-of-plane direction, respectively. Observations of the present films indicate that the texture transition does occurs at thicknesses greater than 5 µm since the texture appearance (Figure 1a, b) of the $h_f = 2.5$ µm Cu film are almost identical to $h_f = 5$ µm, which deviates from other studies where the transition thickness was found to lie between 3 to 5 µm and the absolute {100} texture strength was different with respect to h_f [9]. The 2.5 µm thick film is used here only to illustrate the differences between thin films (≤ 5 µm) and thick films (≥ 5 µm), which is the focus of this paper.

In order to study the change in texture in a quantitative manner, columnar grains are assumed and the mean elastic modulus is calculated. By taking the elastic constants of the stiffness tensor for copper (c_{11}: 168.4 GPa, c_{12}: 121.4 GPa c_{44}: 75.4 GPa) [34], the

mean elastic modulus and as a function of the initial microstructures was calculated using the EBSD information (for detailed information see [15]).

Table I: Initial film properties of the four Cu film thicknesses.

Film thickness [µm]	Grain size [µm]	Elastic modulus (EBSD) [GPa]	Elastic modulus (W.C.)* [GPa]	Thermoelastic - slope [MPa/K]	Poisson´s ratio [-]
20	17.4 ± 3.9	84 ± 39	77	-1.77	0.387
10	6.1 ± 1.7	100 ± 37	89	-1.97	0.365
5	3.4 ± 1.1	112 ± 31	101	-2.20	0.350
2.5	2.5 ± 0.8	112 ± 30	133	-2.88	0.350

* W.C. stands for wafer curvature measurements

As shown in Table I, for h_f = 2.5 and 5 µm thick films, the calculated mean elastic modulus is 112 GPa. These two films have an almost randomly oriented microstructure, where an elastic modulus of 109 GPa [15] was determined. With film thicknesses greater than 5 µm the average elastic modulus decreases due to the increase of the soft {100} out-of-plane texture component.

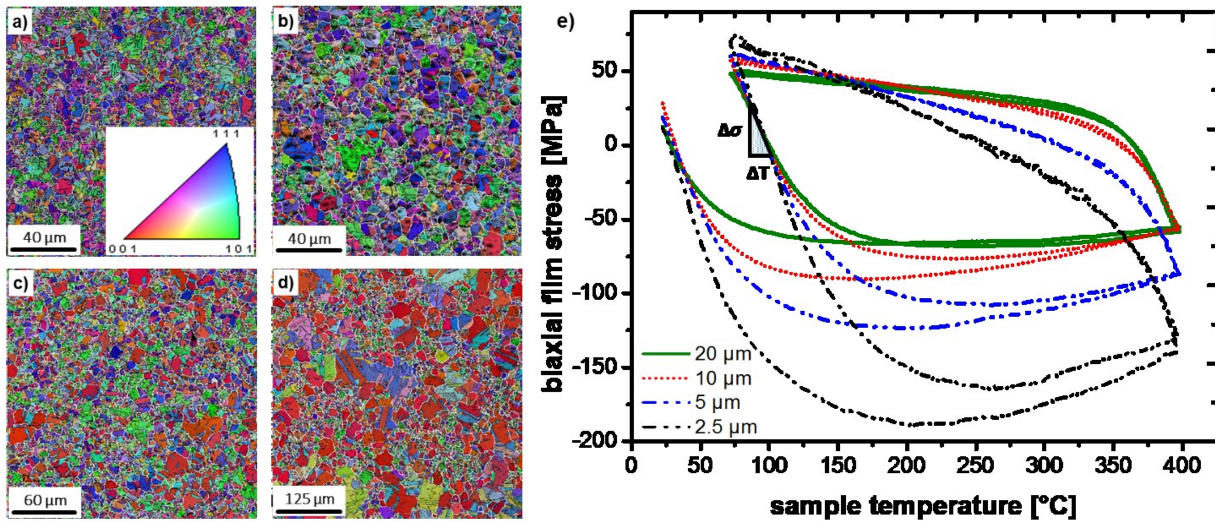

Figure 1: (a-d) Initial film microstructures of the 2.5, 5, 10 and 20 µm copper films presented by grain orientation maps with IQ analysis. (e) The initial thermo-mechanical behaviour changes as function of film thickness. Standard IPF triangle is valid for all EBSD images. (Colour online)

The basic thermo-mechanical behaviour using the stress-temperature evolution (Figure 1e) also varies as a function of film thickness. The biaxial film stress is shown between room temperature and 400 °C of the first cycle and between 80 to 400°C of the second cycle. Starting with similar tensile film stresses, a maximum compressive stress of -190 MPa was observed for h_f= 2.5 µm, which decreases to approximately 120, 80 and 60

MPa for h_f= 5, 10 and 20 µm, respectively. In terms of the shape of the film stress hysteresis an influence of the changing initial film texture was observed. The two random textured microstructures (h_f= 2.5 and 5 µm) exhibit a very similar thermo-mechanical behaviour and a gradual change from elastic to plastic film stress evolution is observed.

For film thicknesses ≥ 5µm the stress hysteresis changes to a very sharp elastic to plastic film stress behaviour, most notably for h_f= 20 µm. It can be seen that two pronounced elastic regions are present for the heating and cooling segments and are followed by plastic flow at an almost constant stress. The transition of the stress-temperature behaviour can also be observed in the decrease of the thermoelastic slopes with increasing film thicknesses (Table I). In order to quantify the correlation of the observed thermo-mechanical behaviour with respect to film thickness, the elastic film modulus E_f was determined in the temperature range of 90-110°C (second cycle) using:

$$\frac{d\sigma_f}{dT} \sim \frac{\Delta\sigma_f}{\Delta T} = \left[\frac{E_f}{(1-\upsilon_f)}\right] * (\alpha_s - \alpha_f) \quad (1)$$

where the differential change of film stress as a function of sample temperature can be seen as the thermoelastic slope $\Delta\sigma_f/\Delta T$. The corresponding stress slopes are the product of the biaxial modulus of the film, where υ_f denotes Poisson's ratio of the film, and the thermal expansion mismatch between the substrate, α_s, and the film, α_f, in the given temperature range. As shown in Table I, the thermoelastic slopes decreased with increasing h_f. The initial Poisson´s ratios of the films have been calculated (Table I) by calculating Poisson´s ratio for the three main orientations (<111>, <110> and <100>) according to references [35, 36] (via calculating $M_{[hkl]}$ and $E_{[hkl]}$). Corresponding Poisson´s ratios ($\upsilon_{<100>}$: 0.42, $\upsilon_{<110>}$: 0.44, $\upsilon_{<111>}$: 0.27) where then weighted using the fractional grain areas of the crystal orientations (<111>, <110> and <100>) determined using the EBSD images (a maximum orientation tolerance of 8° was used). The remaining texture components assigned to υ = 0.35 which can be attributed to a texture-free copper film [34]. As shown in Table I, υ_f increases from υ_f = 0.35 in the two texture-free films (h_f = 2.5 and 5µm) to υ_f = 0.386 for the thickest copper film. The trend of Poisson´s ratio with respect to film thickness is quantitatively confirmed by the calculated elastic moduli in the range of 90-110 °C (using a Δα of 14.1 ppm/K [15]), where the decrease of E_f correlates to the E determined from the EBSD measurements.

The overall elastic film behaviour relates to an increase of the softer {100} texture component for thicknesses between 5 and 20 µm.

In terms of the elastic properties a good correlation between the wafer curvature and EBSD data was found for films thicker than 5 µm, considering that Cu has a temperature coefficient of elastic modulus of about -245 ppm/°C [34]. However, for the 2.5 µm Cu film a rather large discrepancy of the elastic modulus values (Table I) was found indicating that in thinner films (≤ 5 µm) other mechanisms overlap with the elastic response. It appears that the thermoelastic response for thin Cu films is inversely proportional to the film thickness and does not directly correlate to the initial elastic properties based on the microstructure and texture. The same behaviour as the 2.5 µm film was also reported in another study where the thermo-elastic slope for 1 µm thin Cu films was found to be 3.6 MPa/K (in comparison: 2.88 MPa/K for 2.5 µm) [37].

It was also observed that the stress relaxation behaviour changed with increasing h_f. While the two thinner Cu films (2.5 and 5 µm) showed distinct stress relaxation after reaching the maximum compressive film stress, the 20 µm thick Cu film illustrated plastic flow at an almost constant stress level of around -60 MPa / + 35 MPa. Such thermo-mechanical behaviour is often referred as Al-type (e.g. passivated films) [38], where thermally activated (stress driven) dislocation glide was proposed as the dominant deformation mechanism [3]. Cu-type curves, for example the stress-temperature behaviour of the $h_f = 2.5$ µm, use creep mechanisms such as power law breakdown or diffusional creep, which involve atomic diffusion [39]. Considering that diffusion paths such as grain boundaries and twins were found to scale inversely proportional with h_f the obtained results by wafer curvature would indicate a gradual change from a Cu-type to an Al-type with increasing h_f.

Global microstructure evolution

Since a large increase of the {100} out-of-plane texture component as well as different thermo-mechanical behaviour can be observed with Cu film thicknesses ≥ 5 µm, samples with $h_f = 5$, 10 and 20 µm were thermo-mechanically cycled up to 1000 cycles with the fast thermal laser cycling device.

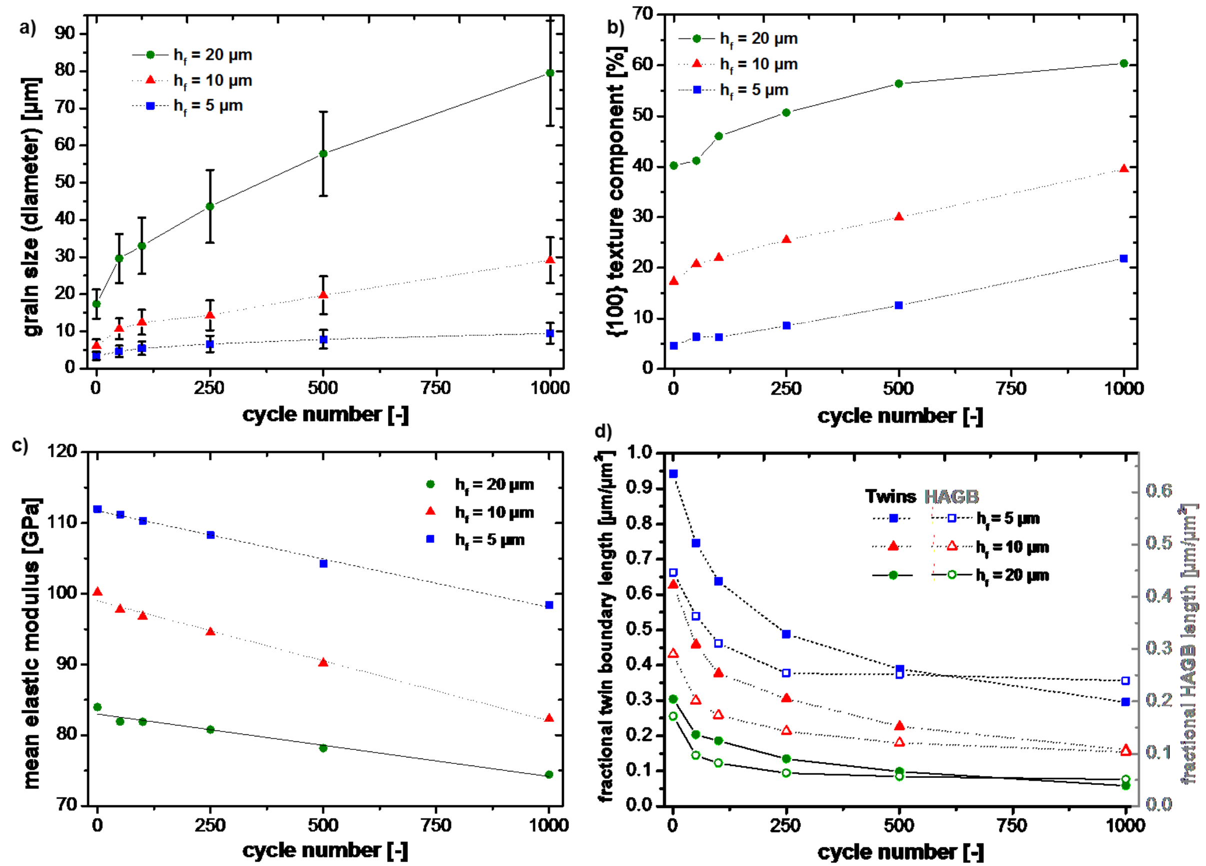

Figure 2: (a) Grain size evolution of the 5, 10 and 20 µm thick Cu films as a function of cycle number and (b) the corresponding fractional area evolution of the {100} texture component. (c) Evolution of the mean elastic modulus determined from EBSD images. (d) Fractional twin/HAGB evolution with respect to the cycling state. (Colour online)

In Figure 2, the global microstructural parameters of the three samples are shown as a function of cycle number. Figure 2a indicates that significant grain growth occurs during thermal cycling in the three Cu films. In all three samples the increase of the grain size (including twins) was the largest during the first 50 cycles followed by a constant increase up to 1000 thermal cycles. The grain size increased from 3.4 ± 1.1 µm up to 9.5 ± 2.8 µm (h_f = 5µm), from 6.1 ± 1.7 µm up to 29.1 ± 6.1 µm (h_f = 10 µm) and from 17.3 ± 3.9 µm up to 79.5 ± 14.1 µm (h_f = 20 µm).

Figure 2b presents the fractional area of the {100} texture evolution as function of thermal cycles. A similar steady (linear) texture increase for all three film thicknesses is seen, where the area fraction for h_f = 5 µm increased from 5 up to 22%, for h_f = 10 µm from around 17 up to 39% and for h_f = 20 µm the values increased from 40 up to 60%. As a result of the prominent {100} texture development, the average elastic moduli (Fig.

2c, incl. linear fit lines) of all specimens decreases during thermo-mechanical cycling. The thinnest Cu film with h_f = 5 µm shows a decrease of the mean elastic modulus from 112 GPa to 98 GPa, while the thicker films h_f = 10 and 20 µm exhibit a decrease from 100 GPa to 82 GPa and from 84 GPa to 74 GPa, respectively.

In order to again quantitatively compare the three film thicknesses from an energetic point of view a columnar grain structure is assumed. The biaxial strain, M, generated during cycling leads to different elastic strain energy densities, W, in the Cu films because the strain energy is orientation dependent in the elastic regime and described by [40]

$$W = M_{hkl}\,\varepsilon^2. \qquad (2)$$

Using the elastic moduli from Figure 2c, the calculated initial biaxial moduli of $M_{5\mu m}$, $M_{10\mu m}$ and $M_{20\mu m}$ are 172 GPa, 157 GPa and 137 GPa, respectively, can be determined. After 1000 thermal cycles the respective biaxial moduli were lowered to 154 GPa, 131 GPa and 122 GPa, for 5, 10 and 20µm film thickness, respectively. The as received data from the 2.5 µm thick film are used as a reference because it exhibits an almost random texture. The minimization of elastic strain energy can be calculated by [40]

$$\Delta W = (M_{2.5\mu m} - M_{hf})\,\varepsilon^2. \qquad (3)$$

Applying Equation 3 leads to a reduction of the elastic strain energy after 1000 cycles of about 18xε^2 GJ/m^3, 41xε^2 GJ/m^3 and 50xε^2 GJ/m^3, compared to a randomly oriented polycrystalline film, for h_f = 5, 10 and 20µm, respectively. The reduction of the elastic strain energy emphasizes the dominant effect of the {100} out-of-plane grain growth. Considering that the <100> orientation has a M_{100} = 115 GPa [9], biaxial moduli calculated from the obtained EBSD analysis (Figure 2c) reveal a transition from an elastically anisotropic microstructure to an isotropic structure with increasing film thickness and cycling stage. The evolution of the fractional (primary) twin boundary and high angle grain boundaries (HAGB) lengths are both presented in Figure 2d, where the total measured boundary length is divided by the total scan area. This results in a quantitative parameter with respect to twin migration as a dominant plastic deformation mechanism [41], as well as indicating energy minimizing processes related to grain boundary energy. The fractional twin boundary length for h_f = 5 µm decreases from 0.94

to 0.30 μm^{-1}, for h_f = 10 μm from 0.63 to 0.16 μm^{-1}, and for h_f = 20 μm from 0.30 to 0.06 μm^{-1}. With respect to the fractional HAGB length evolution a reduction from 0.45 to 0.24 μm^{-1}, from 0.29 to 0.10 μm^{-1}, and from 0.17 to 0.05 μm^{-1} for h_f = 5, 10, and 20 μm was obtained, respectively.

The presented results in Figure 2d indicate a faster rate of interface energy minimization with increasing h_f. For h_f= 5μm the grain boundary length per unit area decreased to less than half of its initial value, while for h_f = 20 μm the HAGB was reduced by more than a factor of three. This leads to the conclusion that minimization of γ_i is proportional to h_f.

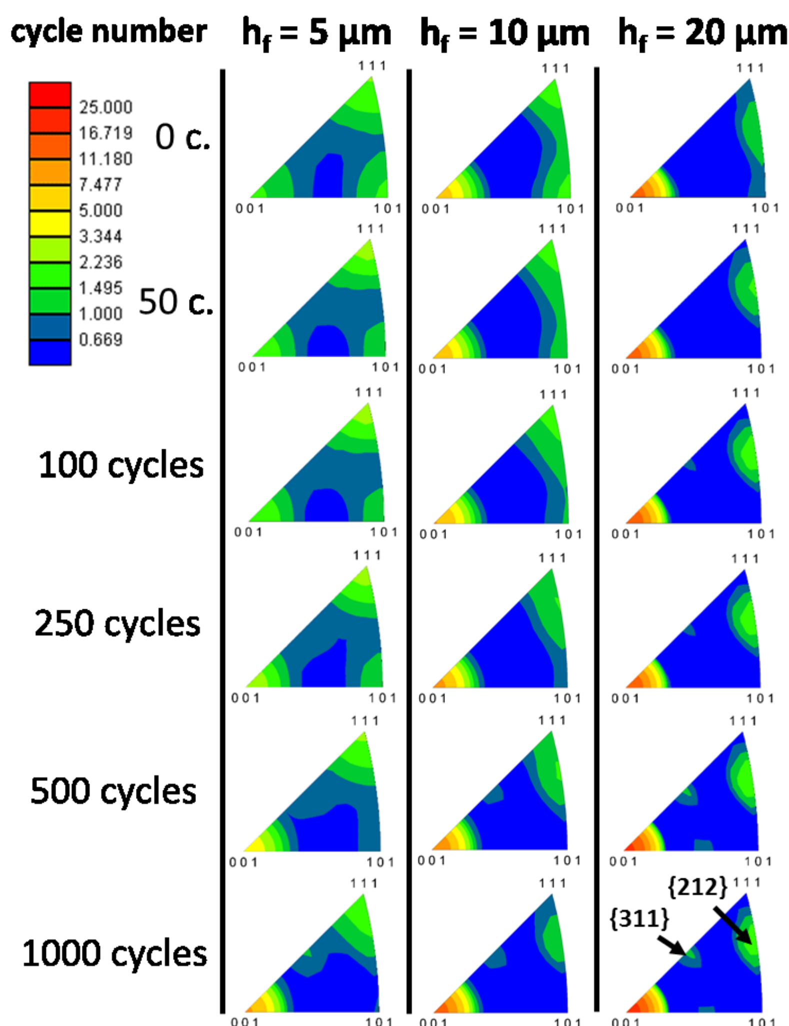

Figure 3: Inverse pole figures represent the texture evolution of the three different initial microstructures of the 5, 10 and 20 μm thick Cu films. (Colour online)

The texture evolution of the three films is presented in Figure 3 with inverse pole figures (IPF). The colour code indicates the likelihood of the appearance of certain crystal orientations compared to a random orientation (blue/dark blue color). From the initial texture it can be observed that with increasing film thickness the texture exhibits a gradual transition from a randomly oriented texture to a {100} dominated texture. During the cycling a texture increase of the {100} out-of-plane orientation, along with a slight increase of its {212} twin configuration, in all three film thicknesses occurs. The {110} plane orientation vanishes for all three thicknesses. After 1000 thermal cycles, only the {100} orientation with its corresponding {212}-oriented twin, a texture component close to the {311} orientation and the {111} out-of-plane orientation, is present where the fraction is significantly reduced with increasing film thickness. From Figure 3 it appears that the {311} orientation develops due to a constant grain rotation and will be discussed in the next section.

Local microstructure evolution

Many studies have already presented detailed work on the thermo-mechanical behaviour of thinner films ($\leq$ 5 μm) [11, 13, 17, 28]. Here, microstructural observations are presented for the 20 μm thick film to emphasize the effect of film thickness, grain size and texture on the thermo-mechanical behaviour.

In Figure 4 the microstructural changes of the first 50 thermal cycles are presented for the same area using EBSD and AFM. The initial microstructure of the 20 μm film (Figure 4a-c) consists of many twinned grains (white lines indicate HAGB, black lines indicate primary twins), where a significant portion has a {100} orientation in the normal direction (ND) to the film plane (Figure 4a), but different in-plane orientations, as shown by the EBSD image showing the transversal direction (Figure 4b). Most of the grains exhibit a pronounced grain boundaries, which can be seen in the AFM image (Figure 4c). After 50 cycles significant changes in the microstructure can be seen by comparing the initial (Figure 4a, b) to the after cycling grain orientation maps (Figure 4d, e). A group of grains with different out-of-plane and in-plane orientations collectively deform by shear, resulting in a crystallographic segment with an approximate {321} out-of-plane orientation, indicated by Feature 1.

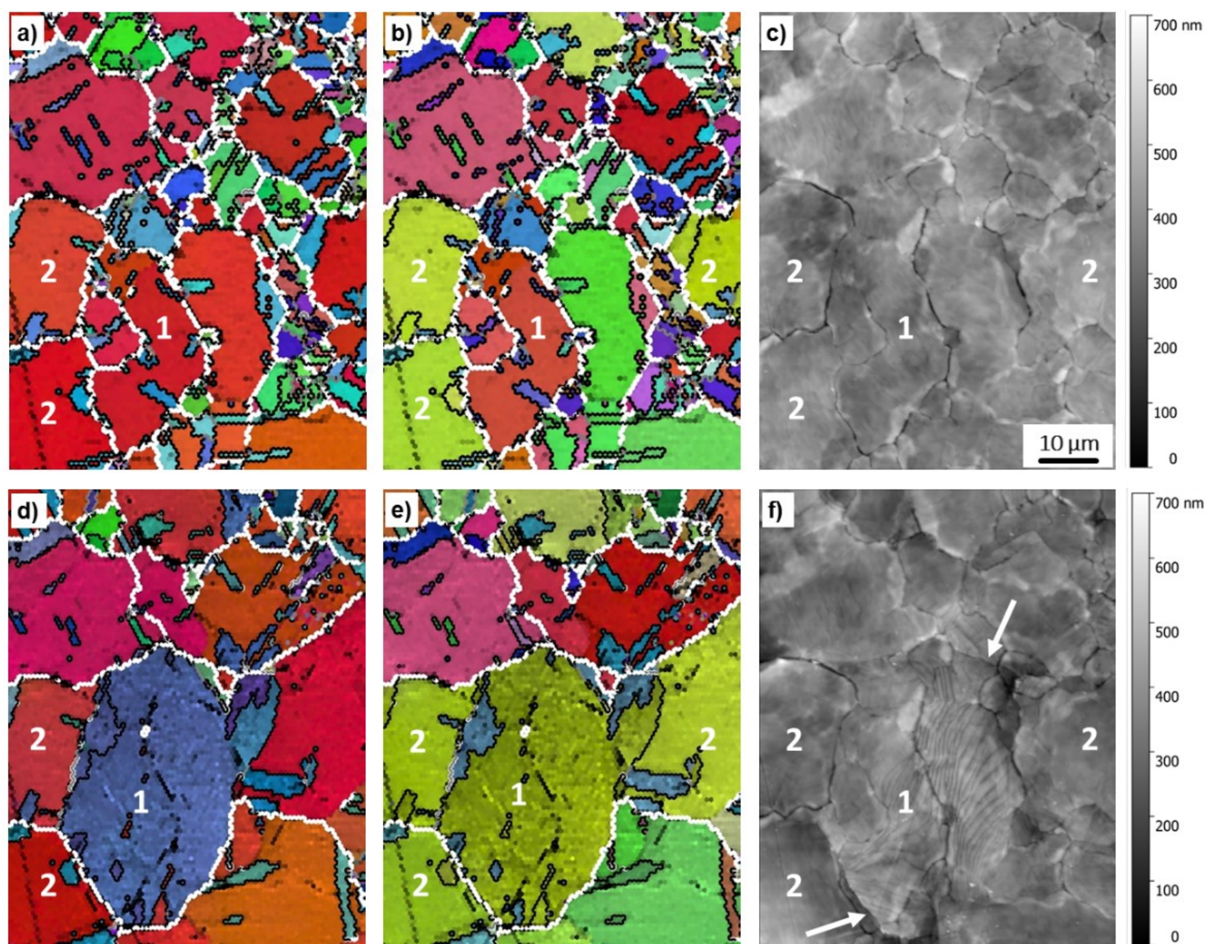

Figure 4: Local microstructural changes for h_f= 20 µm, where the same area before (a-c) and after 50 thermal cycles (d-f) is presented. The crystallographic information with respect to the out-of-plane (a,d) and in-plane (b,e) direction is combined with the topographical information (c,f). Scale bar is valid for all figure parts. (Colour online)

The {321} oriented segment is in a primary twin boundary relation with other growing grains (Feature 2). After 50 cycles the newly formed twin segment (Figure 4 e-f, Feature 1) and the surrounding grains have the same in-plane orientation (Figure 4e). From the Figure 4f it can be observed that the initial grain boundaries are still present and severe shear of the grains occurred on different glide planes. Furthermore, new HAGB interfaces are observed (Figure 4f, white arrows). These findings suggest that grains in thicker films first reorient in order to compensate for the in-plane misorientation when a biaxial strain is applied and a collective reorientation of the former small grains occurs.

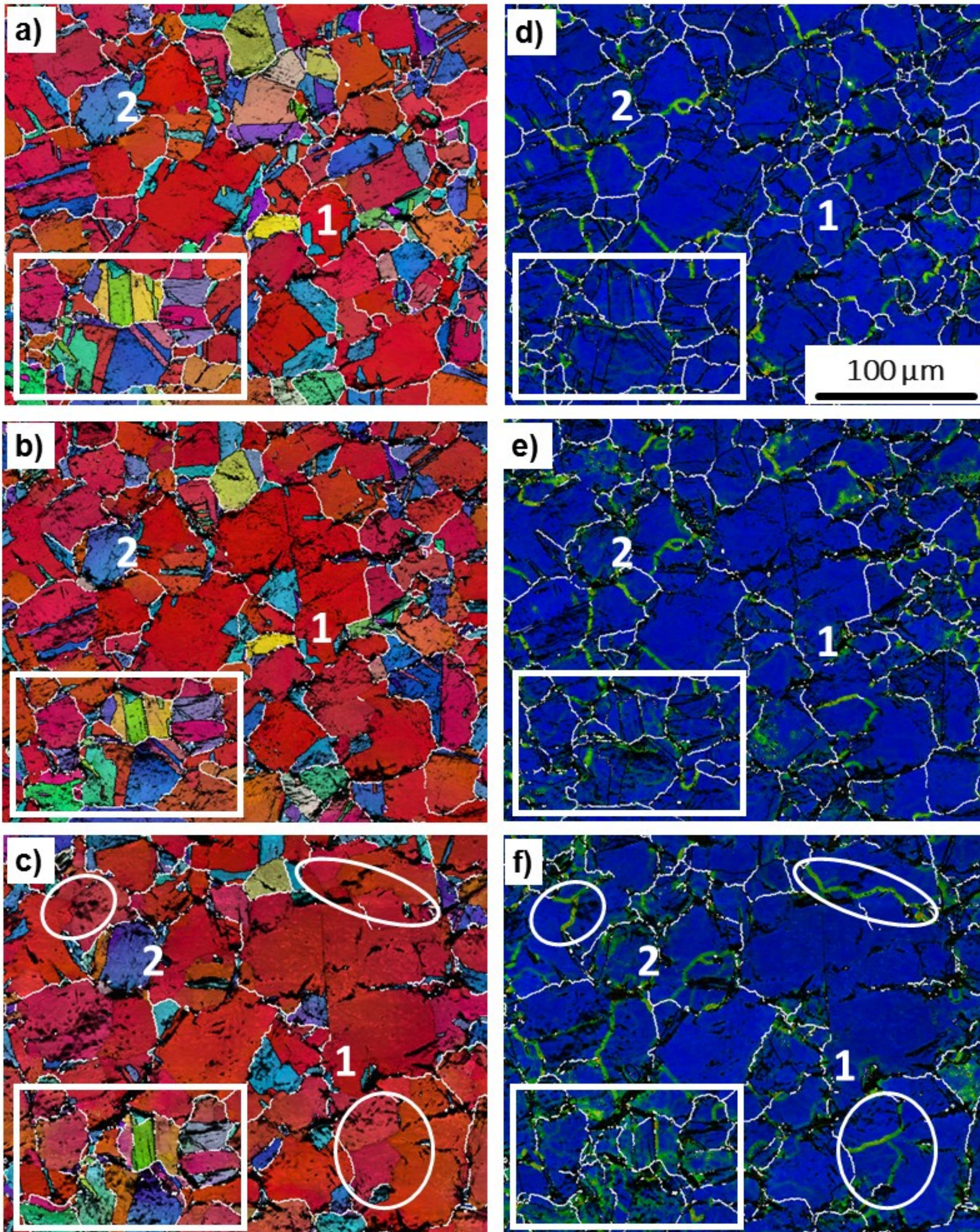

Figure 5: Microstructural evolution of $h_f = 20$ µm illustrated by site specific grain orientation maps with IQ analysis between 250, 500 and 1000 cycles (a, b and c). The corresponding kernel average misorientation plots are presented (d-f). Scale bar is valid for all micrographs. (Colour online)

Figure 5 presents the microstructural changes for the $h_f = 20$ µm after 250, 500 and 1000 cycles (Figure 5 a-c). The microstructure of the selected area after the first 250 thermal cycles (Figure 5a, d) is composed of a majority of large {100} out-of-plane oriented grains with their corresponding {212} oriented primary twins and smaller twinned grains with different orientations (see highlighted rectangular section). Continued

thermal-mechanical cycling resulted in a pronounced growth of {100}-oriented grains, causing large areas with the same crystallographic orientation (see Feature 1). The formation of crystal segments with low angle grain boundaries (LAGB) in the large {100}-oriented grains can be observed during the cycling. Additionally, kernel average misorientation [42, 43] images are provided (Figure 5 d-f). A local misorientation value of the kernel is assigned (2nd neighbour) with respect to the center of the kernel to indicate sub-grain structures, such as low angle grain boundaries (LAGB, $\theta \leq 15°$) and plastic strain accumulation. The substructures, indicated by sharp green lines in the kernel average misorientation plots (Figure 5d-f) exhibit local misorientation angles of about six to twelve degrees. The circular features (Figure 5c, f) highlight the geometric substructures with approximate angles of about 90, 135 and 150 degrees between the straight LAGB domains. As seen from the grain orientation maps and kernel average misorientation plots, Feature 2 does not change size despite the plastic strain accumulation during cycling. Grains and twins with an orientation other than {100} either significantly shrink or accumulate plastic strain during the thermal cycling. Such behaviour can be seen in the highlighted rectangular section where grains do not greatly change in size but accumulate plastic strain during cycling. This is qualitatively indicated by the colour changes (Figure 5c) and the formation of a dense network of local misorientations (Figure 5d-f) in this area.

The experimental results indicate that the mechanisms behind grain growth during thermo-mechanical cycling are strongly influenced by h_f and texture. The pronounced grain growth in the early stage (Figure 4) was accomplished by collective shearing across the initial grains where it appears that the in-plane crystal orientation plays an important role. Experimental evidence is found in Figure 5, where the same twin (marked as Feature 2) is preserved throughout the cycling experiment. Grain growth of the {100} texture component in the 20 µm thick film follows the development of defined grain sub-structures (circular features), while grains with other orientations have severe plastic strain accumulation. In a recent work, the authors found similar behaviour for a 5 µm thick Cu film cycled in an infrared furnace where such geometric substructures formed gradually from an initial misorientation gradient in an approximately{100}-oriented grain [15]. The {100}-specific sub-grain structures were also previously observed by others in thermally cycled submicron thick copper lines, where angles of 5-

10° misorientation developed [21]. TEM studies of mechanically fatigued copper films revealed that a grain size/film thickness dependent dislocation structure develops in {100} out-of-plane oriented grains [10, 16]. Geometric arrays of {100}-aligned dislocation walls form in larger grains due to the promotion of dislocation activity in larger crystals. Studies on the characterization of dipolar dislocation walls could be used to explain the geometry of the incurred LAGB substructures in the abnormally large <100> oriented grain. The authors [44, 45] conclude that fatigue experiments in fcc metals, especially in crystals with a <100> crystal orientation suitable for multiple slip, would result in {100} and {110} walls. The model of combined (double) slip on the primary {111}/<110> glide systems, where Burgers vectors of the slip systems add to a Burgers vector parallel or perpendicular to the dislocation walls, was used to explain the resulting arrays of edge dislocations [44].

Microstructural damage analysis

To qualitatively assess the thermo-mechanical fatigue damage, Figure 6 presents representative areas after 1000 cycles of h_f = 5-20 µm using SEM and EBSD micrographs. For the 5 µm thick Cu film (Figure 6 a, b) surface damage is present over the entire area. For example, pronounced glide bands formed within grains at twin boundary interfaces (Feature 1) and severe roughening can be observed at HAGB (white lines) where hillock-like formations (Feature 2) at the grain boundaries are observed. The area in the circular marking is an example of extrusions/intrusions within individual grains.

With increasing film thickness the surface damage changes. In the presented area for h_f = 10 µm (Figure 6 c, d), large {100}-oriented grains exhibit pronounced shearing (slip) at their twin boundary interfaces after 1000 thermal cycles (Feature 3). Damage evolution differs depending on the grain orientation. For example at Feature 4, the approximately {212}-oriented twin segment has severe surface roughening along preferred slip planes (Figure 6c), while in the {100}-oriented twin counterparts the same fatigue features are not seen. Grains with an orientation other than {100} exhibited severe shearing at their twin planes and have a rougher appearing surface (Feature 5).

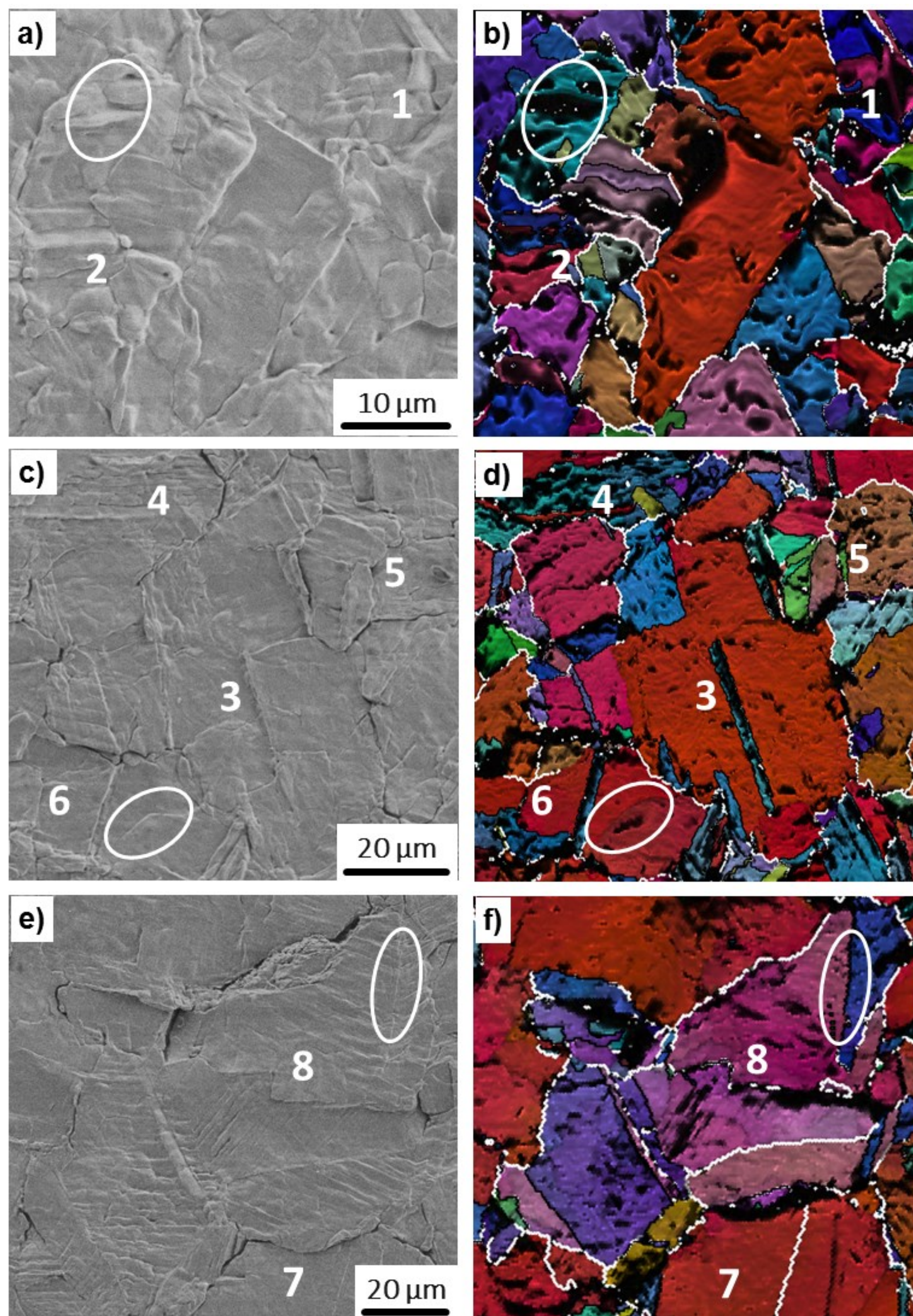

Figure 6: Qualitative film surface damage analysis of h_f= 5µm (a,b), h_f= 10 µm (c,d) and h_f= 20µm (e,f) using site-specific SEM and grain orientation maps with IQ analysis after 1000 thermal cycles. (Colour online)

Plasticity in the soft oriented {100} grains appears to accumulate differently than in other oriented crystal segments. The colour gradients in Feature 6 (Figure 6d) indicate a gradual change of orientation. The observation that a gradual change in orientation across {100}-grains (constant tilt with respect to ND) occurs as a result of stress field minimizing LAGB [46]. This suggests that dislocation reactions are involved in the crystal rotation that are energetically preferred compared to those that would result in

glide steps at the film surface. In contrast to grains with orientations other than {100}, there was no dominant slip system activated that would lead to the formation of one specific slip pattern at the film surface.

For the Cu film thickness h_f= 20 µm it can be seen that thermo-mechanical fatigue damage strongly depends on the out-of-plane orientation. Feature 7 (Figure 6e, f) shows that no significant surface damage is present in the {100}-oriented grains. Grains with crystal orientations other than {100} show severe surface roughening in the form of slip traces (Feature 8). The approximate {311} oriented grain and its twin show pronounced slip steps at the film surface, demonstrated by the circular marking at a twin boundary and indicates the mirror-like arrangement of the slip traces between the two crystallographic orientations. As already seen in Figure 3 the ~{311} out-of-plane orientation appears to develop due to a constant grain rotation, which is experimentally observed by Feature 8 in Figure 6 where misorientation gradients are present across the twinned grain. This reorientation seems to also be strain energy driven as well, as reported by Zhang et al. on annealed Cu films on Si substrates [47].

Another study dealing with orientation specific damage analysis, attributed the higher damage resistance of the {100} oriented grains to the lower biaxial stresses ($\sigma_{111}/\sigma_{100} = 2.26$) as well as to the lower fraction of applied shear stress, τ, on a particular slip plane (eight equally active glide systems in <100> compared to six in <111>) [20]. Considering that after 1000 cycles $d >> h_f$ for thicker Cu films (h_f = 10, 20µm), grain to grain stress interactions are negligible and a single crystal approximation can be used (Schmid´s law) [22]. For such a condition, Mönig et al. computed the corresponding resolved shear stresses for each orientation [21] where $\tau_{212}/\tau_{100} = 1.84$. The {212} twin segment has two glide systems with the highest resolved shear stress compared to eight for the {100} parent grain which is in agreement with observed roughening in those twin sections (Figure 6, Feature 4). The experimental stress-temperature response (Figure 1e) of the 20 µm thick film it gives further proof to the assumption that the corresponding shear stresses on the eight equally active glide systems are very low. By approximating that the measured film stress σ_{film} corresponds to σ_{100}, this would lead to a $\tau = S_{100}*\sigma_{100}$ of about -24 MPa and 14 MPa in the heating and cooling stages respectively.

The site specific damage investigation presented in Figure 6 emphasizes that surfaces damage decreases with increasing film thickness. This can be directly correlated to the large fraction of {100} oriented grains which appear to have a higher damage tolerance with respect to thermo-mechanical fatigue.

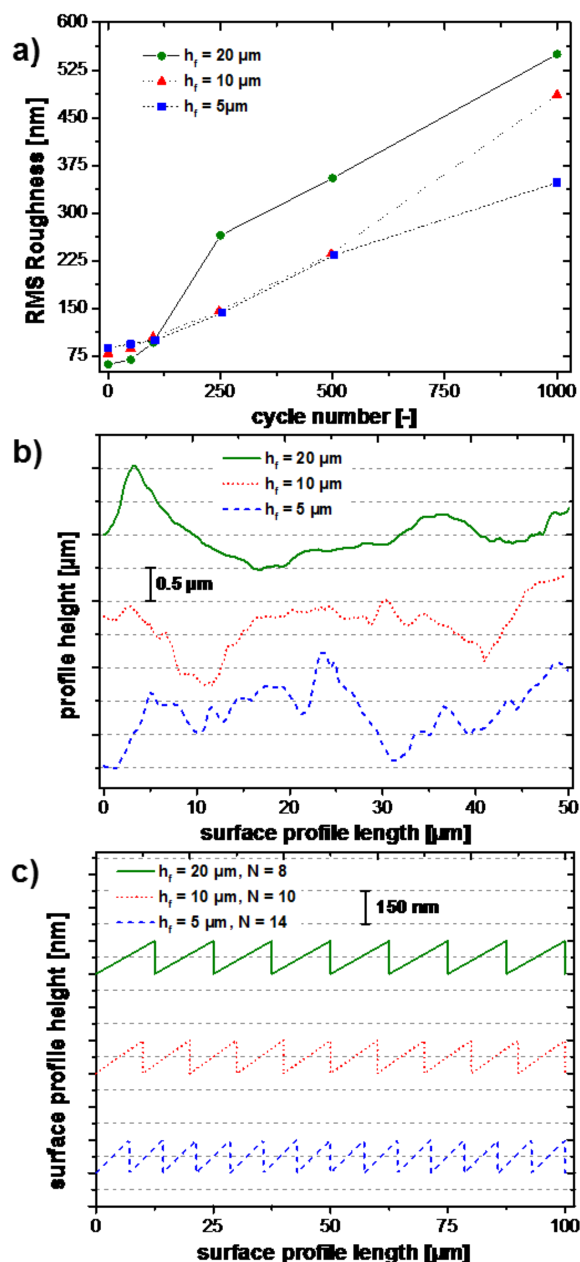

Figure 7: (a) RMS roughness evolution of the three film thicknesses as a function of cycle number. (b) Representative AFM profile sections after 1000 thermal cycles. (c) Reference surface roughness profiles using the determined mean surface length after 1000 cycles.

In Figure 7a the RMS roughness evolution is presented for the three thermally cycled Cu film thicknesses. The initially similar film roughness (88, 79 and 62 nm with

increasing h_f) evolves differently, where the RMS roughness was ranked with respect to the film thickness after 1000 cycles. This result may seem to contradict previous observations illustrated in Figure 6, where the surface roughness appeared to be inversely proportional on h_f. In Figure 7b this contradictive observation regarding the surface roughness can be explained the following way. The representative surface profiles for h_f = 5, 10 and 20 µm reveal that all film surfaces after 1000 cycles have a similar maximum vertical height amplitudes ($\Delta y \sim 1.5$µm), but the frequency of lateral surface roughness (which can be equated to surface damage) appears to increase with decreasing film thickness. This is due to the fact that R_{RMS} is considered as an amplitude parameter and is only affected by vertical height variations of the film surface. Furthermore, the quadratic dependency of data points accentuates greater height variations providing greater R_{RMS} values [48]. To show the influence of the increasing fraction of more damage tolerant {100} grains with respect to increasing film thickness, 15 AFM profiles were taken after 1000 thermal cycles from each film thickness. The surface profile lengths, extracted by the AFM processing software, were numerically processed by creating a polygonal path using the Pythagorean theorem between each pair of data points [49]. The resulting mean surface lengths were normalized with respect to a profile length of 100 µm. This results in a mean surface length of 102.26 ± 0.65 µm, 101.53 ± 0.56 µm and 101.22 ± 0.52 µm for h_f = 5, 10 and 20 µm, respectively. To visualize these seemingly similar lateral roughness parameters, a reference roughness function was defined and used in Fig 7c, where the obtained surface length $L_{(f)}$ is defined as:

$$L_{(f)} = \left[d + \sqrt{\left(\frac{100}{N}\right)^2 + d} \right] N \qquad (4)$$

with d as the chosen roughness height and N giving the number of roughness intervals. This enables the direct comparison of accumulated surface damage with respect to the film thickness. From the graph it becomes evident that the Cu film with h_f = 5 µm has the highest accumulated roughness. For the same reference profile length of 100 µm with a chosen roughness height of d = 150 nm, 15 intervals are required to obtain the experimental mean surface length. In comparison, the thicker films h_f = 10 and 20 µm result in N = 10 and 8, respectively, indicating significantly less surface damage with

increasing film thickness. The approach of numerically integrating several representative profile lengths over different AFM scans led to a statistical parameter with a physical meaning. By using a chosen reference function and displaying the accumulated damage with similar maximum height differences (see Figure 7b), allows a direct qualitative and quantitative comparison of the film surface roughening (damage) of the three thermo-mechanically cycled film thicknesses (Figure 7c). The experimental observations from Figure 6 are confirmed, emphasizing that fatigue damage is inversely proportional to h_f for thick Cu films ($h_f \geq 5$µm).

Conclusions and Summary

In this study, the thermo-mechanical behaviour of thick Cu films with thicknesses between 5 to 20 µm was presented. Initial microstructural characteristics of texture and grain size changed as a function of film thickness during 1000 thermo-mechanical cycles. The microstructural evolution during cycling and the corresponding surface damage is significantly different from similar studies on thin Cu films (< 5 µm). The following conclusions can be drawn:

- Initial microstructural properties indicate that electrodeposited Cu films a texture transitions towards the {100} out-of-plane orientation at film thicknesses ≥ 5 µm.

- Pronounced growth of the {100} out-of-plane orientated grains upon thermal cycling was observed. The grain growth of the {100} texture component in thicker films (10 µm and 20 µm) agrees with a gradual formation of dislocation sub-structures.

- The thermo-mechanical fatigue damage assessment after thermal cycling (Figure 6) revealed a transition of an orientation independent surface damage (5 µm) to an orientation dependent damage (roughening) for thicker films (10 µm and 20µm). A higher damage tolerance was found for the {100} oriented grains because these grains have a lower surface roughness.

- The accumulated surface roughness, displayed by the reference function (Figure 7) indicates that fatigue damage has a ~ $1/h_f$ dependency for thicker films (≥ 5 µm) and is different compared to thin Cu film counterparts (≤ 5 µm).

4 Acknowledgement

The work was performed in the project EPPL, financially supported by grants from Austria, Germany, The Netherlands, France, Italy, Portugal, and the ENIAC Joint Undertaking (ENIAC JU Grant Agreement no. 325608). This project is co-funded within the programme "Forschung, Innovation und Technologie für Informationstechnologie" by the Austrian Ministry for Transport, Innovation and Technology.

5 References

[1] G.E. Moore, Electronics Cramming More Components onto Integrated Circuits 38(8) (1965) 114-117.

[2] M. Nelhiebel, R. Illing, C. Schreiber, S. Wöhlert, S. Lanzerstorfer, M. Ladurner, C. Kadow, S. Decker, D. Dibra, H. Unterwalcher, M. Rogalli, W. Robl, T. Herzig, M. Poschgan, M. Inselsbacher, M. Glavanovics, S. Fraissé, *Microelectron Reliab*, A reliable technology concept for active power cycling to extreme temperatures 51(9–11) (2011) 1927-1932.

[3] P.A. Flinn, D.S. Gardner, W.D. Nix, *IEEE T Electron Dev*, Measurement and interpretation of stress in aluminum-based metallization as a function of thermal history 34(3) (1987) 689-699.

[4] M. Nelhiebel, R. Illing, T. Detzel, S. Wöhlert, B. Auer, S. Lanzerstorfer, M. Rogalli, W. Robl, S. Decker, J. Fugger, M. Ladurner, *Microelectron Reliab*, Effective and reliable heat management for power devices exposed to cyclic short overload pulses 53(9–11) (2013) 1745-1749.

[5] W. Robl, M. Melzl, B. Weidgans, R. Hofmann, M. Stecher, *IEEE T Semiconduct M*, Last Metal Copper Metallization for Power Devices 21(3) (2008) 358-362.

[6] X. Zhou, H. Wadley, *Acta Mater*, Twin formation during the atomic deposition of copper 47(3) (1999) 1063-1078.

[7] A. Wikström, M. Nygårds, *Acta Mater*, Anisotropy and texture in thin copper films—an elasto-plastic analysis 50(4) (2002) 857-870.

[8] C. Thompson, R. Carel, Grain growth and texture evolution in thin films, *Mater Sci Forum*, 1996, pp. 83-98.

[9] P. Sonnweber-Ribic, P. Gruber, G. Dehm, E. Arzt, *Acta Mater*, Texture transition in Cu thin films: Electron backscatter diffraction vs. X-ray diffraction 54(15) (2006) 3863-3870.

[10] G.P. Zhang, C.A. Volkert, R. Schwaiger, P. Wellner, E. Arzt, O. Kraft, *Acta Mater*, Length-scale-controlled fatigue mechanisms in thin copper films 54(11) (2006) 3127-3139.

[11] O. Kraft, P. Wellner, M. Hommel, R. Schwaiger, E. Arzt, *Z Metallkd*, Fatigue behavior of polycrystalline thin copper films 93(5) (2002) 392-400.

[12] R. Mönig, R.R. Keller, C.A. Volkert, *Rev Sci Instrum*,Thermal fatigue testing of thin metal films 75(11) (2004) 4997-5004.

[13] W. Heinz, W. Robl, G. Dehm, *Microelectron Eng*, Influence of initial microstructure on thermomechanical fatigue behavior of Cu films on substrates 137 (2015) 5-10.

[14] O. Kraft, R. Schwaiger, P. Wellner, *Mat Sci Eng A-Struct*, Fatigue in thin films: lifetime and damage formation 319–321 (2001) 919-923.

[15] S. Bigl, S. Wurster, M.J. Cordill, D. Kiener, *Thin Solid Films*, Advanced characterisation of thermo-mechanical fatigue mechanisms of different copper film systems for wafer metallizations 612 (2016) 153-164.

[16] G.P. Zhang, R. Schwaiger, C.A. Volkert, O. Kraft, *Phil Mag Lett*, Effect of film thickness and grain size on fatigue-induced dislocation structures in Cu thin films 83(8) (2003) 477-483.

[17] R. Schwaiger, G. Dehm, O. Kraft, *Philos Mag A*, Cyclic deformation of polycrystalline Cu films 83(6) (2003) 693-710.

[18] M. Hommel, O. Kraft, E. Arzt, *J Mater Res*, A new method to study cyclic deformation of thin films in tension and compression 14(06) (1999) 2373-2376.

[19] G.P. Zhang, C.A. Volkert, R. Schwaiger, E. Arzt, O. Kraft, *J Mater Res*, Damage Behavior of 200-nm Thin Copper Films Under Cyclic Loading 20(01) (2005) 201-207.

[20] M. Aicheler, S. Sgobba, G. Arnau-Izquierdo, M. Taborelli, S. Calatroni, H. Neupert, W. Wuensch, *Int J Fatigue*, Evolution of surface topography in dependence on the grain orientation during surface thermal fatigue of polycrystalline copper 33(3) (2011) 396-402.

[21] R. Mönig, Dissertation, Max Plank Institute Thermal fatigue of Cu thin films (2005).

[22] S.P. Baker, A. Kretschmann, E. Arzt, *Acta Mater*, Thermomechanical behavior of different texture components in Cu thin films 49(12) (2001) 2145-2160.

[23] Y. Akiniwa, T. Suzuki, K. Tanaka, Evaluation of deformation behavior in Cu thin film under tensile and fatigue loading by X-ray method, *Mater Sci Forum*, 2006, pp. 807-812.

[24] S. Bigl, S. Wurster, M.J. Cordill, D. Kiener, *BHM*, Site Specific Microstructural Evolution of Thermo-mechanically Fatigued Copper Films 5(160) (2015) 235-239.

[25] A. Wimmer, M. Smolka, W. Heinz, T. Detzel, W. Robl, C. Motz, V. Eyert, E. Wimmer, F. Jahnel, R. Treichler, *Mat Sci Eng A-Struct*, Temperature dependent transition of intragranular plastic to intergranular brittle failure in electrodeposited Cu micro-tensile samples 618 (2014) 398-405.

[26] S. Bigl, T. Schöberl, S. Wurster, M.J. Cordill, D. Kiener, *Surf Coat Tech*. Correlative microstructure and topography informed nanoindentation of copper films 308 (2016) 404-413.

[27] S. Bigl, W. Heinz, M. Kahn, H. Schoenherr, M.J. Cordill, J*OM-J Min Met Mat S*, High-Temperature Characterization of Silicon Dioxide Films with Wafer Curvature 67(12) (2015) 2902-2907.

[28] S. Wurster, S. Bigl, M.J. Cordill, D. Kiener, *Microelectron Eng*, Accelerated thermo-mechanical fatigue of copper metallizations studied by pulsed laser heating (2016).

[29] T.A. Hahn, J Appl Phys, Thermal Expansion of Copper from 20 to 800 K—Standard Reference Material 736 41(13) (1970) 5096-5101.

[30] C. Swenson, *J Phys Chem Ref Data*, Recommended values for the thermal expansivity of silicon from 0 to 1000 K 12(2) (1983) 179-182.

[31] K. Chavez, D. Hess, *J Electrochem Soc*, A novel method of etching copper oxide using acetic acid 148(11) (2001) G640-G643.

[32] D. Nečas, P. Klapetek, *Cent Eur J Phys*, Gwyddion: an open-source software for SPM data analysis 10(1) (2012) 181-188.

[33] P. Sonnweber-Ribic, P.A. Gruber, G. Dehm, H.P. Strunk, E. Arzt, *Acta Mater*, Kinetics and driving forces of abnormal grain growth in thin Cu films 60(5) (2012) 2397-2406.

[34] H. Ledbetter, E. Naimon, *J Phys Chem Ref Data*, Elastic properties of metals and alloys. II. Copper 3(4) (1974) 897-935.

[35] J. Rösler, H. Harders, M. Baeker, Mechanical behaviour of engineering materials: metals, ceramics, polymers, and composites, Springer Science & Business Media2007.

[36] E.M. Zielinski, R.P. Vinci, J.C. Bravman, *J Appl Phys*, Effects of barrier layer and annealing on abnormal grain growth in copper thin films 76(8) (1994) 4516-4523.

[37] P.A. Flinn, *J Mater Res*, Measurement and interpretation of stress in copper films as a function of thermal history 6(07) (1991) 1498-1501.

[38] D. Weiss, Dissertation, Deformation mechanisms in pure and alloyed copper films Deformation mechanisms in pure and alloyed copper films (2000).

[39] A.C.F. Cocks, M.F. Ashby, *Prog Mater Sci*, On creep fracture by void growth 27(3) (1982) 189-244.

[40] C.V. Thompson, R. Carel, *Mat Sci Eng B-Solid*,Texture development in polycrystalline thin films 32(3) (1995) 211-219.

[41] D. Field, B. True, T. Lillo, J. Flinn, *Mat Sci Eng A-Struct*, Observation of twin boundary migration in copper during deformation 372(1) (2004) 173-179.

[42] M. Calcagnotto, D. Ponge, E. Demir, D. Raabe, *Mat Sci Eng A-Struct*, Orientation gradients and geometrically necessary dislocations in ultrafine grained dual-phase steels studied by 2D and 3D EBSD 527(10) (2010) 2738-2746.

[43] S.I. Wright, M.M. Nowell, D.P. Field, *Microsc Microanal*, A review of strain analysis using electron backscatter diffraction 17(03) (2011) 316-329.

[44] P. Charsley, D. Kuhlmann-Wilsdorf, *Philos Mag A*,Configurations of {100} dislocation walls formed during fatigue 44(6) (1981) 1351-1361.

[45] M. Saxlová, J. Kratochvíl, *Mat Sci Eng A-Struct*, A theory of dipolar dislocation wall structures 188(1-2) (1994) 69-79.

[46] W. Read, W. Shockley, *Phys Rev A*, Dislocation models of crystal grain boundaries 78(3) (1950) 275.

[47] J.-M. Zhang, K.-W. Xu, V. Ji, *Appl Surf Sci*, Competition between surface and strain energy during grain growth in free-standing and attached Ag and Cu films on Si substrates 187(1–2) (2002) 60-67.

[48] E.S. Gadelmawla, M.M. Koura, T.M.A. Maksoud, I.M. Elewa, H.H. Soliman, *J Mater Process Tech*, Roughness parameters 123(1) (2002) 133-145.

[49] J. Ahlberg, E. Nilson, J. Walsh, *Math Sci Eng*, New York: Academic Press, 1967 The theory of splines and their applications (1967).

IX Publication F

Limits of Stoney's equation: substrate influenced thermo-mechanical fatigue of copper metallizations

Stephan Bigl, Stefan Wurster, Megan J. Cordill, Daniel Kiener

Thin Solid Films (2017); submitted

Abstract:

Rapid progress in the reduction of substrate thickness for silicon-based microelectronics leads to a significant reduction of the device bending stiffness and the need to address its implication on thermo-mechanical fatigue behaviour of metallization layers. Experimental results on 5 µm thick Cu films reveal a strong substrate thickness dependent microstructural evolution. We show that for substrates with h_s= 323 and 220 µm the Cu microstructure exhibits accelerated grain growth and surface roughening. Moreover, curvature-strain data indicates that Stoney´s simplified curvature-stress relation is not valid for thin substrates with regard to the expected strains, but can be addressed using more sophisticated plate bending theories.

1 Introduction

Thermo-mechanical fatigue of metallic thin films has been one of the key concerns in microelectronics during product life cycle. The material damage and subsequent failure regarding functionality is often associated with film cracking, severe surface roughening and void formation in the film interior. The driving force behind such microstructural changes is always connected to the evolving stresses in the film material. Stresses arise as a consequence of the substrate constraint and the different coefficients of thermal expansion (CTE) between film and substrate. The cornerstone of experimental evaluation of film stresses is performed with the famous Stoney equation [1]. Although many authors have developed refined calculations for substrate bending [2-6], Stoney´s equation has been used unchanged for more than a century. The arising biaxial film stress, σ_f, is derived by the simple expression

$$\sigma_f = \frac{E_s\, h_s^2\, \kappa}{6(1-\upsilon_s)\, h_f}, \tag{1}$$

where h_s, E_s and υ_s are the thickness, elastic modulus and Poisson’s ratio of the substrate, h_f the film thickness, and κ denotes the film/substrate curvature (inverse of radius). Since biaxial film stresses develop as a consequence of the thermal mismatch strain, ε_m,

$$\varepsilon_m \cong (\alpha_s - \alpha_f)\Delta T, \tag{2}$$

which is an invariant bound by the different CTE of the substrate and film, α_s and α_f, determination of stresses is only connected to the variation of the film/substrate curvature .

In other words, for the same σ_f the corresponding curvature is proportional to $1/h_s^2$ and h_f, and scales with the elastic properties of the substrate. To guarantee validity, equation (1) is based on the main assumption that h_f is much less than h_s [7]. Thereby, the criterion, $h^* = h_f/h_s$ is not strictly defined, but rather arbitrarily chosen (often set to h*= 0.01, see [6]). In modern microelectronics increasing product performance requires thinner and thinner substrates to decrease the vertical resistance and device volume, while keeping the metallization thicknesses similar [8, 9]. In literature, numerous studies report about the effect of film thickness on microstructural changes [10-12], but experimental work dealing with the influence of substrate thickness is very limited. Few

studies have shown that as a consequence to the increase of h^*, large non-linear deformations and bifurcation ($\kappa_x \neq \kappa_y$) of the substrate curvature can occur due to deposited films [13, 14]. This raises the question in which range Stoney's approximation is still valid with regard to cyclic thermal fatigue testing. Therefore, in the present study, the influence of substrate thickness is shown by thermally cycling identical 5 µm thick Cu films on silicon substrates with different thicknesses.

2 Materials and Experimental

Copper films with h_f = 5 µm were electrodeposited using a Cu electrolyte on 725 µm thick (100)-oriented silicon wafers. Afterwards, samples were annealed for 30 min in inert/reducing atmosphere at 400°C. For detailed information regarding the used copper film and its microstructure see references [15, 16], where the film used here was denoted as Film A. To achieve different substrate thicknesses, sample pieces of 5x10mm were cut, mounted into sample holders, and wet-ground with a semi-automated lab tool (Struers TegraPol, Struers ApS, Ballerup, Denmark). This process enabled specimens with h_s down to ~ 200 µm. Below that thickness, sample integrity (e.g. substrate cracking) becomes a major concern. For thermal cycling and subsequent microstructural analysis samples with h_s of 725, 541, 323 and 220 µm resulting in h^* of 0.007, 0.009, 0.015 and 0.023, respectively, were used. Those samples were thermo-mechanically cycled in an infrared furnace between 170°C and 400°C in formic gas atmosphere. To study the effect of varying substrate thickness on the thermo-mechanical behaviour of Cu films a site specific microstructural tracking technique was applied throughout the thermal cycling process [17]. Using electron back scatter diffraction (EBSD) in combination with atomic force microscopy (AFM) the microstructural and topographical evolution of a specific marked film surface area was studied. Furthermore, scanning electron microscope (SEM) images and focused ion beam (FIB) film cross-section were used to substantiate experimental evidence. To guarantee an oxide–free film surface, specimens were subjected to 100 vol% acetic acid at 35-40 °C for ~ 3 min. This enables the selective removal of any copper oxide and does not affect the actual Cu microstructure [18]. Experimental determination of the substrate curvature evolution was performed with a custom built wafer curvature set up with a multiple optical beam sensor, kSA MOS (k-Space Associates, Inc. Dexter, 48130 USA) and heating rate of 10

°C/min. Experimental details regarding temperature calibration, settings of the used instruments and its software packages can be found in [17, 19, 20].

3 Results

To quantitatively assess the effect of decreasing h_s with respect to the cyclic thermo-mechanical behaviour of the 5 µm thick Cu film, Table 1 presents the grain size (including twin boundaries) and standard deviation determined by EBSD for 0, 100 and 500 thermal cycles. For h_s = 725 and 541 µm an almost identical grain size evolution is present, where marginal grain growth during thermo-mechanical loading occurs. Below that the 541 µm substrate thickness, significant grain growth could be observed. For h_s = 323 µm, the grain size increased up to 4.3 ± 1.3 µm after 500 cycles, while for h_s = 220 µm the average grain size was increasing by a factor of two after 500 cycles. Figure 1 provides an overview of local microstructural changes for h_s = 541, 323 and 220µm. The inverse pole figure (IPF) images with overlaid image quality (IQ) in normal direction (ND) document the grain growth with respect to cycle number, where white lines indicate high angle grain boundaries (HAGB, ≥ 15°) and thin black lines primary twins (misorientation = 60°). For the Cu film on the thick substrate, h_s = 541 µm marginal microstructural changes can be observed during the cycling with respect to the initial stage. For instance, the ~ //{212} oriented parent/twin grain highlighted by a circle showed no essential plasticity during cycling, in particular no twin boundary migration as this controls grain growth in these films on standard 725 µm thick substrates [19]. On the contrary, the two thinner substrates (h_s = 323 and 220 µm) reveal grain growth during the thermo-mechanical loading in combination with noticeable twin boundary migration as a plastic deformation mechanism. This is highlighted for h_s=220 µm in the squared section. The ~ {110}-oriented twinned grains shows distinct grain growth via HAGB migration as well as detwinning during cycling.

Table 1: Grain size evolution of the Cu film with four different substrate thicknesses during cycling.

Cycle Number [-]	**Grain size (including twins) [µm]**			
	h_s = 725 µm	**h_s = 541 µm**	**h_s = 323 µm**	**h_s = 220 µm**
0	2.4 ± 0.8	2.3 ± 0.7	2.5 ± 0.7	2.4 ± 0.8
100	2.7 ± 0.9	2.7 ± 0.8	3.6 ± 1.1	3.8 ± 1.2
500	2.8 ± 0.9	3.0 ± 1.0	4.3 ± 1.3	5.1 ± 1.6

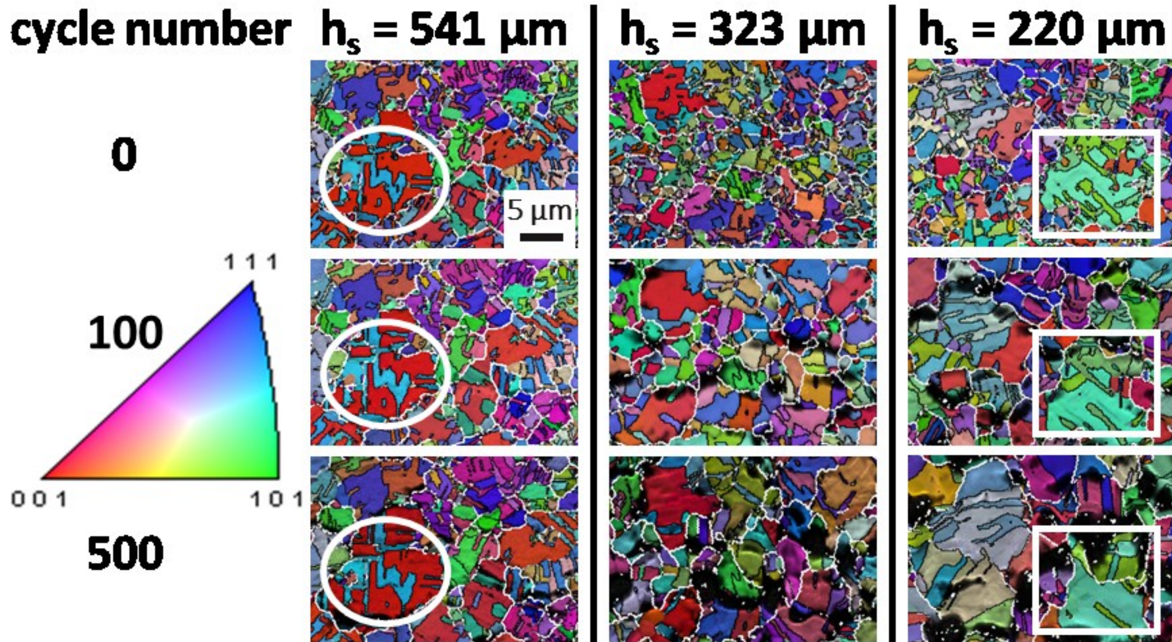

Figure 1: Microstructural evolution of 5 µm Cu films on silicon substrates with different thicknesses. The IPF-IQ images display the changes with respect to the cycling stage of 0, 100 and 500 cycles. Scale bar is valid for all EBSD images.

A comparable trend was found when evaluating the roughness. Figure 2a illustrates the root mean squared (RMS) roughness evolution of the film surface with regard to a decreasing h_s. An almost identical roughness evolution for h_s= 725 and 541 µm is observed, in accordance with the grain size evolution in Table 1. Both films start with an initially very flat surface of about ~ 20 nm RMS roughness, which increased up to ~110 nm after 1000 cycles. For h_s= 323 and 220 µm a significant increase was observed. After 750 cycles the RMS roughness of the Cu films on h_s= 323 and 220 µm was increased by a factor of ~ 3 and ~5 compared to that on h_s = 541 µm. The significant increase of surface roughening for thinner substrates was due to the formation of hillock-like features and voids on the surface (Figure 2b), as well as void formation at grain boundaries in the film interior (Figure 2c).

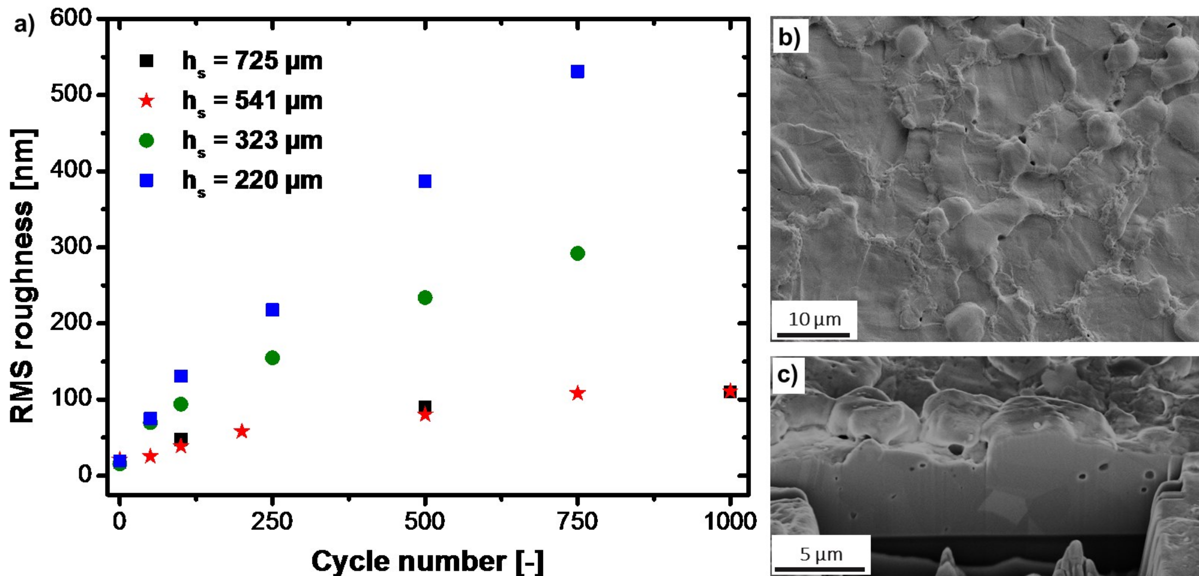

Figure 2: (a) RMS roughness evolution of a h_f = 5 µm Cu film on silicon substrates with different thicknesses (725, 541, 323 and 220 µm) as a function of cycle number. (b) SEM micrograph and (c) FIB cross section of a 5 µm film on h_s = 220 µm after 750 thermal cycles.

4 Discussion

The experimental findings show a significant substrate thickness dependency with regards to the thermo-mechanical fatigue behaviour. The h_s= 725 and 541 µm thick substrates show minimal grain growth (Table 1) and restricted surface roughening (Fig. 2a), therefore, confirming results from a previous study on 725 µm substrates (denoted as Film A in that work) [19]. However, a distinctively different thermal fatigue behaviour was observed for substrate thicknesses < 541 µm. From a phenomenological point of view it seems that at a certain h^*, a threshold strain energy was overcome to enable the observed HAGB migration and twin boundary migration. Since mismatch strain is only defined by the mismatch in CTE of the corresponding materials (see equation 2), thermal film stresses were supposedly the same in every cycled sample and, hence, cannot cause the different thermal fatigue behaviour.

In a study by Chu et al. dealing with the reformulation of the Stoney formula, the author points out that the original problem of bending a composite beam (or plate) due to thermal stress will always result in a net bending moment as long as there is an elastic bending curvature [21]. In other words: The composite plate curvature results in a bending stress configuration which is opposite in sign than the generated thermal stress.

The exact derivation not only points out the falsehood of Stoney´s simplified and arbitrarily chosen neutral axis position b, where $b = 2h_s/3$ [1], but lead to substantially different curvature-strain relation. For h^* smaller than 0.1, Stoney's formula would underestimate the corresponding bending curvature by a factor of ~ 2. (see Figure 6, [21]). Thereby, the curvature is related to

$$\frac{1}{R} = \frac{12\frac{M_f}{M_s}\frac{h_f}{h_s}}{h_s\left(1+6\frac{M_f}{M_s}\frac{h_f}{h_s}\right)}\varepsilon_m\,, \tag{3}$$

where M_s and M_f are the biaxial moduli of the substrate and film, respectively.

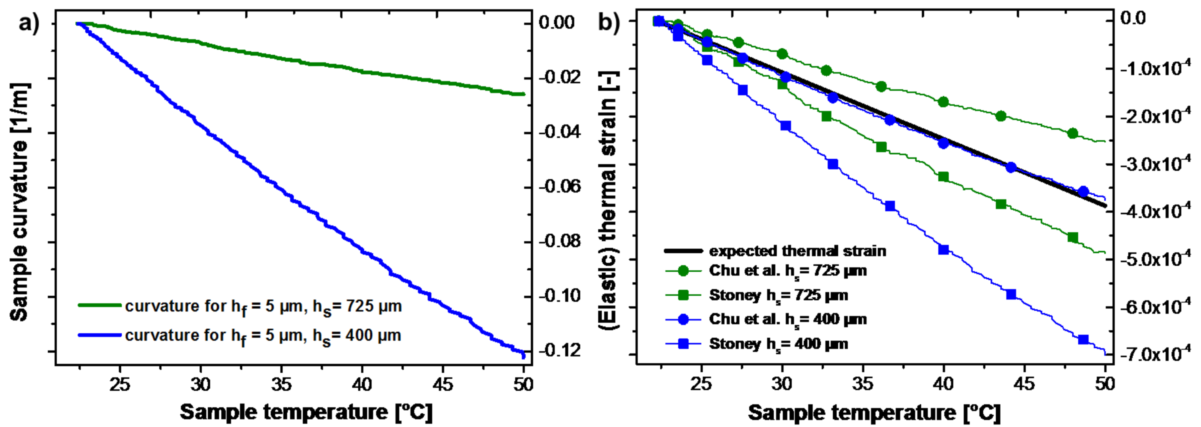

Figure 3: (a) Curvature evolution of a h_f= 5 µm Cu film on Si with h_s = 725 and 400 µm. (b) Comparison of thermal strain evolution calculated following Stoney (squares) and Chu (circles) with regards to the measured curvature.

To validate the predictions of the actual bending curvature using Stoney and Chu curvature-(film) strain relations, the curvature evolution due to thermal mismatch was measured for substrate thicknesses of h_s = 725 and 400 µm using substrates were processed using semiconductor industry tools to exclude preparation artefacts. Both wafers had the 5 µm thick Cu film on top of it and specimens of 10 x 10 mm in lateral dimension were used. In Figure 3a the two corresponding sample curvatures are presented from room temperature up to 50°C, where pure elastic strain development can be assumed. In both cases a linear curvature-temperature (strain) relationship is observed. The decrease of h_s down to 400 µm led to an increase of the substrate curvature by a factor of ~ 5. For both configurations, the resulting thermal strain in the copper film at any given temperature is the same and follows equation (2). We assume

a constant CTE mismatch between Cu and Si of Δα = 14 ppm/K. Using the temperature data from the curvature measurements the respective strain evolution is plotted as a thick black line in Figure 3a. As displayed in Table 2, a thermal strain of -3.9x10^{-4} and -65 MPa respectively (using $\sigma_f = \varepsilon_m \cdot M_f$, with M_f = 168 GPa) at 50°C is obtained. Rearranging equation (1) and (3) we can calculate the strain from the curvature data using M_s = 180.5 GPa. For a common wafer thickness, h_s = 725 µm a final strain of -4.9x10^{-4} and -2.5x10^{-4} is obtained which would result in -82 MPa and -42 MPa for Stoney and Chu, respectively. One could argue that this discrepancy regarding an overestimation for Stoney (underestimation for Chu´s relation) could simply be a sensitivity problem due to the small curvature evolution [22]. However, a clearer picture evolves for h_s = 400 µm where Stoney´s relationship would result in -7.0*10^{-4} and -118 MPa. This would overestimate the strain/stress by almost a factor of ~2, whereas the analysis of Chu et al perfectly correlates with the developed stress by the predicted CTE mismatch of -65 MPa in the Cu film.

Table 2: Comparison of the predicted strain and stress values in copper at 50°C.

Method of validation	h_s = 725 µm		h_s = 400 µm	
	compressive ε_m	compressive σ_f	compressive ε_m	compressive σ_f
CTE mismatch	-3.9x10^{-4}	-65 MPa	-3.9x10^{-4}	-65 MPa
Stoney	-4.9x10^{-4}	-82 MPa	-7.0x10^{-4}	-118 MPa
Chu	-2.5x10^{-4}	-42 MPa	-3.7x10^{-4}	-63 MPa

These observations confirm that in general Stoney´s equation is only an approximation of the stress development for thin films on rigid substrates. For thin substrates it leads to the wrong curvature-strain relationship, while the Chu et al. derivation, where the curvature is ~$2 \cdot \kappa_{\text{stoney}}$, correlates well with our experimental observations. In fact, this emphasizes that the simplified model of having net-zero bending moment with regard to the composite curvature is not correct. If we consider the stress fields proposed in [21], equation (15) for the Cu layer, it becomes evident that a stress/strain gradient is directly proportional to the evolving curvature κ, scaling with the resulting bending curvature and the applied thermal strain ε_m. This is similar to the bending strain relationship for flexible electronics, where the strain in the outer fiber (e.g metallization layer) is proportional to its bending curvature [23]. With the decrease of h_s and the

understanding that the curvature is underestimated by a factor of ~ 2, significant strain gradients could locally lead to higher stresses in the surface region and cause an accelerated microstructure evolution, as evidenced in Figure 1 and 2. Furthermore, the density of geometrically necessary dislocations ρ_G is proportional to $|\kappa|$, which would give rise to a strain gradient in the bended lattice curvature [24].

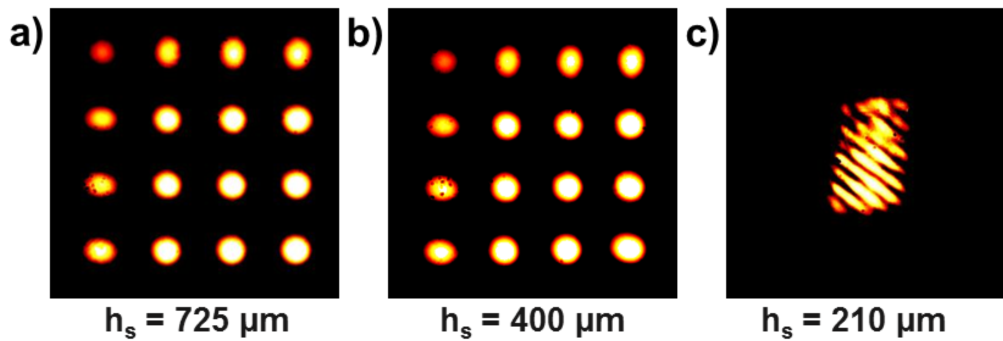

Figure 4: Detected multi-laser spot grid for a h_f = 5 µm Cu film at room temperature with a varying h_s of a) 725 µm, b) 400 µm and c) 210 µm.

Furthermore, the CCD detector images of the deflected laser beams in Figure 4 reveal that between h_s = 400 µm and 210 µm an abrupt "snap over" of the substrate curvature is observed, seen as a bifurcation of the sample curvature. Besides the impracticable measurement of the curvature evolution for h_s = 210 µm, this observation points to the presence of large non-linear deformation. Focussing on the ellipsoidal shape of the detected laser spots suggests that the curvature is a function of position and that twist moments are present. Such effects rise inevitably in modern microelectronics, and are not considered in common analysis but can have pronounced effect on the thermo-mechanical material behaviour.

5 Conclusions

The detailed results regarding the microstructural evolution of 5 µm Cu films upon thermal fatigue revealed a strong substrate thickness dependency. The findings showed that distinct grain growth coupled with twin migration and accelerated surface roughening was present for Cu films cycled on thin substrates with h_s= 323 and 220 µm. The examination of Stoney´s curvature-strain relation using wafer curvature measurements showed distinct deviations between the expected and measured curvature. The significantly larger sample curvature in combination with expected

plastic strain gradients in the film material can serve as an explanation for the accelerated material degradation. The observations with respect to non-uniform sample curvature and bifurcation for thinner substrates (e.g. 210 µm) furthermore raise the need of more detailed investigations of the actual limits of Stoney´s assumptions on small substrate deformation and its implications for microstructural effects on semiconductor thin film materials.

6 Acknowledgement

The work was performed in the project EPPL, financially supported by grants from Austria, Germany, The Netherlands, France, Italy, Portugal, and the ENIAC Joint Undertaking (ENIAC JU Grant Agreement no. 325608). This project is co-funded within the programme "Forschung, Innovation und Technologie für Informationstechnologie" by the Austrian Ministry for Transport, Innovation and Technology.

7 References

[1] G.G. Stoney, Proceedings of the Royal Society of London. Series A 82(553) (1909) 172-175.

[2] S. Timoshenko, Journal of the Optical Society of America 11(3) (1925) 233-255.

[3] A. Brenner, S. Senderoff, J. Res. Natl. Bur. Stand 42(105) (1949) 105-123.

[4] S.P. Timoshenko, S. Woinowsky-Krieger, Theory of plates and shells, McGraw-hill1959.

[5] R.H. Saul, Journal of Applied Physics 40(8) (1969) 3273-3279.

[6] L.B. Freund, J.A. Floro, E. Chason, Applied Physics Letters 74(14) (1999) 1987-1989.

[7] G. Janssen, M. Abdalla, F. Van Keulen, B. Pujada, B. Van Venrooy, Thin Solid Films 517(6) (2009) 1858-1867.

[8] J. Vobecky, M. Rahimo, A. Kopta, S. Linder, Exploring the Silicon Design Limits of Thin Wafer IGBT Technology: The Controlled Punch Through (CPT) IGBT, 2008 20th International Symposium on Power Semiconductor Devices and IC's, 2008, pp. 76-79.

[9] K. Zoschke, M. Wegner, M. Wilke, N. Jürgensen, C. Lopper, I. Kuna, V. Glaw, J. Röder, O. Wünsch, M.J. Wolf, O. Ehrmann, H. Reichl, Evaluation of thin wafer processing using a temporary wafer handling system as key technology for 3D system integration, 2010 Proceedings 60th Electronic Components and Technology Conference (ECTC), 2010, pp. 1385-1392.

[10] G. Zhang, R. Schwaiger, C. Volkert, O. Kraft, Philosophical Magazine Letters 83(8) (2003) 477-483.

[11] G. Zhang, C. Volkert, R. Schwaiger, P. Wellner, E. Arzt, O. Kraft, Acta Materialia 54(11) (2006) 3127-3139.

[12] O. Kraft, R. Schwaiger, P. Wellner, Materials Science and Engineering: A 319–321 (2001) 919-923.

[13] M. Finot, I. Blech, S. Suresh, H. Fujimoto, Journal of Applied Physics 81(8) (1997) 3457-3464.

[14] B.D. Harper, W. Chih-Ping, International journal of solids and structures 26(5-6) (1990) 511-525.

[15] A. Wimmer, M. Smolka, W. Heinz, T. Detzel, W. Robl, C. Motz, V. Eyert, E. Wimmer, F. Jahnel, R. Treichler, G. Dehm, Materials Science and Engineering: A 618 (2014) 398-405.

[16] S. Bigl, T. Schöberl, S. Wurster, M.J. Cordill, D. Kiener, Surface and Coatings Technology 308 (2016) 404-413.

[17] S. Bigl, S. Wurster, M.J. Cordill, D. Kiener, BHM Berg- und Hüttenmännische Monatshefte 160(5) (2015) 235-239.

[18] K. Chavez, D. Hess, Journal of The Electrochemical Society 148(11) (2001) G640-G643.

[19] S. Bigl, S. Wurster, M.J. Cordill, D. Kiener, Thin Solid Films 612 (2016) 153-164.

[20] S. Bigl, W. Heinz, M. Kahn, H. Schoenherr, M.J. Cordill, JOM 67(12) (2015) 2902-2907.

[21] S. Chu, Journal of the Electrochemical Society 145(10) (1998) 3621-3627.

[22] E. Chason, Sandia National Laboratories (2005).

[23] Z. Suo, E. Ma, H. Gleskova, S. Wagner, Applied Physics Letters 74(8) (1999) 1177-1179.

[24] N. Fleck, J. Hutchinson, Advances in applied mechanics 33 (1997) 296-361.

X List of Publications

S. Bigl, S. Wurster, M. J. Cordill, D. Kiener

Site specific microstructural evolution of thermo-mechanically fatigued copper Films

Berg und Hüttenmännische Monatshefte (2015) Vol. 160; Issue 5; 235‐239

S. Bigl, W.Heinz, M. Kahn, H Schönherr, M. J. Cordill

High-temperature characterization of silicon dioxide films with wafer curvature

Journal of the Minerals, Metals & Materials Society (2015) Vol. 67; No. 12; 2902-2907

S. Bigl, S. Wurster, M. J. Cordill, D. Kiener

Advanced characterization of thermo-mechanical fatigue mechanisms of different copper film systems for wafer metallizations

Thin Solid Films (2016) Vol. 612; 153–164

S. Bigl, T. Schöberl, S. Wurster, M. J. Cordill, D. Kiener

Correlative microstructure and topography informed nanoindentation of copper films

Surface and Coatings Technology (2016) Vol. 308; 404–413

S. Wurster*, S. Bigl*, M. J. Cordill, D. Kiener

Accelerated thermo-mechanical fatigue of copper metallizations studied by pulsed laser heating

Microelectronic Engineering (2017) Vol. 167; 110–118

S. Bigl, C. O. W. Trost, S.Wurster, M. J. Cordill, D. Kiener

Film thickness dependent microstructural changes of thick copper metallizations upon thermal fatigue

Journal of Materials Research (2016); revised-submitted

Stephan Bigl, Stefan Wurster, Megan J. Cordill, Daniel Kiener

Limits of Stoney's equation: substrate influenced thermo-mechanical fatigue of copper metallizations

Thin Solid Films (2017); submitted

*Both authors contributed equally